

Spin-polarized Scanning Tunneling Microscopy and Spectroscopy Study of Fe and Co Nanostructures on Cu(111)

DISSERTATION

zur Erlangung des akademischen Grades
doctor rerum naturalium (Dr. rer. nat.)

vorgelegt der
Naturwissenschaftlichen Fakultät II - Chemie und Physik
der Martin-Luther-Universität Halle-Wittenberg

von Herrn **Marco Corbetta**
geboren am 06.01.1984 in Bollate (Mi), Italien

angefertigt am
Max-Planck-Institut für Mikrostrukturphysik
in Halle an der Saale

Gutachter:

1. Prof. Dr. J. Kirschner
2. Prof. Dr. W. Widdra
3. Prof. Dr. C. M. Schneider

Verteidigungsdatum: 18.07.2013

Contents

| | | |
|----------|--|-----------|
| 1 | Introduction | 1 |
| 2 | Introductory remarks on spin-polarized Scanning Tunneling Microscopy | 5 |
| 2.1 | Spin-polarized STM/STS | 5 |
| 3 | Experimental setup and methods | 11 |
| 3.1 | The Cryo-SFM | 11 |
| 3.2 | Spectroscopy | 13 |
| 3.3 | Sample and tip preparation | 14 |
| 3.3.1 | sample preparation | 14 |
| 3.3.2 | Tip preparation | 16 |
| 3.4 | Extraction of the dI/dV asymmetry | 18 |
| 4 | Electron confinement in nanostructures on Ir(111) and Cu(111) | 23 |
| 4.1 | Graphene nano islands | 23 |
| 4.2 | Co nano islands | 27 |
| 4.3 | Fe-decorated Co nano islands | 29 |
| 5 | Characterization of bulk Cr and Fe-coated W tips for spin-polarized STM: spin polarization and temperature dependent measurements | 33 |
| 5.1 | Bulk Cr tips | 34 |
| 5.2 | Temperature dependent measurements using Fe-coated W tips | 36 |
| 6 | Magnetic properties of Co and Fe nanostructures on Cu(111) | 39 |
| 6.1 | Spatial dependence of the spin-polarized electronic properties near the edges of Co nano islands | 39 |
| 6.1.1 | Induced spin polarization in Cu near Co islands | 40 |
| 6.1.2 | Spin-dependent Smoluchowski effect | 42 |
| 6.2 | Nanomagnetism of Co and Fe islands: magnetization reversal | 45 |
| 6.2.1 | Island size dependence of the magnetic switching field of individual Co nano islands | 45 |
| 6.2.2 | Island size dependence of the magnetic switching field of individual Fe-decorated Co nano islands | 46 |
| 6.3 | Spin dependent electronic properties of Fe islands and Fe-decorated Co islands | 48 |

| | | |
|----------|---|------------|
| 7 | Discussion | 57 |
| 7.1 | Electron confinement in graphene nano islands | 58 |
| 7.2 | Electron confinement in Co nano islands and Fe-decorated Co nano islands | 62 |
| 7.3 | Magnetic response and spin polarization of bulk Cr tips | 67 |
| 7.4 | Temperature dependent measurements with Fe-coated W tips | 69 |
| 7.5 | Estimation of the induced spin polarization in Cu in proximity of a Co island | 72 |
| 7.6 | Spin-dependent Smoluchowski effect | 73 |
| 7.7 | Magnetization reversal of individual Co and Fe-decorated Co islands | 77 |
| 7.7.1 | Co nano islands | 77 |
| 7.7.2 | Fe-decorated Co nano islands | 79 |
| 7.8 | Novel magnetic structure of nano structured Fe on Cu(111) | 84 |
| 7.8.1 | The stripe pattern of Fe phase-b | 84 |
| 7.8.2 | Fe phase-a | 90 |
| 7.8.3 | Spin polarization of Fe-decorated Co islands | 91 |
| 8 | Conclusions and outlook | 93 |
| | Bibliography | 97 |
| | Publications | 113 |
| | Acknowledgments | 115 |
| | Curriculum vitae | 117 |
| | Erklärung an Eides statt | 119 |

Chapter 1

Introduction

The study of electronic and magnetic properties on the nanoscale has been the focus of intensive research in the past few decades and has led to revolutionary developments in catalysis [1–4], energy applications [5–8], high-density magnetic storage devices [9–16] and magnetic random-access memory (MRAM) [17–21]. Also many fundamental issues regarding the physics of magnetism and antiferromagnetism are related to sub-nanoscale properties and questions about the magnetic anisotropy, spin polarization, coercive fields and exchange bias have been related to properties on the atomic scale [22–25]. Experimental investigation of atomic-scale spin properties was first accomplished for magnetic metals by combining the atomic-resolution capability of scanning tunneling microscopy (STM) [26–32] with spin sensitivity, based on vacuum tunneling of spin-polarized electrons [33]. The resulting technique, spin-polarized scanning tunneling microscopy (sp-STM) [34–36], provides unprecedented insight into collinear and noncollinear spin structures at surfaces of magnetic nano structures and has already led to the discovery of new types of magnetic order at the nanoscale such as two dimensional magnetic skyrmion lattices [37, 38].

Spin-polarized STM is the experimental technique used in this thesis to study spin-dependent electronic and magnetic properties of Co and Fe nano structures on Cu(111). I used this technique also to investigate electron confinement in Co nano islands and Fe-decorated Co nano islands on Cu(111) and graphene nano islands on Ir(111).

Confinement induced electronic properties in nano structures are of great interest in many research fields, such as nano electronics and magnetism. The first studies on quantum interference phenomena and confinement of surface state electrons on metal surfaces were already reported in the early 1990's by Crommie and Hasegawa [39, 40]. Since then, quantum interference phenomena were observed in many different nanosized systems [41–53]. In this thesis, the first observation of quantum electron confinement in nano-size graphene islands on Ir(111) is shown [54]. Graphene is one candidate for future nano electronic devices [55–59], and one leading question for its application in nano electronics is how its electronic properties depend on the size at the nanoscale. Our results provide experimental insights into the physics relevant for graphene-based electronics, where engineering of electronic properties via well-defined nanostructuring is likely to be a central issue.

Experiments on electron confinement are also of central importance to ob-

tain information about the scattering potential which confines the surface state electrons within the nanostructure. In this thesis, a novel approach to alter the scattering potential by modifying the edge electronic properties of a nano structure is introduced. For this purpose, the edges of Co nano islands were decorated with Fe. This thesis presents the first report on the remarkable differences between confinement in pure Co islands as compared to Co cores of Fe-decorated Co islands. This provides new insights into the correlation between structural relaxations and local electronic properties at the edges of nanostructures.

At the edge of a nanostructure, such as a Co island on Cu(111), the electron charge tends to spill out and smoothen the transition of the electronic charge density, which differs from the abrupt variation of the positions of the positively charged atomic nuclei [60]. This was already discussed some 70 years ago by Smoluchowski, and the corresponding effect of charge redistribution near surface corrugations bears his name. The Smoluchowski effect focuses on the total electron charge density and it neglects that electrons, in addition to charge, also carry a spin. Evidence for the spin-dependence of the Smoluchowski effect at the edge of a Co nano structure is shown here for the first time in a close cooperation between theory and experiment [61]. In view of technological application, the possibility to tune the tunneling magneto resistance of nano structured magnetic tunnel junctions on a Ångstrom scale is demonstrated by exploiting this novel insight.

This thesis presents new insights also into another topic of utmost interest for magnetic recording industry as well as for fundamental research, such as the mechanism of magnetization reversal in nanoscale particles [62–73]. Studies on the switching of magnetic particles are mostly performed on ensemble of particles by averaging techniques [23, 72–74]. On the other hand, sp-STM allows to measure the switching field of single nano particles. Here, the size dependence of the switching field for individual Co nano particles on Cu(111) is revisited [75, 76]. Previous results indicate a crossover of the magnetization reversal from an exchange-spring behavior to domain wall formation with increasing size [77, 78]. Here, the first results on the impact of an Fe decoration on the magnetization reversal of Co nano islands are presented. Surprisingly, the Fe decoration contributes in a non-trivial way to the magnetism of the Fe-decorated Co nano particle. The main reason of this result is that nano structured bilayer Fe on Cu(111) shows a novel and unexpected magnetic order at the nano scale.

This thesis identifies a stripe pattern in the spin-polarized spectroscopy of the differential conductance of bilayer Fe on Cu(111), which has a magnetic origin and has not been described so far. The physical origin of this magnetic contrast is not fully resolved yet. It points at the importance of non-collinear spin states in magnetic nanostructures.

Fundamental experimental aspects of spin-polarized STM are also addressed in this thesis. In order to extract reliable information about the magnetic properties of the sample, the importance of characterizing the magnetic response of the tip apex is fundamental. For this purpose, temperature dependent measurements of the differential conductance on the applied magnetic field were performed for Fe-coated W tips [34, 79]. A superparamagnetic response of the magnetic moment of the Fe-coated tips used in this work was established.

This thesis introduces also bulk Cr tips as magnetic probes for in-field sp-STM [80]. In contrast to W tips covered with a magnetic material, which are the magnetic probes typically used for sp-STM [34, 79, 81, 82], bulk Cr tips

present the advantage of a simpler preparation [83]. They require neither high-temperature flashing nor material deposition. This aspect is of interest in experiments where tip exchange or tip treatment are experimental not feasible. A spin polarization of the tip apex as large as 45% is extracted [80], which is comparable with the spin polarization of Fe-coated W tips. The precise characterization of the magnetic tips used in the experiments opens the way to tackle both spin dependent electronic properties and nano magnetism aspects of the samples investigated down to the nanoscale.

The thesis is organized as follows. *Chapter 2* illustrates introductory basic theoretical concepts of spin-polarized scanning tunneling microscopy (sp-STM) and spectroscopy (sp-STs). *Chapter 3* describes the low temperature STM operated in magnetic field used for this work. Also, the preparation of samples and magnetic probes used in this thesis are described. The extraction of the asymmetry of the differential conductance between parallel and anti-parallel configuration of tip and sample magnetization is also introduced here, and this is important for the discussion of the spin polarization of the magnetic nanostructures investigated in this thesis. *Chapter 4* presents the results on electron confinement. The first observations of electron quantum confinement within graphene nano islands on Ir(111) and the comparison between electron quantum confinement within pure Co islands and within the Co cores of Fe-decorated Co islands on Cu(111) are described. Experimental results of spin-polarized STM follow in *Chapter 5*, where magnetic properties of bulk Cr tips are characterized and temperature dependent measurements are performed with Fe-coated W tips in order to gain insights into the magnetic behavior of the tip magnetic moment. *Chapter 6* focuses on the results on the magnetic properties of Co and Fe nano structures on Cu(111). Measurements to detect the induced spin polarization in the Cu substrate in proximity of Co islands are presented, and clear evidence of the existence of a spin-dependent Smoluchowski effect is shown for the first time. *Chapter 6* also reports the results of the size dependence of the switching field for individual Fe-decorated Co islands, in comparison to previous work on pure Co islands. Clear evidence of a novel and unexpected magnetic order of nano structured bilayer Fe on Cu(111) is found. All experimental results are thoroughly discussed in *Chapter 7*, and conclusions and indications for future prospects are presented at the end of the thesis.

Chapter 2

Introductory remarks on spin-polarized Scanning Tunneling Microscopy

The invention of STM by Binnig and Rohrer [26–28] in the early 1980’s has revolutionized surface science, and it was awarded with a Nobel prize in 1986. The possibility of combining atomic resolution in imaging with the capability of performing spectroscopy, probing both occupied and empty electronic states, opened the way to investigate the physical properties of nanostructures and even single atoms. A decade after its invention, the introduction of spin-polarized STM [33, 84], allowed the investigation of magnetic and spin-dependent properties down to the atomic scale.

The main topics of this work are spin-dependent scanning tunneling spectroscopy measurements (sp-STM). This Chapter gives a brief description of the relevant mechanisms involved in spin-STM measurements. However, the goal of this section is not to give a complete description of all phenomena occurring in real sp-STM experiments, since more detailed descriptions can be found in textbooks [29–32] and exhaustive reviews are given by Bode [34], Wulfhekel and Kirschner [35] and Wiesendanger [36].

2.1 Spin-polarized STM/STS

The principle of operation of sp-STM is based on the difference of the density of states near the Fermi energy for electrons of different spin character. Due to the quantum mechanical exchange interaction between electrons, the density of states splits up into minority and majority states, which are shifted rigidly against each other in the band model of ferromagnetism [85], as shown in Fig. 2.1. The imbalance causes a spin polarization, in contrast to paramagnetic substances, in which the density of states of spin-up and spin-down electrons are identical at the same energy. This splitting of the density of states has immediate consequences on the tunneling current, as discussed by Jullière in 1975 [86]. When electrons tunnel between two ferromagnets, the magnitude of the current is influenced by the orientation of magnetization of the two electrodes and the

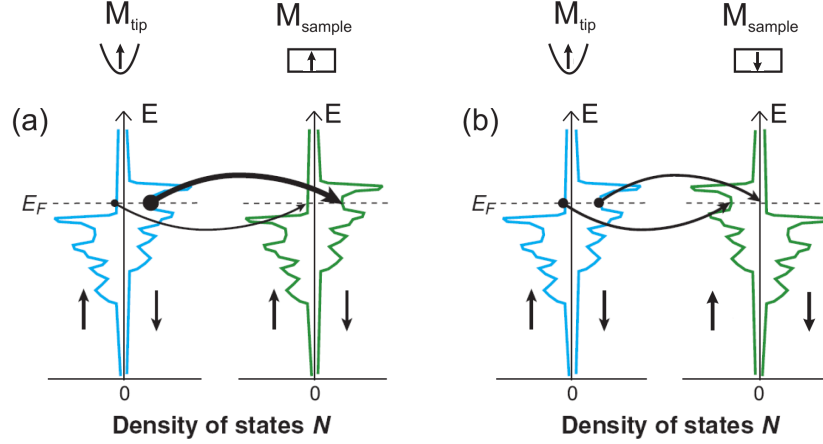


Figure 2.1: Simplified picture of spin polarized tunneling within an hypothetical spin split density of states model [35]. The spin orientation of the tunneling electrons is assumed to be conserved during tunneling, i.e. spin-up electrons always tunnel into spin-up states and spin-down electrons always tunnel into spin-down states. Black arrows indicate the DOS of spin-up and spin-down electrons. M_{tip} and M_{sample} denote the magnetization orientation of tip and sample, respectively. (a) Parallel and (b) antiparallel alignment of tip and sample magnetization lead to high and low tunnel current, respectively.

phenomena was called tunneling magnetoresistance (TMR) effect.

Figure 2.1 presents a very simplified sketch of spin polarized tunneling involving two hypothetical spin-split density of states (DOS) [35]. In this picture it is assumed that the spin orientation of the tunneling electrons is conserved, i.e. spin-flip processes during tunneling are excluded. This is well justified in the limit of low bias voltage [34], where the tunnel current is dominated by elastic processes. In Fig. 2.1(a) the situation for a parallel alignment of tip and sample magnetization is shown. For the sake of simplicity the electronic structure of both tip and sample are considered to be identical. Under parallel alignment and with a small positive voltage applied to the sample, electrons can tunnel from occupied spin-up (spin-down) states of the tip into unoccupied spin-up (spin-down) states of the sample. The high DOS of spin-down electrons at the Fermi energy of tip and sample results in a high tunnel current (thick black arrow). The contribution of spin-up electrons to the tunnel current is very small, due to the reduced spin-up DOS at the Fermi level, as marked by the thin black arrow. In Fig. 2.1(b) the magnetization of the sample is reversed, the DOS of spin-up and spin-down electrons are swapped. Now the number of unoccupied sample states of spin-down character is strongly diminished, which leads to a low tunnel current of the spin-down electrons. For the spin-up electrons the situation remains unchanged. Despite the higher density of unoccupied states in the sample, the number of occupied tip states available for tunneling is unchanged. In conclusion the tunnel current is smaller in the antiparallel situation than in the parallel situation.

For a theoretical description following Bardeen's perturbative treatment of

tunneling [87, 88], the tip and sample wave functions have to be replaced by spinors, and the problem of deriving an expression for the tunneling current involves a spinor transformation from the spin coordinate system of one electrode to the spin coordinate system of the other electrode, leading to the following expression for the total tunneling current I_t in the limit of small applied bias voltage [86, 89]

$$I_t \propto V(\rho_T^\uparrow \rho_S^\uparrow |M_{\uparrow, \uparrow}|^2 + \rho_T^\uparrow \rho_S^\downarrow |M_{\uparrow, \downarrow}|^2 + \rho_T^\downarrow \rho_S^\uparrow |M_{\downarrow, \uparrow}|^2 + \rho_T^\downarrow \rho_S^\downarrow |M_{\downarrow, \downarrow}|^2) \quad (2.1)$$

Here, $\rho_{T,S}^{\uparrow, \downarrow}$ denote the spin-resolved densities of states for tip and sample, respectively, and $M_{\uparrow, \downarrow}$ are the tunneling matrix elements for transitions between the spin-dependent states of the tip and sample. Introducing the total tip (sample) LDOS as

$$\rho_{T(S)} = \rho_{T(S)}^\uparrow + \rho_{T(S)}^\downarrow \quad (2.2)$$

and the spin polarization of the tip (sample) DOS

$$P_{T(S)} = \frac{\rho_{T(S)}^\uparrow - \rho_{T(S)}^\downarrow}{\rho_{T(S)}^\uparrow + \rho_{T(S)}^\downarrow} \quad (2.3)$$

Equation 2.1 can be simplified as follows:

$$I_t \propto V |M_0|^2 \rho_T \rho_S (1 + P_T P_S \cos \theta) \quad (2.4)$$

where M_0 is the average matrix element and θ is the angle between the magnetization of the two electrodes. Equation 2.4 is an extension of Slonczewski result [89] and it reduces to the result of Tersoff and Hamann [90, 91] if one of the electrodes, either the tip or sample, is nonmagnetic ($P_T = 0$ or $P_S = 0$). According to Eq. 2.4 the tunneling conductivity in the magnetic case is expected to depend on the spin-resolved local density of states at the Fermi energy for both electrodes and on the cosine of the angle θ between the magnetization directions of tip and sample, similarly to the case of planar magnetic tunnel junctions.

Although constant-current sp-STM is sensitive to an energy-integrated property (I_t) it plays a unique role to reveal complex atomic-scale spin structures at ultimate magnetic resolution [38, 92, 93]. This is because the coefficients of the 2D Fourier transform of the surface lattice decay exponentially with increasing length of the reciprocal lattice vectors [34, 90, 94]. Therefore the STM image is primarily dominated by the smallest non-vanishing reciprocal lattice vector. Since any magnetic superstructure leads to a larger periodicity in real space compared to a nonmagnetic state, the corresponding reciprocal lattice vectors become smaller than those related to the structural unit cell. As a consequence, the expansion coefficients for the spin-polarized contribution to the tunneling current become exponentially larger than those of the non-polarized part. Thus, a constant-current sp-STM image reflects the magnetic superstructure rather than the atomic structure [94]. However, the use of this type of operation mode has some limitations. For example, measurements of rough surfaces at larger length scales are difficult because topographic features and magnetic structures might interfere. Moreover, at relatively large bias voltage V applied between

tip and sample, the energy integration can lead to a reduced spin-polarized tunneling current signal if the spin polarization of the relevant electronic states contributing to the tunneling current changes sign in the energy range between the Fermi level and eV . These limitations can be overcome by operating the sp-STM in the spectroscopic mode.

Spin Polarized Scanning Tunneling Spectroscopy (sp-STs) provides direct access to the spin- and energy-resolved DOS of the sample and it can be qualitatively explained by the same picture used for constant-current sp-STM. Using the theory of Tersoff and Hamann [90,91] generalized for the magnetic case [94], the following expression for the local differential tunneling conductance can be derived

$$\frac{dI}{dV} \propto \rho_T(E_F)\rho_S(E_F + eV)[1 + P_T P_S(E_F + eV) \cos \theta] \quad (2.5)$$

Comparing Eq. 2.5 with Eq. 2.4 reveals the essential difference between the contrast mechanisms of the two operating modes. While the differential conductivity is directly proportional to ρ_S and P_S at the energy $E_F + eV$, the constant current STM image, is governed by the energy integrated quantities ρ_S and P_S . For a more detailed treatment, see ref [94].

An outstanding characteristic of sp-STM is the capability to detect spatial variation of the energy resolved spin polarization of the sample surface with sub-nanometer resolution. In spin-polarized STM experiments the spin polarization of the sample can be determined from measurements of the asymmetry of the differential conductance for states of parallel and anti-parallel orientations between tip and sample magnetization. The asymmetry A of the differential conductance is defined as

$$A = \frac{dI/dV_{AP} - dI/dV_P}{dI/dV_{AP} + dI/dV_P} \quad (2.6)$$

where dI/dV_{AP} and dI/dV_P are the differential conductance signals measured with the tip and sample magnetization in antiparallel (AP) and parallel (P) configurations, respectively. Substituting Eq. 2.5 in Eq. 2.6, the asymmetry of the differential conductance A can be linked to the spin polarization of the tip, P_T , and of the sample at the tip apex position, P_S

$$A = -P_T P_S \quad (2.7)$$

At a fixed voltage value, the spin polarization of the tip P_T is constant and the dI/dV asymmetry is proportional to the spin polarization of the sample P_S . The feasibility of this approach has been demonstrated before [95], where the comparison between experimentally measured asymmetry of the differential conductance and calculated spin polarization supports the applicability of this approach to extract spin polarization above a Co nano island on Cu(111) by sp-STM with high spatial resolution.

In the same manner, tip and sample spin polarizations (P_T and P_S) can be related to the tunnel magneto resistance (TMR) [96]. The TMR is defined as

$$TMR = \frac{I_P - I_{AP}}{I_{AP}} \quad (2.8)$$

Using Eq. 2.4 in Eq. 2.8, we obtaine

$$TMR(E) = \frac{2P_T(E)P_S(E)}{1 - P_T(E)P_S(E)} \quad (2.9)$$

Polarizations of surface states are of the order of 10–20% and tip spin polarization larger than 40–50% are rarely achieved. This means that $|P_T P_S| \ll 1$ and therefore

$$TMR(E) \simeq 2P_T(E)P_S(E) \quad (2.10)$$

It means that for small tip and sample spin polarizations, the TMR is proportional to the asymmetry of the differential conductance with an opposite sign. Thus, for small spin polarizations of tip and sample, the TMR ratio is proportional to the spin polarization above the sample and it can be estimated from the spin polarizations of tip and sample alone. This conclusion was recently confirmed by sp-STM measurements on Co islands on Cu(111) [97], where clear spatial modulation of the TMR ratio with amplitudes as large as 20% and spacing of about 1.3 nm were observed around the Fermi energy due to spin-dependent quantum interference. Spatial variations of the TMR ratio at the Ångstrom scale at the edge of a Co nanostructure are also presented in this thesis in Section 6.1.2 and further discussed in Section 7.6.

Chapter 3

Experimental setup and methods

This Chapter describes the low temperature scanning tunneling microscope that was used to perform all the measurements presented in this thesis. In Section 3.3, the sample preparations are described. Preparations of magnetic STM tips for studying the magnetic properties of single magnetic nano particles are discussed. A thorough discussion of the preparation of magnetic tips for spin-polarized STM follows in Chapter 5. The last section of the chapter introduces a method which is widely used throughout the thesis, namely the extraction of the asymmetry of the differential conductance dI/dV from the measurement of differential conductance maps for states of parallel and anti-parallel orientation between tip and sample magnetization.

3.1 The Cryo-SFM

The results presented in this work have been achieved by using a so-called Cryogenic SFM from Omicron NanoTechnology¹. The Cryogenic SFM is designed to operate at cryogenic temperatures and in high magnetic fields. In addition to STM, an interferometric glass fiber setup enables atomic force microscopy (AFM). However, in this work I only used the STM capabilities.

Figure 3.1 shows selected aspects of the Cryogenic SFM. The instrument is operated inside a ⁴He bath cryostat² with optical access and it is attached to a UHV chamber (Fig. 3.1(a)). The cryostat is a so-called top loader, where the STM head is lowered from the top into it. Loading of tip and sample into the STM is done in the UHV chamber above the cryostat at room temperature. The base pressure of the STM chamber is 1×10^{-11} mbar, and it is estimated to be orders of magnitudes smaller at the STM head in the cryostat due to the cryo pumping of the cold (liquid He cooled) chamber wall in the cryostat. The setup is fairly tall (4 m), as indicated in Fig. 3.1(a) to provide the necessary vertical travel.

The cryostat contains concentric tanks for the cryo liquids. An outer liquid nitrogen surrounds two inner liquid helium (LHe) tanks. The outer helium

¹www.omicron.de

²Janis Research Company, www.janis.com

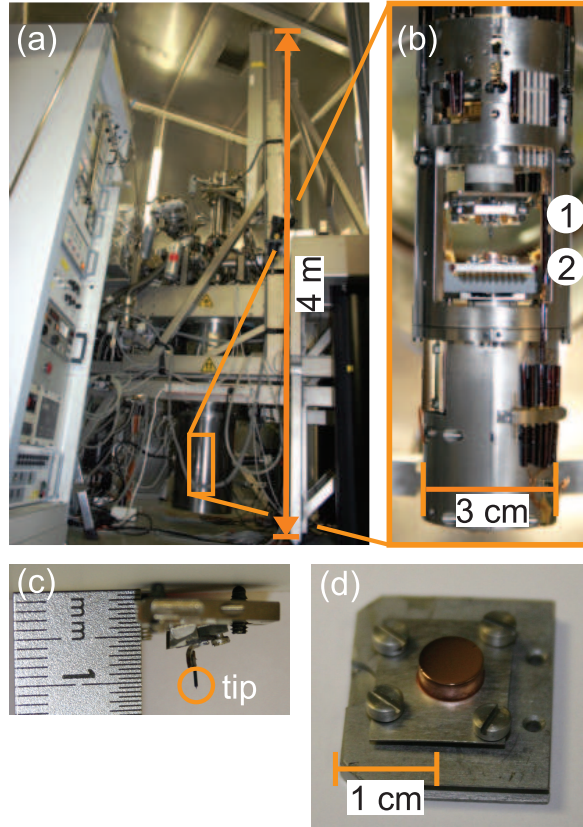


Figure 3.1: (a) Side-view of Omicron cryogenic STM. The STM head (b) is located at the bottom end of the cryostat (orange rectangle). (b) shows the tip holder 1 mounted at the x,y-coarse motion, the sample holder 2 is attached to the z-coarse motor and scanning piezo. (c) Side view of the tip holder, where the tip is spot welded to its support. (d) Cu(111) crystal, diameter 6 mm, mounted to the sample plate with Mo foils.

tank contains a superconducting magnet at its lower end, the inner helium tank cools the STM. The superconducting magnet produces a magnetic field of up to 7 T along the vertical axis, normal to the sample surface. The STM is cooled by pressing a conical heat exchanger to a LHe cooled counter cone within the UHV section of the cryostat by applying a contact force. The lowest reachable temperature is of order 7 – 8 K, as verified by calibrated Cernox sensors³ mounted at the STM head.

It is possible to set the temperature of the STM to values above its equilibrium value of 7 – 8 K. This is realized by a resistive heater which is built into the STM head. The temperature controller is able to keep the temperature of the STM within ± 0.1 K around the set temperature. Heating the STM from 8 K to 30 K is used in Section 5.2, where temperature dependent measurements of the magnetic field dependence of the differential conductance are performed

³LakeShore, www.lakeshore.com

on Fe-decorated Co islands to identify the magnetic response of Fe-coated W tips. The temperature of the STM can be also lowered by reducing the vapor pressure above the inner LHe reservoir, which is used for STM cooling. Thus, the equilibrium temperature of the STM can be lowered by roughly 1 K and kept for several hours, until the LHe reservoir is emptied.

Figure 3.1(b) shows the STM head with the central opening for the insertion of tip (1) and sample holder (2). The tip is positioned by a piezo coarse motion by ± 5 mm horizontally in x- and y-directions. The sample is mounted on the scanner piezo which gives a scan range of order $1 \mu\text{m}$ at 7 K. The scanner piezo is mounted at the z-coarse motion which gives a vertical travel of up to 10 mm. The tip is spot welded to the tip holder, Fig. 3.1(c), and the sample is clamped to a Mo-sample plate with thin Mo-foils and Mo screws, Fig. 3.1(d).

Different measures are taken to minimize the noise level during STM measurements. The whole UHV system is mounted on a frame which floats on an air based damping system during the measurements. This enables to decouple mechanical vibrations from the ground from the microscope. Inside the UHV chamber, the STM head hangs on a spring suspension and residual vibrations are damped by a three-stage eddy current damping system above the STM head. The foundation on which the UHV chamber is mounted also plays a relevant role. It consists of a concrete cube of $4 \times 4 \times 4 \text{ m}^3$ which sits in its own sand bed. This leads to a complete decoupling of the concrete cube from the rest of the building and consequently to an extremely efficient noise reduction for the STM. Furthermore, a sound proof cabin, which surrounds the UHV chamber, prevents acoustical vibrations from coupling to the STM.

The STM is combined with an UHV sample and tip preparation chamber, which includes a load lock for exchanging tip and sample without breaking the vacuum. Tip and sample can be transferred from the preparation chamber into the STM by a magnetically coupled linear drive, using wobble sticks for tip and sample handling. The preparation chamber is equipped with a scanning ion gun and a home-built sample and tip heating stage for cleaning purposes. Two evaporators are available to deposit different metals onto samples and tips.

3.2 Spectroscopy

The main results of this work were obtained by spectroscopy measurements of the differential conductance, so called $dI/dV(V)$ or STS spectra. The goal of such measurements is to retrieve information about the electronic structure of the sample. In this mode of operation the tip-sample distance is typically stabilized at a gap voltage of +0.5 V and a tunnel current of 1 nA. We estimate that this leads to a tip-sample distance of order 0.4–0.5 nm. Then the feedback loop is switched off and the applied bias is swept between an initial and a final value in some hundred steps within a few seconds. Disabling the feedback loop leads to a fixed tip sample distance throughout the measurement. During the voltage ramp, the tunnel current $I(V)$ and the differential conductance $dI/dV(V)$ are measured. By changing the stabilization parameters it is possible to probe the electronic structure at different heights above the surface. For example, increasing the set point current from 1 nA to 10 nA the tip-sample distance changes by 0.1 nm. Typically, 5 – 10 scans of $I(V)$ and differential conductance $dI/dV(V)$ spectra are averaged to improve the signal-to-noise ratio.

The differential conductance dI/dV is measured by a lock-in technique. An AC modulation with an amplitude of 5 – 20 mV at a frequency $f = 4$ kHz is added to the gap voltage and the resulting modulation of the tunnel current at frequency f is detected with a lock-in amplifier. These single point spectroscopy data are used to probe the electronic structure of the sample at a fixed position and a fixed tip-sample distance as a function of applied bias, i.e. as a function of energy. These measurements can be performed at each image pixel position, and a complete map of the spectroscopic properties results. The spectroscopic data acquisition of a 150×150 pixel image, with a spectroscopy scan of $I(V)$ and differential conductance $dI/dV(V)$ with 130 data points at each pixel, takes around 10 hours. For comparison, a constant current image with simultaneously taken differential conductance value at a fixed gap voltage takes a few minutes.

3.3 Sample and tip preparation

This section presents the experimental techniques to prepare STM magnetic tips and sample surfaces. The first part of this section describes the preparation of Co islands on Cu(111), of Fe and Fe-decorated Co islands on Cu(111) and graphene islands on Ir(111). The second part presents the preparation of magnetic STM tips required for spin-STM measurements.

3.3.1 sample preparation

Cu(111) and Ir(111) single crystal from MaTeck GmbH⁴ were used in this work as substrates. The as-delivered Cu(111) crystal was treated⁵ by mechanical and chemical polishing to reach a better orientation than 0.1° and to diminish the screw dislocations at the crystal surface.

The Cu(111) crystal was cleaned by cycles of Ar ion bombardment (1 keV, 1 μ A sample current, 15 min) at 300 K and subsequent annealing at 700 K for 15 min until atomically flat, clean and large terraces (hundreds of nm wide) were obtained. Co islands were grown by depositing a submonolayer amount of cobalt ($\simeq 0.4$ ML) at room temperature onto the clean Cu(111) surface. After the deposition, the sample was immediately transferred into the STM head and cooled down to low temperature in order to minimize potential intermixing of Co and Cu [98]. Figure 3.2 is a constant-current STM image showing an overview of Co islands on Cu(111) prepared in this way. The Co islands are two-atomic-layer high ($\simeq 0.4$ nm) and have an approximate triangular shape [99, 100]. The base length of the islands ranges from 4 nm to 30 nm.

Fe and Fe-decorated Co islands were grown by successive deposition of first Co ($\simeq 0.2$ ML) and then Fe ($\simeq 0.3$ ML) on the C(111) surface at 300 K, which was cleaned as described before. Depositions of both Co and Fe were performed by an e-beam evaporator with a deposition rate of order 2 min per monolayer. Figure 3.3(a) is a constant-current STM image showing an overview of the sample. Both pure Fe (Fig. 3.3(b)) and Fe-decorated Co islands (fig. 3.3(c)) form on the surface. Pure Fe islands (fig. 3.3(b)) show a smooth surface approximately all at the same height. Fe-decorated Co islands (Fig. 3.3(c)) are composed by

⁴www.mateck.de

⁵Polishing of the crystal was performed by Frau Menge at the Max-Planck-Institute of Halle.

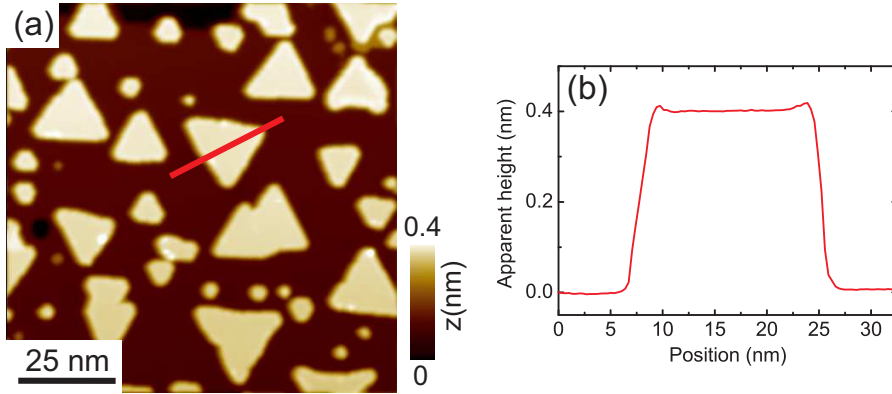


Figure 3.2: (a) Constant-current STM image of Co islands grown on Cu(111). (b) Line profile along the red line in (a). Imaging parameters: $V_{gap} = +0.5$ V, $I_t = 1$ nA, $T = 10$ K.

an inner Co core surrounded by a Fe rim. A clear cut distinction between Fe and Co is possible by studying the position dependence of the differential conductance dI/dV spectra within the islands, as discussed in Section 6.3. The apparent height of the Fe-decorated Co islands changes by 30 – 40 pm from the inner Co core to the Fe rim. Also, the apparent height of the Fe rim surrounding the Co core is not uniform due to inhomogeneous structural and electronic properties within the Fe rim as it will be discussed in Section 6.3. The apparent height of both kinds of islands depends on the applied bias voltage and it is about 0.35 – 0.4 nm, suggesting a height of two atomic layers.

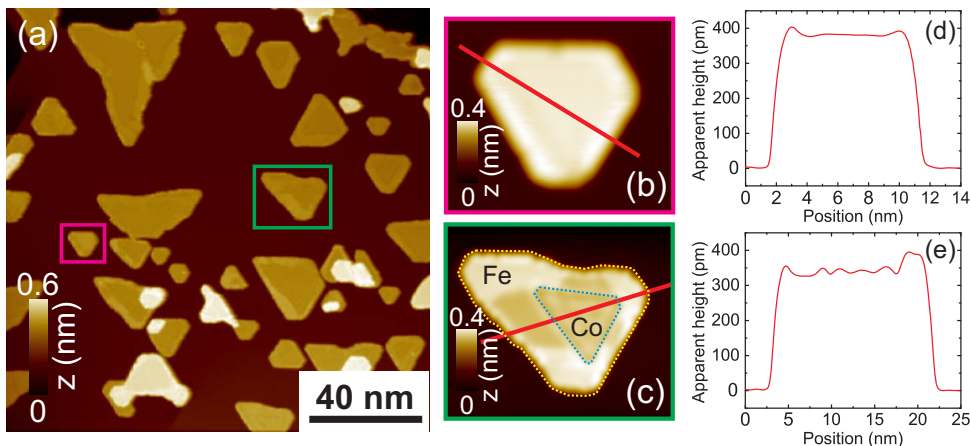


Figure 3.3: (a) Constant-current STM image of Fe and Fe-decorated Co islands grown on Cu(111). (b), (c) Close view of the pure Fe island and the Fe-decorated Co island surrounded by the magenta and green lines in (a), respectively. (d,e) Line profiles along the red lines in (b) and (c). Imaging parameters: $V_{gap} = +0.1$ V, $I_t = 1$ nA, $T = 10$ K.

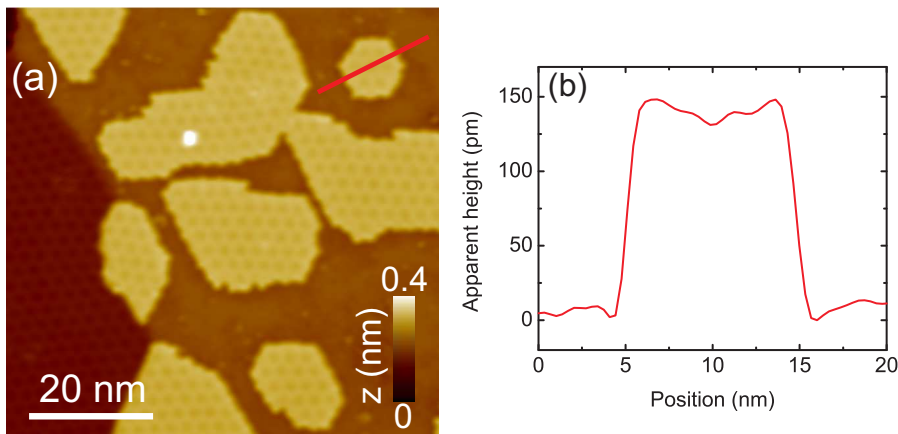


Figure 3.4: (a) Constant-current STM image of graphene islands grown on Ir(111). (b) Line profile along the red line in (a). Imaging parameters: $V_{gap} = +0.05$ V, $I_t = 1$ nA, $T = 10$ K.

The third sample studied in this work is graphene on Ir(111). The Ir(111) single crystal was cleaned by Ar ion sputtering at room temperature (2 keV, 1 μ A sample current, 20 min) and subsequently heated 10 times up to 1200 K in an oxygen pressure of 1×10^{-8} mbar. Finally, it was annealed at 1370 K at a pressure of 2×10^{-10} mbar. In order to grow monolayer graphene, the cleaned Ir(111) surface was exposed to C_2H_4 at room temperature and a pressure of 2×10^{-9} mbar for 2 min and subsequently heated to 1320 K for 2 min under the same partial pressure of C_2H_4 . Figure 3.4 is a constant-current STM image of the sample surface. STM image shows that $\simeq 60\%$ of the substrate surface is covered by graphene islands and their sizes range from 6 to 50 nm in diameter. Only single layer islands were observed (apparent height $\simeq 0.15 - 0.2$ nm).

3.3.2 Tip preparation

In order to obtain information about the magnetic properties of the sample, magnetic probes are required [34–36]. In this work, two magnetic STM tips were used: Fe-coated W tips and bulk Cr tips.

The preparation of Fe-coated W tips is a two step process which consists of ex-situ and in-situ treatments. The first step is an ex-situ etching process. Tips were produced from polycrystalline W wire (99.95%, diameter = 0.375 mm) electrochemical etched in 8% sodium hydroxide solution. All tips were produced by the so-called lamella etching technique, as described in early papers [101–104]. After etching, tips are mounted on a tip holder (Fig. 3.1(c)) and are subsequently introduced into the UHV chamber via the load lock. The aim of ex-situ preparation is obtaining tips with a sharp apex. As the etching is performed in air, chemical contamination of the tip with oxides and other compounds can be expected. In order to remove these impurities from the tip, all tips used in this work were heated in UHV up to $\simeq 2400$ K for a few seconds. The temperature of the tip apexes was monitored by an optical pyrometer during this flash annealing. Deposition of Fe on tips was performed by e-beam evaporator

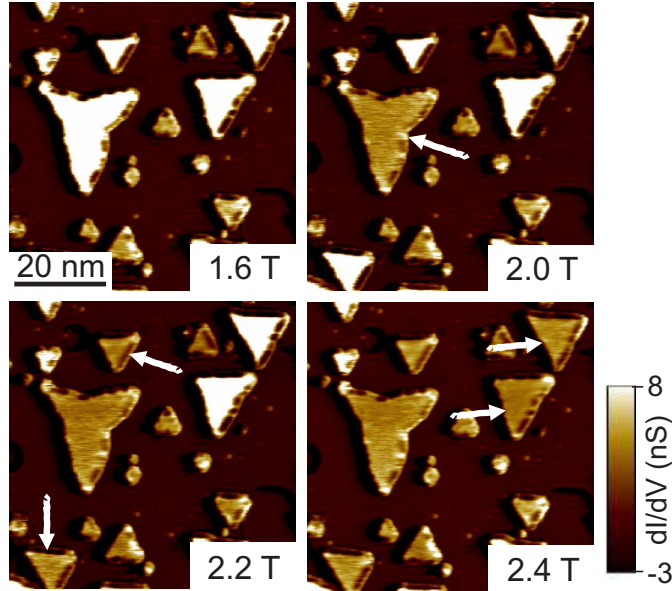


Figure 3.5: Maps of the differential conductance of bilayer Co islands on Cu(111) obtained with a magnetic tip (bulk Cr) at different external magnetic fields. White arrows mark islands the magnetization of which switches over sweeping of the magnetic field. Imaging parameters: $V_{gap} = +0.5$ V, $I_t = 1$ A, $T = 8$ K.

in the preparation chamber at 300 K. In this work, tips were covered with 40 – 80 atomic layers of Fe⁶. After the Fe deposition, the tips were annealed to $\simeq 1000$ K for a few seconds in order to flatten the deposited material. Omitting the anneal leads to unstable tips, which change the spectroscopic response in an uncontrolled arbitrary manner.

Bulk Cr tips were also used in this work [80]. As compared with Fe-coated W tips, bulk Cr tips present the advantage of a simpler preparation, i.e. they do not require high-temperature flashing or material deposition. Tips were produced starting from rods of polycrystalline Cr with a nearly square cross section of $0.7 \text{ mm} \times 0.7 \text{ mm}$ obtained by cutting a 99.99% Cr foil⁷. The etching was done in a 1.5 M NaOH solution and the procedure is divided in two steps. In the first, a pre-etching was performed with a ring-shaped gold cathode applying a DC voltage in the 5 – 7 V range in order to reduce the rod cross-section and to smoothen the edge of the rod. In the second step, the etching is performed using a DC voltage in the 3 – 4 V range until the drop off occurs. After etching, the tips were spot welded to the tip holder, inserted into the chamber and then directly used for STM experiments. The only in-situ preparation of the tip consisted of the application of voltage pulses (up to 10 V) between tip and sample during STM experiments.

Although the material at the tip apex is known to be spin-polarized as bulk sample, it is by no means a priori clear in which direction the magnetization at the tip apex points, nor how such a tip will respond to a magnetic field [79, 80].

⁶Deposition rate was calibrated by STM measurements on low coverages of Fe on Cu(111).

⁷Super Conductor Materials, www.scm-inc.com

One simple approach in order to test the magnetic sensitivity of the tips is the imaging of the magnetic sample in spectroscopy mode, while the magnetic state of the system is varied by an external field. The goal is to exploit the dependence of the differential conductance dI/dV on the relative orientation of the magnetization directions of tip and sample, as described in Chapter 2. We exploit our previous work on Co/Cu(111), which in agreement with early work by others [105] indicates an easy out-of-plane magnetization direction of Co bilayers islands with remanent magnetization in larger islands (≥ 1000 atoms) at 8 K. Figure 3.5 presents a series of dI/dV images of Co islands on Cu(111) taken with a bulk Cr tip at different magnetic field values. At a field of 1.6 T, the small islands appear darker than the large islands. Increasing the field to 2 T the color of the island marked by the white arrow changes from bright to dark. With a further increase of the magnetic field more and more islands change their color from dark to bright, until at 2.4 T all islands in the image exhibit a dark color. It can be concluded that, since only the external magnetic field is changing along the sample normal direction, the contrast change is due to the switching of the islands magnetization direction. To ensure the magnetic origin of the contrast, we also measure single point spectra of the differential conductance dI/dV on single particles as a function of an external magnetic field. Hysteresis loops of the differential conductance dI/dV of single particles are extracted from this data. Only these hysteresis loops of the differential conductance dI/dV allow a rigorous disentanglement of tip and sample contributions to the measured data and a clear-cut determination of the magnetic state of tip and sample. Details will be described in the next section and in Chapter 5.

3.4 Extraction of the dI/dV asymmetry

This section introduces the steps necessary to extract the asymmetry of differential conductance dI/dV from maps of the differential conductance dI/dV for states of parallel and anti-parallel orientation between tip and sample magnetization. The method described here is used in Sections 6.1.1, 6.1.2. and 7.3.

As already pointed out, the the magnetic configuration of a tip and its change in an external field is not clear a priori. It depends on both the macroscopic preparation by film coverage and on the microscopic preparation by voltage pulses [79, 80]. The first step to extract the asymmetry of differential conductance consists in measuring single point spectra of differential conductance on single nanostructures as a function of an external magnetic field. This is a fundamental measurement to understand the response of the local magnetic moment of the tip apex to an applied magnetic field. Only after disentangling tip and sample contributions to the measured data, a clear determination of states of parallel and anti-parallel orientation between tip and sample magnetization is possible.

Figure 3.6(a) shows the dependence of the differential conductance dI/dV on the magnetic field for the two-layer-high Co island in the inset. The measurement was performed with a bulk Cr tip. Changing the magnetic field induces changes of shape and amplitude of differential conductance dI/dV spectra. Sign and magnitude of the signal change depend on the bias voltage. At bias voltages where the curves cross there is no effect of the magnetic field detectable. I chose

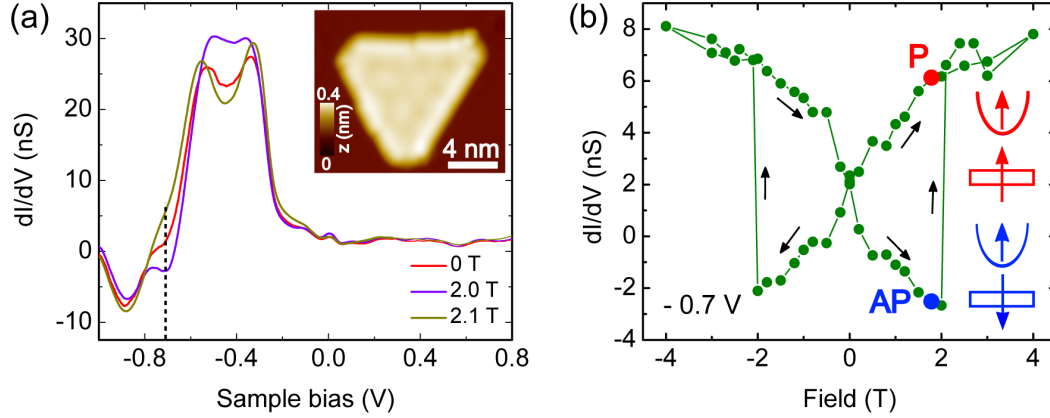


Figure 3.6: (a) Differential conductance (dI/dV) spectra measured with a bulk Cr tip at the center of the bilayer Co island on Cu(111) shown in the inset at different external magnetic fields at 8 K ($V_{stab} = +0.5$ V, $I_{stab} = 1.0$ nA). The dashed black line indicates the bias voltage at which the corresponding hysteresis loop of the differential conductance (b) was taken. (b) Hysteresis loops of the differential conductance at the center of the Co islands in the inset of (a) ($V = -0.7$ V). Arrows indicate the sequence in which the data were measured. Red and blue points respectively indicate parallel (P) and anti-parallel (AP) states between the magnetization direction of tip and sample at +1.8 T.

a bias of +0.5 V to study the effect of the external field more clearly by plotting the differential conductance at +0.5 V as a function of field in Fig. 3.6(b). In Fig. 3.6(b) a hysteresis curve of the differential conductance which is almost symmetric with respect to the differential conductance axis is observed. This finding tells us that both tip and sample respond to the magnetic field. Previous experiments have identified that the easy magnetization direction of bilayer Co islands on Cu(111) at low temperature is perpendicular to the surface with full remanence [105]. Thus, the abrupt change in the differential conductance is ascribed to the reversal of the magnetization direction of the Co island. On the other hand, the smooth signal variation at smaller fields indicates a continuous increase of the z -component of the magnetic moment of the tip apex towards the field direction. At large positive and negative fields the same differential conductance is observed which indicates an equivalent magnetic state in view of the tunnel experiment. At this point, a clear distinction between parallel (P) and antiparallel (AP) orientation of tip and sample local magnetic moment is possible, as indicated by the red and blue arrows in Fig. 3.6(b).

With this information it is possible to measure electronic properties in the P and AP states of the system. In order to extract asymmetry maps of the differential conductance we use the following procedure: (1) We sweep the magnetic field from 0 T up to +1.8 T (AP state, blue point in the hysteresis loop in Fig. 3.6(b)). (2) We record a spectra of the differential conductance for each point of the image in the inset of Fig. 3.6(a). (3) We sweep the magnetic field up to +4 T in order to switch the magnetization direction of the sample and to reliably establish a parallel state configuration. (4) We sweep the magnetic field

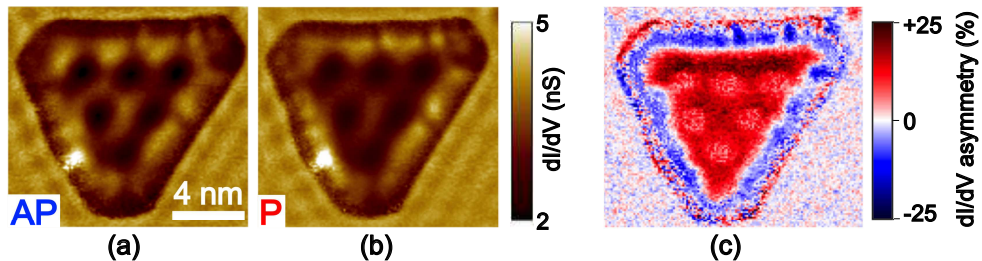


Figure 3.7: (a), (b) Two images of differential conductance of the Co island in the inset of Fig. 3.6, which are the basis for the asymmetry map of the differential conductance in (c). Both images were recorded at $B = +1.8$ T, but with different magnetization configurations between the magnetic tip and the Co island: antiparallel (a) and parallel (b). Measurement parameters: $V = +0.03$ V, $V_{stab} = +0.5$ V, $I_t = 1.0$ nA, $T = 10$ K, bulk Cr tip. V is the bias voltage at which the differential conductance is recorded and V_{stab} is the bias voltage to stabilize the tip before the feedback loop is opened. (c) Asymmetry map of the differential conductance dI/dV calculated from the images in (a) and (b).

down to $+1.8$ T (P state, red point in the hysteresis loop in Fig. 3.6(b)) and we repeat step (2). At this point, we have a map of the differential conductance for parallel and anti-parallel state at each bias voltage in the set range. From the measured maps of the differential conductance we calculate an asymmetry map of the differential conductance for each measured sample bias. We define the asymmetry of the differential conductance as

$$A = \frac{dI/dV_{AP} - dI/dV_P}{dI/dV_{AP} + dI/dV_P} \quad (3.1)$$

where dI/dV_{AP} and dI/dV_P are the differential conductance signals measured with the tip and sample magnetization in antiparallel (AP) and parallel (P) configurations, respectively. This asymmetry is proportional to the spin polarization of the sample P_S , as discussed in Chapter 2.

Figure 3.7 shows an example. Figure 3.7(a) and (b) are two maps of the differential conductance of the Co island in the inset of Fig. 3.6(a) obtained at the same magnetic field of $+1.8$ T at anti-parallel and parallel magnetization configurations, respectively. Here, the differential conductance in the center region of the island is spatially modulated with a pattern, which reflects the symmetry of the island. This modulation is due to electron confinement [106]. The pattern can be ascribed to the formation of standing waves of the electronic density of states in the island surface, which is caused by scattering of electrons off the island boundaries [41,42]. The electron confinement within this Co island is studied in the next chapter. The modulation patterns in Fig. 3.7(a) and (b) are very similar but differ in the amplitude of the modulation. This difference is clearly displayed in the asymmetry image of the differential conductance of Fig. 3.7(c). The inner part shows a spatial modulation with a period which is determined by the electron dispersion relation of the Co island. The rim shows an opposite asymmetry and no distinct modulation. These results can be

interpreted as spin dependent quantum confinement within a single Co island as reported in ref. [95].

In conclusion, asymmetry maps of the differential conductance are a powerful technique to explore the spatial distribution of the sample spin polarization as it will be described in Section 6.1.1 and 6.1.2. Moreover, if the sample spin polarization is known, information about the tip spin polarization can be extracted as illustrated in section 7.3.

Chapter 4

Electron confinement in nanostructures on Ir(111) and Cu(111)

The growth and characterization of nanostructures is a very active research area in solid state physics. Detailed knowledge of the electronic behavior of nano particles gains interest not only from a fundamental standpoint but also in the view of technological applications. At this scale, electrons are confined to length scales approaching the de Broglie wavelength and quantum mechanical confinement phenomena play a dominant role in the electronic properties. For detailed investigation of electronic confinement in nano particles, simultaneous measurements of both the local geometrical and electronic properties are needed. This requirement is fulfilled by combining scanning tunneling microscopy (STM) and scanning tunneling spectroscopy (STS).

This chapter is divided in three sections. Section 4.1 focuses on nanometer-size graphene islands on Ir(111). The first experimental observation of electron confinement in graphene islands is presented [54, 107]. Energy-resolved maps of the differential conductance clearly show a spatial modulation indicating a modulated local density of states due to quantum confinement. The energy dispersion relation with quantized electron wave vectors is established. In Sections 4.2 and 4.3 electron confinement within Co islands and Fe-decorated Co islands grown on Cu(111) is presented. I present the first results which indicate how the decoration of the Co islands rim affects the electron confinement within the Co core. Although the dispersion relations are also quantized in both Co and Fe-decorated Co islands, the confinement in the two systems presents remarkable differences. Magnetism and spin-polarized effects of Fe-decorated Co islands are discussed in Chapter 6.

4.1 Graphene nano islands

Figure 4.1(A) shows graphene islands grown on Ir(111), which were prepared as described in Section 3.3.1. Constant-current STM images reveal that all islands have a uniform apparent height of $\simeq 0.2$ nm. The surface of the islands shows

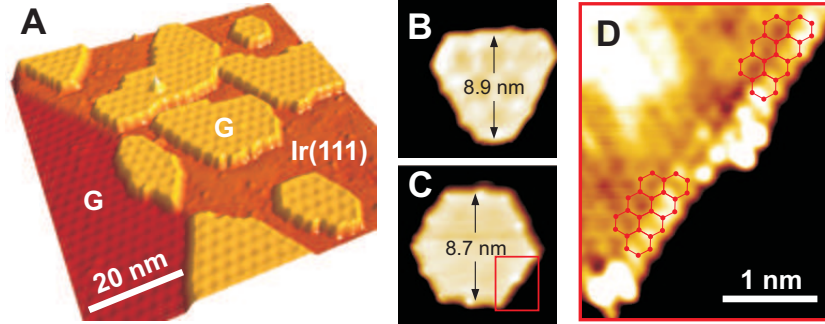


Figure 4.1: (A) Constant-current STM image of G islands grown on Ir(111). (B), (C) Constant-current STM images of the graphene nano islands where the electron confinement was investigated. (D) Atomically resolved constant-current STM image at the edge region marked by the red rectangular box in (C). The graphene honeycomb lattice model is superimposed. The edges of the graphene nano islands showed zigzag-type arrangements of carbon atoms in our experiments. Imaging parameters: $V_{gap} = +0.05$ V, $I_t = 1$ nA (A,B); $V_{gap} = +0.05$ V, $I_t = 2$ nA (C); $V_{gap} = +0.03$ V, $I_t = 2$ nA (D). Adopted from ref. [54]

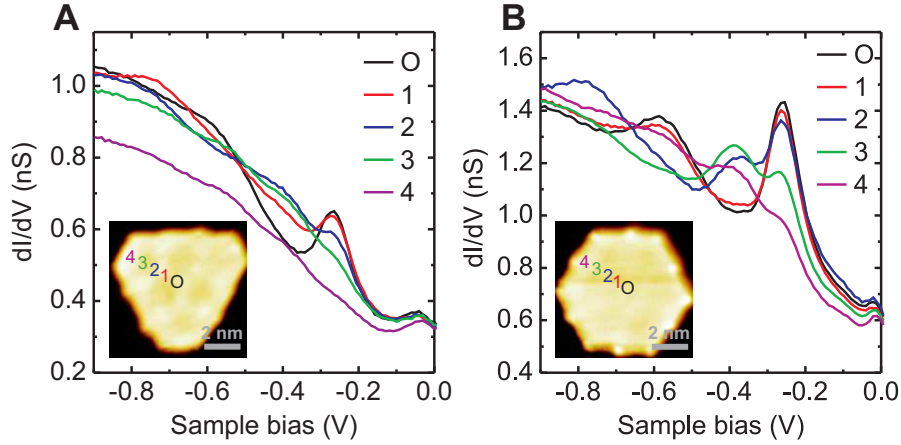


Figure 4.2: (A) Differential conductance dI/dV curves measured from the center toward a corner of the island in Fig. 4.1(B). (B) Differential conductance dI/dV curves measured from the center toward a side of the island in Fig. 4.1(C). The inset in each plot shows the constant-current STM image with the positions where the dI/dV curves were taken. Measurement parameters: $V_{stab} = +0.5$ V, $I_{stab} = 1$ nA, $V_{mod} = 20$ mV (A,B); $V_{gap} = +0.05$ V, $I_t = 1$ nA (insets of A and B). Adopted from ref. [54]

a spatial modulation with a periodicity of 2.52 ± 0.03 nm, regardless of size and shape of the G islands. This pattern is known as moiré structure, and it is ascribed to modulations of the electronic properties due to the graphene-substrate interaction. This specific periodic modulation of 2.52 nm arises from

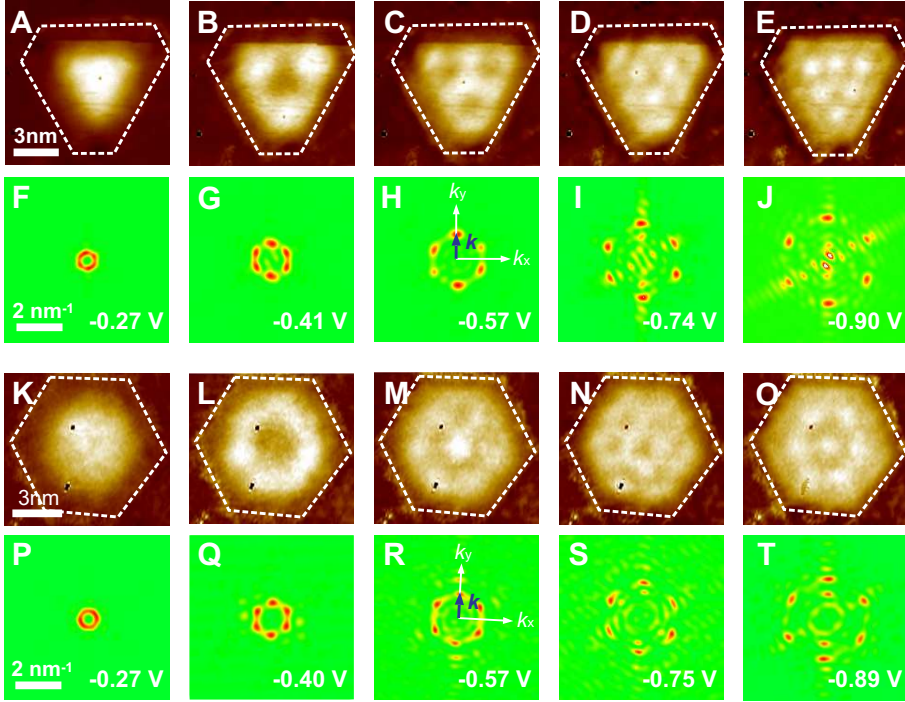


Figure 4.3: (A-J) Maps of the differential conductance dI/dV (A-E) and corresponding FT intensity maps (F-J) obtained from the island in Fig. 4.1(B). (K-T) Maps of the differential conductance dI/dV (K-O) and corresponding FT intensity maps (P-T) obtained from the island in Fig. 4.1(C). The bias voltage of each map of the differential conductance is denoted at the bottom-right side of the corresponding FT map. Dotted polygons in A-E and K-O indicate the boundaries of the nano islands, as determined from the STM images in Fig. 4.1(B), (C), respectively. Measurement parameters: $V_{stab} = +0.5$ V, $I_{stab} = 1$ nA, $V_{mod} = 20$ mV. Adopted from ref. [54]

the superposition of the graphene and Ir(111) lattices [108]. The monoatomic apparent height and the moiré pattern identify the formation of epitaxially ordered graphene islands. Figure 4.1(B,C) shows two graphene nano islands on which the measurements were taken. Figure 4.1(D) shows an atomic resolution image near the edge of the island in Fig. 4.1(C) showing the zigzag arrangement of the outermost carbon atoms.

Figure 4.2(A,B) shows differential conductance dI/dV curves measured at different positions along the most symmetric directions of the islands shown in Fig. 4.1(B,C), respectively. As the measurement position moves from the center to the border, the curves clearly show a decrease in the amplitudes of the first peak at a sample bias of -0.27 V and an increase in the amplitudes of the second peak at -0.41 V. These voltage dependent and spatially modulated differential conductance dI/dV signals are ascribed to electron confinement, which induces a corresponding spatial modulation of the LDOS [44, 51].

To provide clear evidence for electron confinement, maps of the differential conductance at different sample bias were measured. Figure 4.3(A-E)

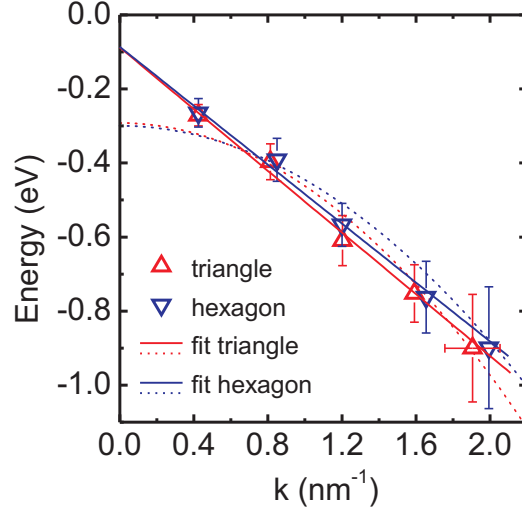


Figure 4.4: Dispersion relation $E(k)$ extracted from the maps of the differential conductance of the islands in Fig. 4.1(B) (Fig. 4.3(A-E)) and Fig. 4.1(C) (Fig. 4.3(K-O)), named triangle and hexagon, respectively. The data points for each island were fitted with the linear dispersion relation $E = E_D - \hbar v_F |k|$ (solid line), predicted by the tight-binding model of graphene [109,110], and with the parabolic dispersion relation $E = E_0 + \hbar^2 k^2 / 2m^*$ (dotted line) describing the free-electron-like behavior of the electronic surface states. Adopted from ref. [54]

(Fig. 4.3(K-O)) and Fig. 4.3(F-J) (Fig. 4.3(P-T)) show the maps of the differential conductance and their Fourier transform (FT) intensities of the patterns inside the islands of Fig. 4.1(B) (Fig. 4.1(C)). As the sample bias is lowered from zero bias, the first modulation pattern (Fig. 4.3(A)) is observed at -0.27 V. Here, the differential conductance dI/dV signal shows a maximum at the center and a monotonic decrease toward the border of the islands. For larger negative sample biases, four more distinct modulation patterns are identified (Fig. 4.3(B,E)). The patterns at lower sample bias show an increasing number of modulations over the area of the island. The modulation can be understood as a standing wave pattern resulting from the interference of electron waves. These findings suggest a decrease in the electron wavelength (increase in the electron wave vector) toward larger negative energy, as shown in Fig. 4.4. For the island in Fig. 4.1(C), a similar tendency in both differential conductance dI/dV and FT maps is observed, as shown in Fig. 4.3(K,T).

Interestingly, the energy intervals between any two neighboring patterns in Fig. 4.3 are identical within our experimental accuracy, with an average separation of 0.16 eV. This marks a distinct difference between the energy dependence of dI/dV modulation patterns of graphene nano islands as compared to those of metallic nano structures [44, 46, 111], which are also discussed in the next Sections 4.2 and 4.3.

The energies of the patterns of Fig. 4.3 are selected to show the largest intensity of the specific k-point. Indeed, the intensity of a given k-point of the

FT map varies with energy. Also, the position does not vary continuously with energy but changes in a discrete manner [46]. In 2D electron systems, the radial average of the FT map has been used to determine the in-plane wave vector k_{\parallel} of a standing wave pattern [111–113]. Under the same strategy, the average of the k for the sixfold symmetric pattern in each FT map was taken as the magnitude of wave vector for each modulation pattern in Fig. 4.3(A,E) (Fig. 4.3(K,O)).

Figure 4.4 shows the dispersion relation $E(k)$ obtained from the extracted wave vector of the Fourier analysis and the corresponding energy from the modulation patterns of the differential conductance shown in Fig. 4.3. The discrete nature of the wave vector is apparent, which is a signature of the confinement. Also, the wave vector increases monotonically as the electron energy gets more negative. Both linear and parabolic fits through to data points were performed, and they are shown in Fig. 4.4. The linear dispersion relation $E = E_D - \hbar v_F |k|$ is predicted by the tight-binding model of graphene [109, 110]. A linear fit through the data points gives $E_D = -0.088 \pm 0.022$ eV (-0.086 ± 0.021 eV) and $v_F = (6.3 \pm 0.40) \times 10^5$ m/s ($(6.0 \pm 0.38) \times 10^5$ m/s) for the island in Fig. 4.1(B) (Fig. 4.1(C)). For the typical free-electron-like behavior of the electronic surface states, the parabola can be described by the dispersion relation $E = E_0 + \hbar^2 k^2 / 2m^*$ [114]. The fit through the data points results in $E_0 = -0.29 \pm 0.04$ ($E_0 = -0.30 \pm 0.04$) and $m^* = 0.22 \pm 0.02 m_e$ ($m^* = 0.25 \pm 0.02 m_e$) for the island in Fig. 4.1(B) (Fig. 4.1(C)). Apparently, the linear fit describes better our data.

These results clearly show the observation of electron confinement in graphene nano islands on Ir(111) for the first time [54], a detailed discussion is given in Section 7.1.

4.2 Co nano islands

The results on electron confinement effects within approximately triangular two-atomic-layers-high Co islands grown on Cu(111) are presented here. Although this topic has already been investigated before at the MPI Halle [75], the present section is necessary to compare the electron confinement within Co islands with the electron confinement within Fe-decorated Co islands (see Section 4.3). Moreover, from the measurements in ref. [75], no clear distinction between a parabolic and a linear dispersion relation $E(k)$ of the Co surface states was possible due to the limited k -range of data. The new measurements performed here lead to a clarification of this open aspect.

Figure 4.5(a) shows a constant current STM image of the investigated island. The island has the shape of a truncated triangle with a base length of about 13 nm. A series of maps of the differential conductance recorded at different sample bias is presented in Fig. 4.5(b),(d-f). Pronounced modulation patterns within the island can be observed. These patterns become more complex with increasing energy, similar to the results of graphene islands presented in Section 4.1. The appearance of the patterns is ascribed to the confinement of surface state electrons within the island. Figure 4.5(c) shows the FT map of the truncated triangular area of interest in (b). The three symmetry axes of the triangle A, B and C are highlighted in the images. The energies of the patterns of Fig. 4.5(b),(d-f) are selected to show the largest intensity of the specific k -point. Indeed, the intensity of a given k -point of the FT map varies with

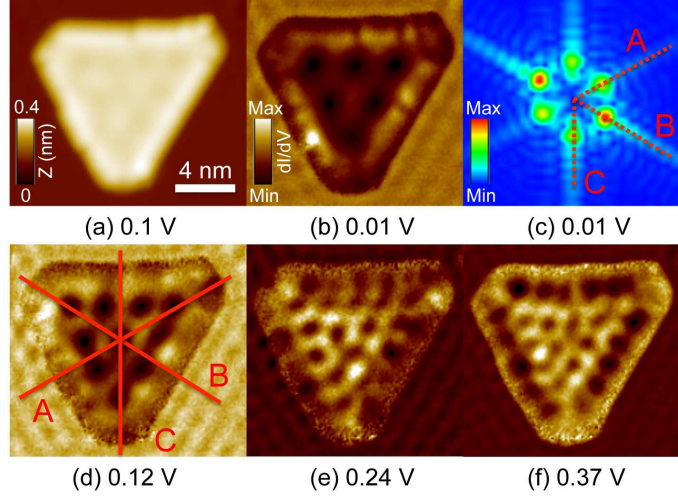


Figure 4.5: (a) Constant-current STM image of a Co island on Cu(111). (b), (d-f) Maps of the differential conductance at different bias voltages. Note that the distinct modulation pattern is only apparent in the center region of the island, and not close to the rim. This differs from Fig. 4.7. Solid red lines in (d) show the directions three heights of the triangular island. Dashed red lines in (c) show where the directions A-C appear in the FFT map of (c). Measurements parameters: $V_{gap} = +0.1$ V, $I_t = 1$ nA (a); $V_{stab} = +0.5$ V, $I_{stab} = 1$, $V_{mod} = 20$ mV, $T = 10$ K, bulk Cr tip.

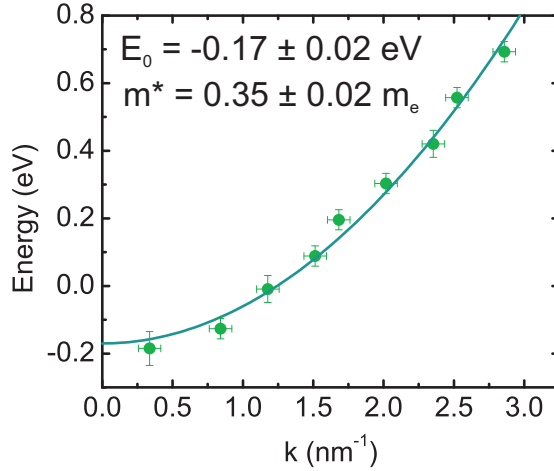


Figure 4.6: Dispersion relation $E(k)$ of the Co surface state electrons along the direction C extracted from the FFT analysis of dI/dV spectroscopy maps. E_0 and m^* are extracted from the fit of the plots for each island with the equation $E = E_0 + \hbar^2 k^2 / 2m^*$. Note that the k -values are discrete, as discussed in Section 7.2.

energy. Also, the position does not vary continuously with energy but changes in a discrete manner.

The FT analysis of maps of the differential conductance in the bias range of -0.3 to $+0.8$ V yields the dispersion relations $E(k)$. The dispersion relation $E(k)$ along the direction C is shown in Fig. 4.6. The discrete data points are described reasonably well by a parabola. Assuming a free-electron-like behavior typical of the electronic surface states, the parabola can be described by the equation $E = E_0 + \hbar^2 k^2 / 2m^*$ [114]. The fit through the data points results in $E_0 = -0.17 \pm 0.02$ and $m^* = 0.35 \pm 0.02 m_e$. In Section 7.2, the dispersion relation is discussed and a detailed analysis of the confinement is presented. Here, the new aspect is that the confinement analysis is extended to small wave vectors ($k \leq 1 \text{ nm}^{-1}$), whereas previous data were confined to a more limited range of wave vectors [75].

4.3 Fe-decorated Co nano islands

The characteristic standing wave pattern already shown in Section 4.1 and 4.2 is formed by quantum interference of electrons scattered off the edges of nanostructures. One can expect that modifying the borders of a nanostructure can influence the confining potential and therefore the shape and characteristics of the wave pattern. Moreover, Co islands present peculiar electronic properties at the edges, the so-called rim state [95,106,115], which seems to play a role in the position of the confining potential within the island (see discussion in Section 7.2). Decorating the Co islands with another material is expected to modify the rim of the nano structure. This novel approach is followed here to present for the first time how edge decoration affects the electron confinement. In this case, Fe was chosen to decorate the Co edge. This section deals only with the confinement of the Co surface states within the Co core, accurate studies of the spin polarized electronic and magnetic properties of the system are presented in Section 6.3 and 7.2.

Figure 4.7(a) shows a constant-current STM image of a Fe-decorated Co island prepared as described in Section 3.3.1. In Fig. 4.7(b), the constant current STM image of the area highlighted in Fig. 4.7(a) is shown. Here, the three symmetry axes of the inner triangular Co core A, B and C are indicated. A series of differential conductance maps showing the first four modes is presented in Fig. 4.7(c-f). The yellow dashed line in Fig. 4.7(a-f) indicates the border of the Co core extracted by analyzing the position dependence of the spectra of the differential conductance as it is shown in Section 7.2. The Co core has the shape of a truncated triangle with a geometrical height of approximately 5.7 nm. Already at this point, a clear difference between the wave pattern within a Co island and that within the Co core of a Fe-decorated Co island can be noted comparing Fig. 4.5(b),(d-f) and Fig. 4.7(c-f). The wave pattern within the Co core of a Fe-decorated Co island extends all the way to the border between Co and Fe (see in particular Fig. 4.7(e,f)), whereas the wave pattern in a Co island is confined within a smaller region in respect to the extension of the whole island.

A FT analysis was performed as already explained in Section 4.1 and 4.2. The dispersion relation were extracted for each direction and the result of direction C is shown in Fig. 4.8. Here, due to the small size of the Co core (and

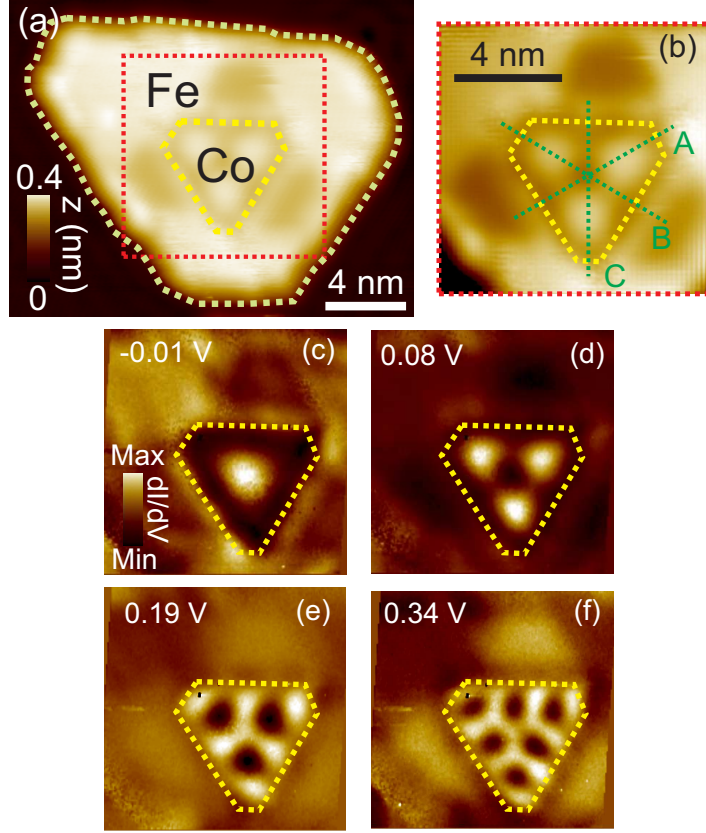


Figure 4.7: (a) Constant current STM image of a Fe-decorated Co island on Cu(111). (b) Constant current STM image of the area marked by the red dashed line in (a). The yellow dashed line indicates the Co core of the Fe-decorated Co island. Green dashed lines show the directions of the three geometrical heights of the triangular Co core, along which the dispersion relations were extracted. (c-f) Maps of the differential conductance at different bias voltages showing the interference patterns of the first four modes. Note that in contrast to Fig. 4.5 the modulation extends all the way to the border of the Co core. Imaging parameters: $V_{gap} = +0.1$ V, $I_t = 1$ nA (a,b); $V_{stab} = +0.5$ V, $I_{stab} = 1$ nA (c-f), $V_{gap} = -0.01$ V (c), $V_{gap} = +0.08$ V (d), $V_{gap} = +0.19$ V (e), $V_{gap} = +0.34$ V (f), $T = 10$ K, bulk Cr tip.

therefore of the quantum well), the modes are wider spaced in energy and only four of them can be observed in the studied voltage range. This is readily understood considering that, for a free particle in a one-dimensional particle-in-a-box model, the energy intervals between two consecutive modes are inversely proportional to the square of the confining length [116]. Here, the confining length is related to the size of the Co core (or of the Co island), as discussed in Section 7.2. Since the Co core of the Fe-decorated Co island in Fig. 4.7(a) is fairly smaller than the Co island in Fig. 4.5(a), we can qualitatively understand why seven modes are observed in the energy range between -0.2 V and $+0.4$ V in

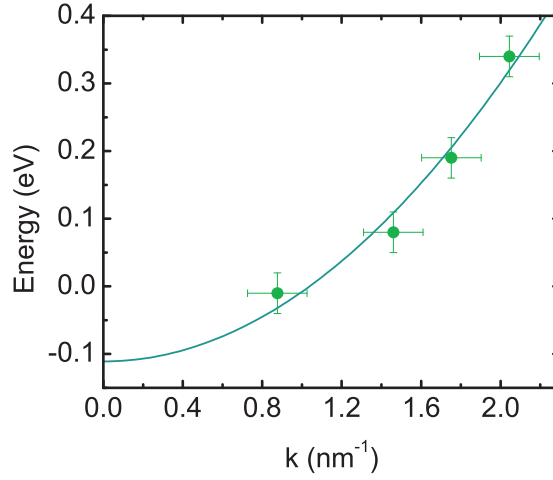


Figure 4.8: Dispersion relation $E(k)$ of the Co core surface state electrons along the direction C extracted from the FFT analysis of dI/dV spectroscopy maps. E_0 and m^* are extracted from the fit of the data with the equation $E = E_0 + \hbar^2 k^2 / 2m^*$.

Fig. 4.6, whereas only four modes are observed in the same energy interval in Fig. 4.8. Using the same free-electron-like model used before, the fit through the data points results in $E_0 = -0.11 \pm 0.03$ and $m^* = 0.34 \pm 0.03 m_e$. A detailed discussion of the comparison between confinement in pure Co islands and in Fe-decorated Co island is presented in Section 7.2.

Chapter 5

Characterization of bulk Cr and Fe-coated W tips for spin-polarized STM: spin polarization and temperature dependent measurements

In spite of the numerous results that illustrate the success of spin-STM in nano magnetism [25, 34–36, 38, 77, 84, 93, 95, 97], only a small number of studies on the decisive role of the tip in this technique have been presented so far [79–81]. A big challenge in sp-STM is the preparation and characterization of magnetic tips. Generally, W tips covered with a thin film of a magnetic material (Co, Fe, Gd, Cr) are used [34, 117]. As described in Section 3.3.2 for Fe-covered W tips, the preparation of these tips requires a multi-step preparation involving several steps performed both ex-situ and in-situ preparation. However, the macroscopic preparation of magnetic tips does not directly ensure magnetic sensitivity routinely. Therefore an additional microscopic preparation by the application of voltage pulses between sample and tip under tunneling conditions is applied. Once a magnetic sensitivity is achieved, the spin direction of the tip apex can differ from tip apex to tip apex. Also, the magnetic response of the specific tip apex to the applied magnetic field may vary. Thus, one can understand that a main challenge of spin-STM is the characterization of the magnetic configuration of the tip apex, in order to draw reliable conclusion about the spin structure of the sample [79]. The magnetic configuration of the tip is expected to be determined by the exact atomic configuration of the tip apex, which is, however, not straightforwardly accessible experimentally. Therefore, further insight into tip preparation and how to determine the magnetic behavior of the tip apex is called for, and corresponding experiments are presented here.

In this chapter, bulk Cr tips and Fe-coated W tips for in-situ sp-STM are

investigated. Bulk Cr tips require an easy fabrication process, which makes them excellent candidates for sp-STM probes. In the second section of the chapter, temperature dependent measurements on Fe-coated W tips are performed to obtain insights into the temperature dependence of the magnetic response of the tip apex to the applied magnetic field.

5.1 Bulk Cr tips

Tips made of bulk antiferromagnetic materials such as Cr [118–120] have been proposed for sp-STM and have recently been shown to provide magnetic contrast on Cr(001) and Fe/W(110) [83, 121]. As it was already pointed out in Section 3.3.2, in contrast to W tips covered with an ultra-thin film of antiferromagnetic material [34, 117, 122], they present the advantage of a simpler preparation which does not require a dedicated in-situ tip preparation stage. Bulk Cr tips do not require either high-temperature flashing or material deposition. The tips were prepared by a simple electrochemical etching performed ex-situ, as described in Section 3.3.2. A scanning electron microscope image (SEM) of a Cr tip¹ is shown in Fig 5.1. The tip apex has a macroscopic radius of about 40 nm. In spite of this fairly large radius of curvature, resolution at the atomic scale is still obtained. This is ascribed to nm small clusters at the tip apex, which ensure high spatial resolution but which are not resolved in this SEM image.

The only in-situ preparation of the tip consisted of the application of voltage pulses between tip and sample during STM experiments. Voltage pulses were applied only on the clean Cu surface to ensure the absence of any potential Co contamination on the tip apex. In order to characterize these tips, we performed sp-STs measurements on Co islands on Cu(111), a system for which the electronic and magnetic properties have been thoroughly characterized [95, 105, 111, 115]. The Co islands have an out-of-plane easy magnetization axis and the energy-dependent spin polarization of Co islands has been measured and accounted for by *ab initio* calculations [95].

Figure 5.2 shows spectra of the differential conductance dI/dV taken on the

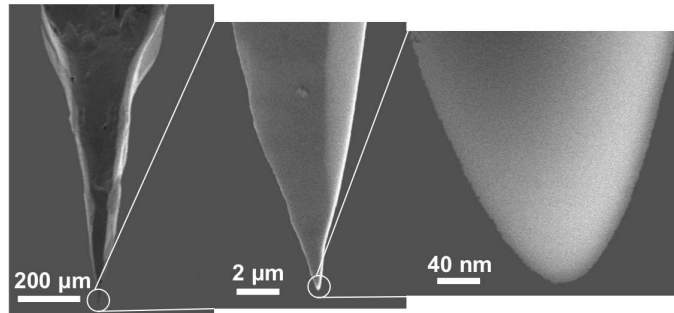


Figure 5.1: SEM image of a typical bulk Cr tip which was electrochemically etched from a Cr foil as described in Section 3.3.2.

¹The SEM image of this bulk Cr tip was kindly provided by W. Erfurth from the Max-Planck-Institute of Halle.

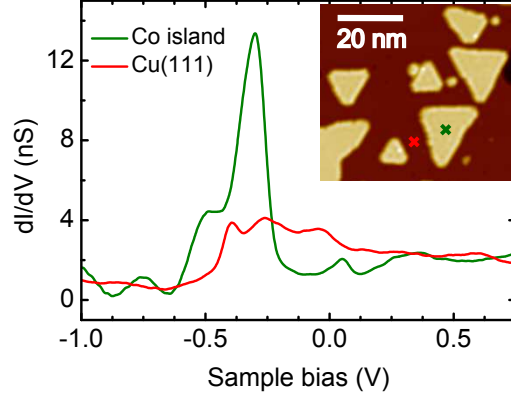


Figure 5.2: Spectra of the differential conductance $dI/dV(V)$ measured with a bulk Cr tip at the center of the marked Co island (green) and on the Cu(111) surface (red). Stabilization parameters: $V_{gap} = +0.5$ V and $I_t = 1$ nA, $T = 10$ K. Inset: constant-current STM image ($V_{gap} = +0.1$ V, $I_t = 1$ nA) of two-atomic-layer-high (0.4 nm) Co nano islands on Cu(111). The green and red marks indicate the positions where the two differential conductance $dI/dV(V)$ spectra were taken. Adopted from ref. [80]

Cu surface and on a Co island. The positions where the two spectra were taken are indicated in the inset. The dI/dV spectra taken on Cu(111) shows a step at -0.44 V and a pronounced peak at -0.3 V in the spectra obtained on the Co island can be observed. Both these features were reported in previous studies and correspond to the onset of the Cu surface state [39] and the occupied d_{z^2} -like Co surface state respectively [111]. Also the smaller features at -0.5 and $+0.3$ V in the Co island spectra were interpreted as sample-related peaks [105, 111, 115]. The spectroscopy measurements on Co and Cu using a bulk Cr tip revealed the intrinsic electronic properties of Co and Cu. The spectra are very similar to those obtained with W and Cr-covered W tips [75, 79, 122]. Thus, we may conclude that the tip shows a rather flat local density of states over the energy range of the spectroscopy measurements.

Figure 5.3(a) shows spectra of the differential conductance at different applied magnetic fields measured at the center of the Co island marked in Fig. 5.2. Clear differences in the shape and amplitude of the spectra were found, although the main features are similar for all voltages. Increasing the applied magnetic field from 0 to 2.3 T, the dI/dV signal at -0.5 V decreases in intensity and then sharply increases at an applied field of 2.5 T. The field-induced change in the dI/dV signal of the main peak located at -0.3 V is opposite in sign to that of the shoulder at -0.5 V. In order to link the magnetic field dependence of the differential conductance to the magnetic properties of the tunneling system (tip + sample), spectra of the differential conductance $dI/dV(V)$ were recorded at different field values during a complete cycle of the applied magnetic field. Extracting the magnitude of the differential conductance signal at a fixed bias

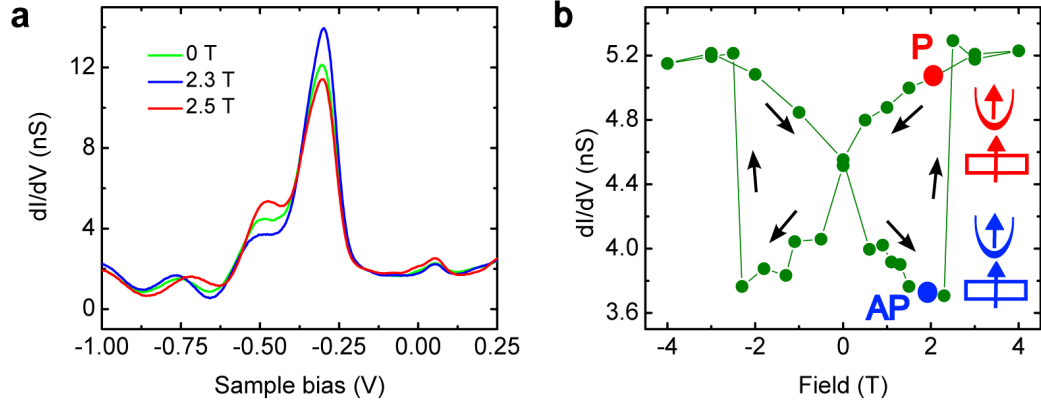


Figure 5.3: (a) Spectra of the differential conductance $dI/dV(V)$ measured at the center of the Co island marked in Fig. 5.2 at different magnetic fields. (b) Hysteresis loop of the differential conductance measured on the Co island in Fig. 5.2 ($V_{gap} = -0.5$ V). Arrows indicate the sequence in which the data were measured. Red and blue points respectively indicate parallel (P) and anti-parallel (AP) states between the magnetization direction of tip and sample at +1.8 T where the asymmetry of the differential conductance shown in Fig. 7.9 was measured. $T = 10$ K, bulk Cr tip.

as a function of the field yielded the hysteresis loop shown in Fig. 5.3(b). The differential conductance dI/dV changes gradually with increasing field and at a critical applied magnetic field of 2.4 T, it changes abruptly. A butterfly hysteresis cycle results, which has been observed in previous studies using Cr-coated W tips [79,122]. As already discussed in Section 3.4, the abrupt change in the differential conductance dI/dV is ascribed to the reversal of the magnetization direction of the Co island, whereas the gradual change is ascribed to a continuous increase of the z-component of the local magnetic moment of the tip apex towards the field direction.

In conclusion, in this section I showed that bulk Cr tips can be used for in-situ sp-STM measurements. In Section 7.3, the tip spin polarization is extracted and a detailed discussion of obtained results is presented.

5.2 Temperature dependent measurements using Fe-coated W tips

This Section presents temperature-dependent measurements which were performed to clarify the magnetic response of Fe-coated W tips used to study the spin-dependent electronic properties of Fe and Fe-decorated Co islands in Section 6.3. As it is shown in Section 6.3, Fe on Cu(111) presents spatial periodic modulations of the differential conductance dI/dV in maps of the differential conductance taken in-field with spin-polarized tips. In order to draw reliable conclusions about the spin structure of the sample, the direction of the tip magnetic moment and its response to the magnetic field must be known unequivocally. The measurements shown in this Section were taken with a W tip

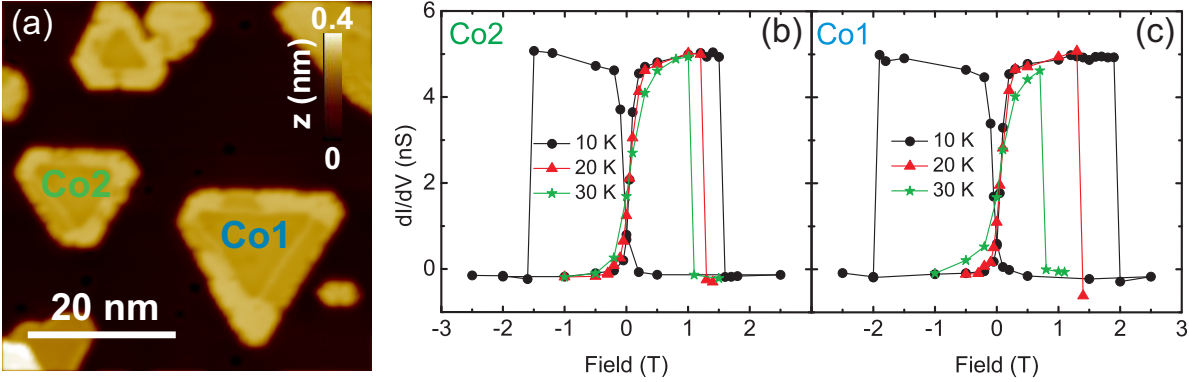


Figure 5.4: (a) Constant current STM image of the two Fe-decorated Co islands on which the magnetic field dependence of the differential conductance dI/dV in (b) and (c) were taken. (b), (c) Magnetic field dependence of the differential conductance measured at the center of the Co core of the two Fe-decorated Co islands in (a) at temperature of 10, 20 and 30 K. W tip covered with 40 atomic layers of Fe was used.

covered with 40 atomic layers of Fe.

To characterize the tip, the dependence of the differential conductance dI/dV on the magnetic field were measured on the Co cores of the two Fe-decorated Co islands of Fig. 5.4(a) as already described in Section 3.4 and 5.1. The black dI/dV hysteresis curves were obtained at 10 K and present the same butterfly shape as those obtained on pure Co islands. Therefore, it is justified to assume that the abrupt changes in the differential conductance at 1.6 and 2 T are ascribed to the reversal of the magnetization direction of the Co cores, whereas the gradual change is ascribed to a continuous increase of the z-component of the local magnetic moment of the tip apex towards the field direction, as already discussed in previous sections.

From the measurements at 10 K only, it is not clear a priori whether the increase of the z-component of the magnetic moment of the tip apex is due to its rotation from the in-plane to out-of-plane direction or due to a superparamagnetic response. Both scenarios are possible. In order to shed light on this issue, the magnetic field dependence of the differential conductance taken on the same Co cores was measured at different temperatures. Indeed, the two proposed physical processes are expected to produce two different temperature dependent effects [123–125].

Figure 5.4(b,c) show the magnetic field dependence of the differential conductance measured at the center of the Co cores of two Fe-decorated Co islands in Fig. 5.4(a). The measurements were performed at 10, 20 and 30 K. Only at 10 K complete cycles were measured, due to time limitations. A complete hysteresis cycle with 40 points takes about 6 hours. The consumption of LHe drastically increases with increasing temperature, and the measurements had to be concluded before emptying the LHe tank. The most evident difference between the measurements is the drastic change of the switching fields of the Co cores with temperature. This change in the switching field is expected for the

Co core, as with increasing temperature the thermally assisted reversal of the Co core becomes more apparent. This effect can be quantitatively described [77] and the observed reduction of switching field is ascribed to this effect. This aspect is discussed in Section 7.7.2.

Another temperature effect is the change in curvature of the magnetic field dependence of the differential conductance dI/dV between ± 1 T. This second temperature dependent effect is the key point to distinguish between the two mentioned physical mechanisms which could bring the tip apex magnetic moment to increase its component into the z-direction, parallel to the sample magnetization. A detailed discussion is presented in Section 7.4. We already note here that the temperature dependence of the differential conductance signal at small fields indicates a superparamagnetic response of the tip apex magnetic moment.

Chapter 6

Magnetic properties of Co and Fe nanostructures on Cu(111)

This chapter presents the results of the magnetic properties of the Co and Fe nanostructures investigated in this thesis. It is divided in three main sections. The first Section 6.1 focuses on the spatial dependence of spin-polarized electronic states near the edges of Co nano islands. An attempt to measure the induced spin polarization in Cu surface states in proximity of Co islands is performed, and first clear evidence of the existence of a spin-dependent Smoluchowski effect is shown. In Section 6.2, a study of the island size dependence of the switching field for individual Co islands and Fe-decorated Co islands is reported. Subsequently in Section 6.3, the magnetic order of Fe islands and at the Fe-rim of Fe-decorated Co islands is investigated. Two different magnetic phases with distinct spin-dependent electronic properties are found for these bilayer Fe nanostructures on Cu(111).

6.1 Spatial dependence of the spin-polarized electronic properties near the edges of Co nano islands

Several experimental and theoretical studies have evidenced the existence of spin-polarized surface states on transition metal substrates [126–133]. On the other hand, when magnetic nano islands grow on a nonmagnetic substrate charge transfer, electronic scattering and interference phenomena generally govern the electronic and the magnetic properties of the combined system. *Ab-initio* calculations show that surface states of nonmagnetic noble metals, such as Cu(111), turn spin polarized and attain a different character when Co atoms are added to the substrate surface [134–137]. Such spin-polarized surface states can serve as spin-transport channels across the vacuum barrier to or from another magnetic material. This issue is of central importance for spintronic applications based on spin-polarized tunneling. In Section 6.1.1 measurements of the

spin polarization of the Cu states close to the edge of Co islands are presented. Section 6.1.2 introduces the basis for a novel way to tune spin-dependent transport at the edges of magnetic nano structures by exploiting the spin-dependent Smoluchowski effect.

6.1.1 Induced spin polarization in Cu near Co islands

When magnetic materials are deposited on a nonmagnetic substrate, a magnetic moment may be induced in the atoms of the substrate [138–143]. The induced magnetic moment affects the properties of the system and it is expected to polarize the surface states of the substrate [134–136, 144]. In this section, a measurement of the induced spin polarization of the Cu surface states in a Cu channel in between two Co islands is performed. This is experimentally demanding, as theory suggests that the induced spin polarization in Cu is very small, on the order of a few percent (see Section 7.5).

Figure 6.1(a) shows a constant-current STM image of the system investigated. The measurements are performed in a Cu channel in between two parallel edges of two Co islands. Figure 6.1(b) shows a map of the differential conductance dI/dV of the same area, a clear modulation pattern is visible in the differential conductance signal on both Co islands and in the Cu channel in between the Co islands. The inset in Fig. 6.1(b) shows the line profile along the blue line, the modulation of the dI/dV signal in the Cu channel reflects the quantum interference of the Cu surface state electrons. If a sizable spin polarization is induced by the Co islands in the Cu substrate, the standing wave pattern of the Cu surface states (and therefore the dI/dV signal in the Cu channel) is expected to be spin-polarized.

In order to check this expectation, spectra of the differential conductance dI/dV along the blue line in Fig. 6.1(a) were measured for states of parallel and

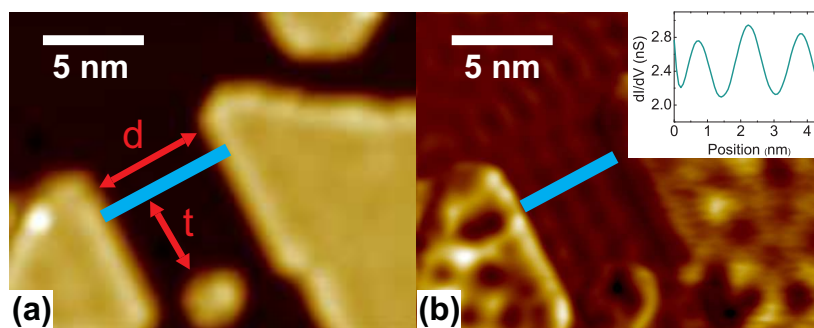


Figure 6.1: (a) Constant current image ($V_{gap} = +0.1$ V, $I_t = 1$ nA) of the studied Cu channel between two Co islands ($d = 5.5$ nm). The blue line indicates the line which has been scanned repeatedly to measure the asymmetry of the differential conductance. In order to ensure to scan always the same line, in both parallel and anti-parallel state, we fixed the distance from the cluster $t = 6$ nm in both measurements. (b) Map of the differential conductance ($V_{gap} = +0.1$ V, $I_t = 1$ nA) of the same area of (a). The blue line shows the direction along which the line profile in the inset have been measured.

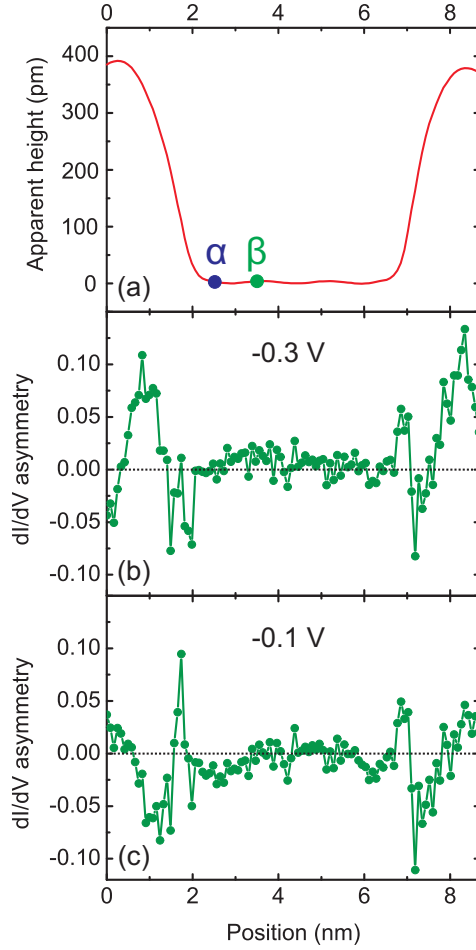


Figure 6.2: (a) Line profile along the blue line marked in the constant current image of Fig. 6.1(a). (b), (c) dI/dV asymmetry $A = (dI/dV_{AP} - dI/dV_P)/(dI/dV_{AP} + dI/dV_P)$ line profiles of the blue line showed in Fig. 6.1(a) at -0.3 V and -0.1 V. α and β indicate the two points in the Cu channel to which the two graphs in Fig. 6.3 refer.

anti-parallel orientation between tip magnetic moment and the magnetization of the two Co islands, as verified from hysteresis curves of the differential conductance measured on both islands. Measurements were performed along a line perpendicular to the edge of the Co islands and at a distance $t = 6$ nm from the cluster at the bottom of the Cu channel. The asymmetry A of the differential conductance along the blue line in Fig. 6.1(a) was extracted. This asymmetry is proportional to the spin polarization of the sample, as explained in Chapter 2. Figure 6.2(a) shows a constant-current line profile of the blue line in fig. 6.1(a) along which the asymmetry of the differential conductance was calculated. Two line profiles of the asymmetry of the differential conductance, averaged over 6 measurements of the same line, are shown in Fig. 6.2(b,c) for -0.3 and -0.1 V, respectively. The data reveal a spatial variation of the asymmetry of the differ-

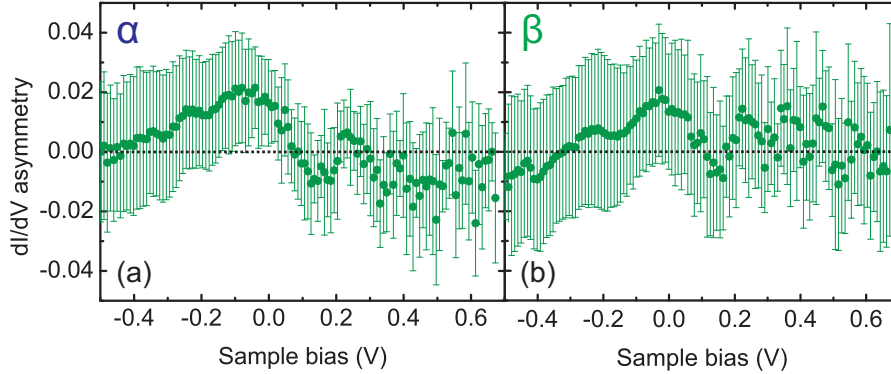


Figure 6.3: Asymmetry of the differential conductance dI/dV as function of sample bias for two points in the Cu channel situated 1 nm (a) and 2 nm (b) away from the edge of the Co island at the left side of Fig. 6.1, as indicated by the labels α and β in Fig. 6.2(a).

ential conductance which is pronounced along the edge of the Co islands, i.e. at positions below 2 nm and above 7 nm. No clear modulation nor deviation from the zero line of the signal can be observed in view of the experimental scatter in the Cu channel. The comparably pronounced variation of the asymmetry of the differential conductance along the edges of the Co islands is treated in the next section and indicates a spin-dependent Smoluchowski effect.

To give an upper limit to magnitude of the induced spin polarization of the Cu surface states within the channel, the statistical error in the extraction of the asymmetry of the differential conductance was estimated. Figure 6.3 shows the asymmetry of the differential conductance as function of sample bias for two points in the Cu channel situated 1 nm (Fig. 6.3(a)) and 2 nm (Fig. 6.3(b)) away from the edge of the Co island at the left side of Fig. 6.1(a). The standard variation of the measurement varies between 0.015 and 0.03 depending on the sample bias. The asymmetry of the differential conductance seems to have positive values up to 0 V and then no clear tendency is visible. However, the measured value of the asymmetry of the differential conductance ranges between -0.02 and $+0.02$, which are values as big as the statistical error of the measurement. Further discussion of the measurement and an estimate by *ab-initio* calculations of the induced spin polarization of Cu surface states near the edge of a Co island are presented in Section 7.5.

6.1.2 Spin-dependent Smoluchowski effect

The spreading and smoothing of electron charge density above atomically sharp surface corrugations as described by Smoluchowski [60] is a well established picture in solid state physics, which has significant implications in wide areas of surface science [145–150]. The typical feature of the Smoluchowski effect is that the spatial corrugation of the atomic cores deviates from that of the electronic charge density. As it was revealed by thermal energy He-atom scattering [151], the latter shows a more smoothed behavior as compared to the former. The works cited above provided an exhaustive picture of the electronic charge redis-

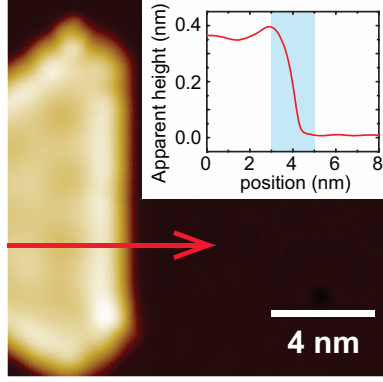


Figure 6.4: Constant current image ($V_{gap} = +0.1$ V, $I_t = 1$ nA, $T = 10$ K, bulk Cr tip) at the edge of a two-atomic-layer-high Co nano island on Cu(111). Inset: line profile along the red line indicated in the figure. The highlighted area indicate the extension of Co island step edge region of the dI/dV asymmetry line profiles in Fig. 6.5. Adopted from ref. [61].

tribution at the surface corrugations and its influence on physical and chemical properties. However, the previous works focus on the total electronic charge density and the effect of the electron spin was neglected. Spin-polarized materials show a different energy dependence of the local density of states (LDOS) for majority and minority electrons and it is a priori not clear how majority and minority states contribute to the spin-dependence of the Smoluchowski effect [60,61].

Spin-polarized STS is the method of choice to determine the spin-polarization above nano structures with high spatial resolution. In order to check the existence of a spin-polarized Smoluchowski effect, measurements of the spin polarization above the edge of the bilayer Co island on Cu(111) of Fig. 6.4 were performed. Figure 6.5 shows a constant current STM image of the step edge

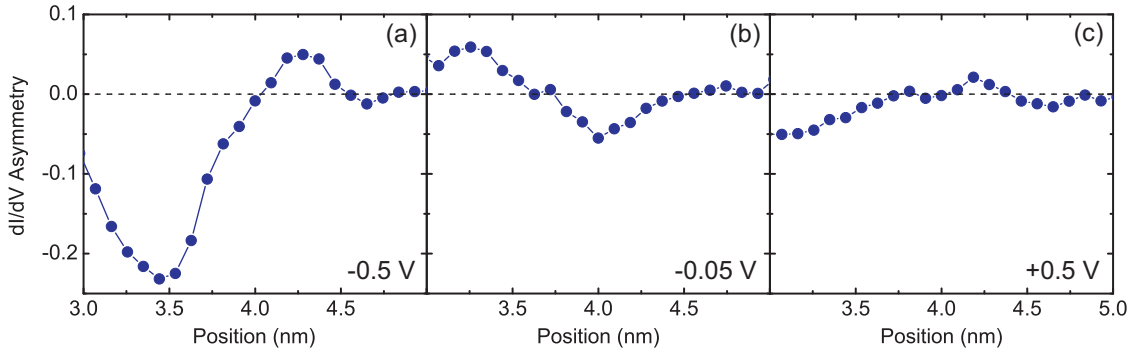


Figure 6.5: Differential conductance dI/dV asymmetry line profiles measured at different gap voltages applied to the sample of the tunnel junction with reference to the tip. Gap voltage (a) -0.5 V, (b) -0.05 V, (c) $+0.5$ V. The line profile is measured along the red arrow in Fig. 6.4. Adopted from ref. [61].

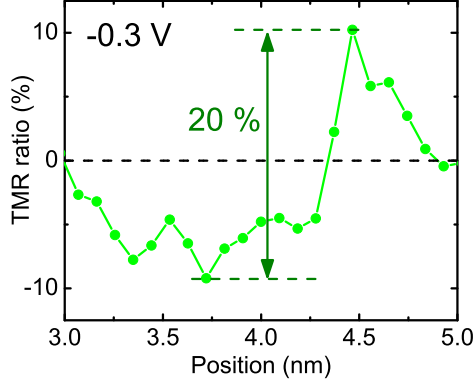


Figure 6.6: Line scan of the tunnel magneto resistance ratio (TMR) measured along the red arrow in fig. 6.4 at a gap voltage between sample and tip of -0.3 V. Adopted from ref. [61].

and a line scan of the apparent height across the step edge. Maps of the differential conductance dI/dV for states of parallel (P) and anti-parallel (AP) orientation between tip and sample magnetization were measured. From these maps, the asymmetry A of the differential conductance was extracted as explained in Section 3.4. This asymmetry is proportional to the spin polarization of the sample [34, 94, 95], as pointed out in Chapter 2.

Three line profiles of the asymmetry of the differential conductance, averaged over six adjacent lines next to the red arrow of Fig. 6.4, are shown in Fig. 6.5(a-c) for different bias voltages. The data reveal a spatial variation, which is most pronounced near the position 3 – 3.5 nm, near the upper section of the step edge. Magnitude and sign of the variation of the asymmetry depend on bias voltage. These data provide already a clear evidence of strong spatial modulations of the spin-dependent electronic properties along the edge of a ferromagnetic nano structure. These spatial variations of the asymmetry of the differential conductance are ascribed to the spin-dependent Smoluchowski effect, as discussed in Section 7.6.

A spatial modulation of the spin polarization impacts also the tunnel magneto resistance ratio (TMR), as recently described by experiment and theory [97] and outlined in Chapter 2. In that work, the spatially modulated TMR ratio in the center region of a nanostructure was induced by spin-dependent quantum interference. Here, it is expected that strong spatial variations of the spin polarization at the edge of the Co nano structure may also strongly modulate the TMR ratio [86, 152]. The TMR ratio along the red line of Fig. 6.4 was extracted and Fig. 6.6 shows the TMR ratio at -0.3 V. As expected, the plot reveals a drastic variation of the TMR ratio from -10% to $+10\%$ within 1 nm along the Co step edge. Thus, this experiment indicates a pronounced spatial variation of the TMR ratio near steps of Co nano islands due to strong spatial modulation of the spin polarization in the same region.

A thorough discussion of the presented results [61] based on *ab initio* calcu-

lations is presented in Section 7.6.

6.2 Nanomagnetism of Co and Fe islands: magnetization reversal

An outstanding challenge in nanomagnetism is the quantitative understanding of magnetization reversal of nanostructures [62, 64, 65, 72, 77], which has also profound implications for magnetic recording media [63, 71]. Both fundamental research and applications are interested in the understanding of the crossover between different reversal modes. This opens the way to modify the parameters which govern the process and to tune this transition as wished. A key parameter in this respect is the magnetic anisotropy energy density K . A large anisotropy favors stable magnetization directions against thermal agitation.

However, the magnetic anisotropy changes dramatically when the dimensions of a particle are reduced to the nm scale in one or more dimensions. Lattice strain, its relaxation and the increasing relative number of surface and interface atoms induce a dramatic deviation of the magnetic anisotropy from its bulk values [23, 153–156]. Also, structural [115, 157] and electronic relaxations at the boundary of a nano structures [106] lead to distinct deviations of the atomic positions and the electronic structure on the nm scale. It is a priori not clear how the magnetic properties respond to this. This section provides experimental reference data for these issues.

6.2.1 Island size dependence of the magnetic switching field of individual Co nano islands

In this section I present briefly our recently published measurements about the island size dependence of the magnetic switching field of individual Co nano islands [77, 78] and I will compare them to Fe-decorated Co islands in the next section.

Figure 6.7 shows a constant-current STM image of several typical Co islands on Cu(111), which were studied in ref [77]. A quantitative analysis of the STM images provides the area A of these islands. Considering a pseudomorphic growth of Co on Cu, the number of Co atoms in a island can be calculated

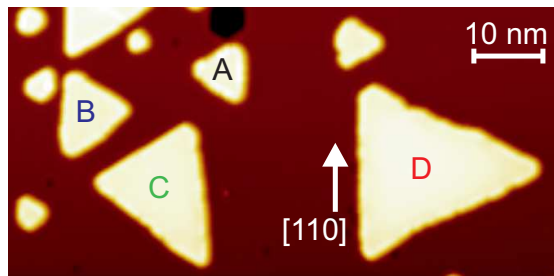


Figure 6.7: Constant current STM image of double layer high (0.4 nm) Co islands on Cu(111) ($V_{gap} = -0.27$ V, $I_t = 1$ nA, $T = 8$ K). Adopted from ref [77].

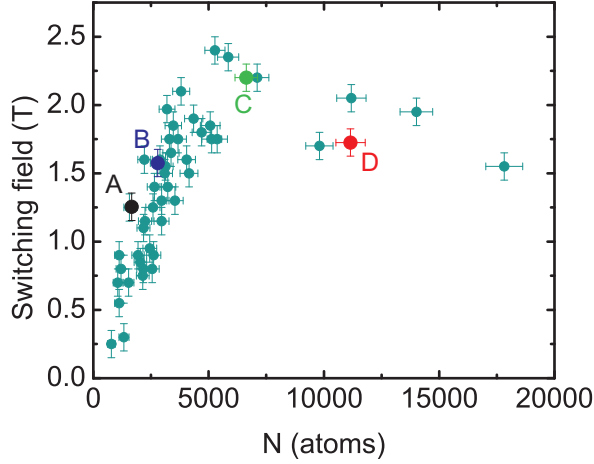


Figure 6.8: Switching fields of 54 individual Co islands of different size. Data points of islands A to D from fig. 6.7 are indicated [77].

as $N = A/0.028$, where A is in nm^2 . Figure 6.7 shows that the shape of the selected islands A to D is similar, while the size varies from 1600 to 13100 atoms. The different orientations of islands A and C versus B and D with respect to the underlying substrate correspond to the faulted and unfaulted layer stacking, respectively [100].

In order to access the magnetization state of the islands, the field dependence of the differential conductance dI/dV was measured at the centre of the Co islands. For one specific field value, several spectra of the differential conductance were obtained in 100 seconds, which marks the characteristic measurement time. The switching fields H_{sw} of 54 individual Co islands were extracted from the measurements of the field dependence of the differential conductance dI/dV as already shown in Section 3.4, 5.1 and 5.2. Figure 6.8 summarizes the measurements of the switching field H_{sw} for different island sizes N . A nonmonotonic dependence of H_{sw} on N is apparent. H_{sw} increases from 0.25 to 2.5 T for an increasing size N from $N = 700$ to 6000 atoms, and it decreases for larger islands. This observation already suggests a crossover between two different reversal mechanisms [77], as discussed extensively in Section 7.7.1.

6.2.2 Island size dependence of the magnetic switching field of individual Fe-decorated Co nano islands

The analysis and discussion of electron confinement and switching fields of Co islands on Cu(111) presented in Section 4.2 and 7.2 suggest that the rim of the Co islands shows peculiar electronic and magnetic properties, which deviate from those of the center region. Therefore, the extremely interesting question arises: what happens upon changing the environment of the rim atoms by decorating the Co islands with another material? In this case, Fe was chosen. A flavor of how the Fe decoration affects the electronic properties of the rim was already shown in Section 4.3, where the electron confinement in the Co core of a Fe-decorated Co island was presented. Here, the impact of the Fe decoration

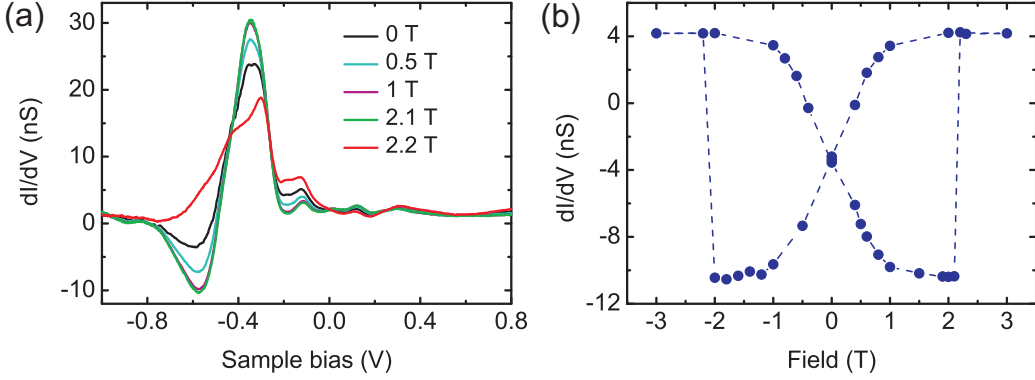


Figure 6.9: (a) dI/dV (V) spectra measured at the center of the Fe-decorated Co island in Fig. 6.11 at different magnetic fields. (b) Hysteresis loop of the differential conductance measured on the Fe-decorated Co island in Fig. 6.11 ($V_{gap} = -0.58$ V). $T = 10$ K, W tip covered with 40 atomic layers of Fe.

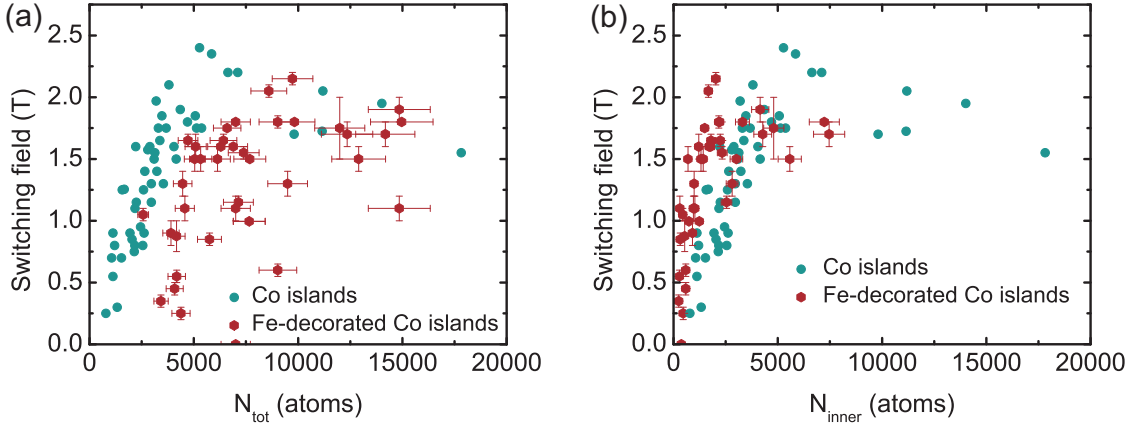


Figure 6.10: Switching fields of 54 individual Co islands and 41 Fe-decorated Co islands of different size. In (a) the switching field is plotted as a function of the total number of atoms N_{tot} , i.e. number of Fe and Co atoms. In (b) only the number of atoms N_{inner} in the inner Co core is considered. All measurements were performed at 10 K

on the switching field H_{sw} is investigated.

The sample was prepared as described in Section 3.3.1 and constant-current STM images of Fe-decorated Co islands are shown in the same section. It is not clear a priori whether the magnetization state of Fe-decorated Co islands is the same as that of pure Co islands. In order to clarify this point, differential conductance spectra at the center of the Co core of the Fe-decorated Co island of Fig. 3.3(c) were measured upon variation of the magnetic field along the out-of-plane direction (Fig. 6.9(a)). Several dI/dV spectra were obtained for each magnetic field value. Extracting the field dependence of the averaged differential conductance signal at -0.58 V, the butterfly hysteresis loop of the

differential conductance in Fig. 6.9(b) was obtained. The hysteresis loops of the differential conductance measured at the center of the Co cores of each studied Fe-decorated Co island present the same butterfly shape. The loops show the same characteristic features observed in the hysteresis loops of the differential conductance measured on the pure Co islands. They show a smooth change of the differential conductance signal due to an increase of the z-component of the tip magnetic moment and a abrupt change ascribed to the switching of the island magnetization. We can conclude that the Co cores of the Fe-decorated Co islands still show an uniaxial anisotropy with easy axis oriented out-of-plane.

The switching fields H_{sw} of 41 Fe-decorated Co islands as a function of the total number of atoms (Co+Fe) in the island are summarized in Fig. 6.10(a). The switching field of Co islands is also plotted as a reference. Surprisingly, the collection of switching fields of Fe-decorated Co islands in Fig. 6.10(a) does not show a clear tendency, and the scatter of points looks random. In Fig. 6.10(b), the same switching fields values H_{sw} are plotted as a function of the size of Co core. Here, a much clearer trend can be observed. The switching fields increase monotonically up to a size of the Co core of around 2000 atoms. For larger Co core size it is not clear whether a saturation is reached or they slowly decrease with the Co core size. The scatter of the points is significant and they are more dispersed respect to the switching fields of pure Co islands. These results are discussed in more depth in Section 7.7.2. Already here we can state that Fe-decoration impacts the switching fields of Co islands. It appears to induce larger switching fields in the size range of up to 2000 atoms of the Co core.

6.3 Spin dependent electronic properties of Fe islands and Fe-decorated Co islands

The surprising results presented in the previous section suggest that the Fe decoration contributes in a non-trivial way to the switching field of Fe-decorated Co islands. This observation calls for a deeper investigation and understanding of the magnetic properties of the Fe decorating the Co islands. Spin-polarized STM is a very suitable technique for such a study as it can measure spatial variations of the spin polarization above nano structures with high spatial resolution.

As already shown in Section 3.3.1, both pure Fe and Fe-decorated Co islands can be found on the Cu(111) surface. A clear cut distinction between Fe and Co regions is possible by their different spectroscopic signatures in the differential conductance spectra. Figure 6.11 shows measurements of the differential conductance performed on two-atomic-layer-high pure Fe and Fe-decorated Co islands. The dI/dV spectra taken on pure Fe islands shows a clear peak at around -0.23 V. In Fe-decorated Co islands, the Co core can be easily identified by the pronounced peak at around -0.3 V [111], visible in dI/dV spectra taken in inner part of the islands (green curve in fig. 6.11(b)). Also, the clear interference pattern due to the electronic quantum interference of the Co surface states studied in Section 4.2 is visible in the maps of the differential conductance in the inner part of the islands (upper inset of Fig. 6.11(b)). No corresponding modulation is observed in pure Fe islands on Cu(111). The Fe decoration of the Co core shows two different areas with different apparent heights, which varies

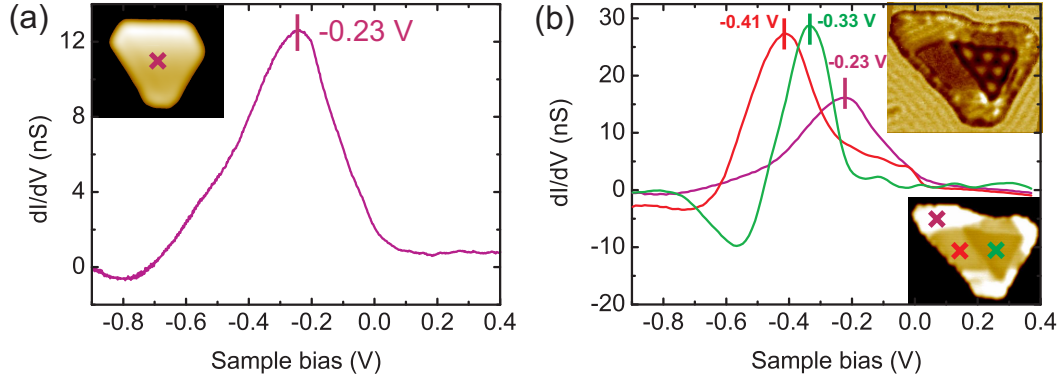


Figure 6.11: (a) $dI/dV(V)$ spectra measured at the center of the island shown in the inset. (b) $dI/dV(V)$ spectra measured at the marked positions of the Fe-decorated Co island shown in the lower inset. Three clearly different dI/dV spectra are measured. The upper inset shows the map of the differential conductance of the island in the lower inset. A clear modulation pattern due to quantum interference of the Co surface states can be seen in the inner part of the island. Stabilization parameters: $V_{gap} = +0.5$ V, $I_t = 1$ nA. Measurement parameters: $V_{gap} = +0.1$ V, $I_t = 1$ nA, $T = 10$ K, W tip covered with 40 atomic layers of Fe. The islands in (a) and (b) are further characterized in Fig. 6.13 and Fig. 6.14.

with the sample bias, as shown in the lower inset of Fig. 6.11(b). Spectra of the differential conductance taken on these two different Fe regions are different. One Fe region presents the same dI/dV spectra which characterizes the pure Fe islands (purple curve in Fig. 6.11(b)). The dI/dV spectra of the second Fe region shows an intense peak at -0.41 V and a small bump of low intensity at -0.05 V (red curve in Fig. 6.11) instead.

Pure Fe nano islands on Cu(111) were already studied by Biedermann et al. [158] and Gerhard et al. [159]. In their studies they also find two Fe regions with different apparent heights. Based on atomically resolved STM images, the authors identify two different Fe regions with two different stackings of Fe on Cu(111), which they refer to as either fcc or bcc. Here we follow their convention of calling different Fe regions fcc or bcc, although the assignment of a bcc structure in a two layer film appears to be disputable. Further below we prefer to refer to Fe phase-a (fcc) and Fe phase-b (bcc). Figure 6.12 shows a hardsphere model explaining the differences between the two stackings. The so-called bcc stacking is obtained by shifting the Fe atoms of the second layer from hollow sites to bridge positions. In ref. [159] the authors perform also STS measurements on the two Fe regions. The dI/dV spectra on Fe fcc shows a pronounce peak at -0.4 V and a small one at small negative voltages near the Fermi level. Instead, bcc Fe areas show a peak at -0.25 V. The dI/dV spectra measured on the different Fe regions of our sample shown in Fig. 6.11 present the same features at the same sample bias values as reported by Gerhard et al. [159]. Therefore we can identify the pure Fe islands of our sample as formed by the so-called bcc stacking of Fe on Cu(111). On the other hand, the Fe which decorates the Co islands is formed both by fcc and bcc stacking regions, which

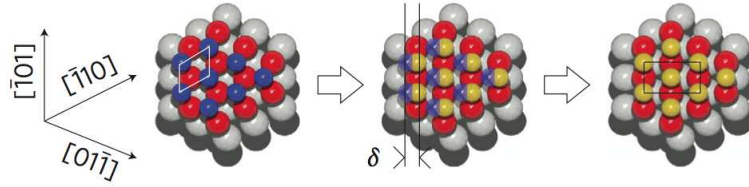


Figure 6.12: Hardsphere model illustrating the movement of the top Fe atoms from their threefold hollow site position of fcc (111) stacking (blue) to the so-called bcc (110) bridge position (orange) [159]. Grey and red balls represent Cu and bottom Fe atoms, respectively. Lattice directions in the fcc (111) plane and respective unit cells are indicated. Adopted from ref. [159].

are easily distinguishable by STS. An inspection of the lower inset of Fig. 6.11(b) reveals that the region of Fe decoration with lower apparent height shows the characteristic dI/dV spectra of Fe fcc stacking and the region with higher apparent height that of Fe bcc stacking on Cu. However, in this thesis no atomically resolved STM image was achieved on Fe regions and the distinction between different Fe stacking is based exclusively on spectroscopy measurements. Since no evidence of different stacking of Fe on the Cu substrate is shown here, the Fe fcc-stacking areas (bcc-stacking areas) will be called Fe phase-a (Fe phase-b) throughout the thesis, whenever I will refer to our measurements.

In ref. [159] the authors perform also *ab-initio* calculations which predict a ferromagnetic order for Fe bcc stacking and a layer-wise antiferromagnetic order for Fe fcc stacking on Cu(111). However, no experimental evidence for the predicted magnetic properties of Fe on Cu have been presented so far and corresponding measurements are presented here.

All the measurements presented in this section were taken with Fe-covered W tips. The response of the tip magnetic moment to the applied magnetic field was characterized as shown in Sections 5.2 and 6.2.2. These tips showed a gradual increase of the z-component of the magnetic moment with increasing field, as shown in Fig. 5.4 and Fig. 6.9.

For sake of clarity, let us focus on pure Fe islands first. Figure 6.13(a) shows the constant-current STM image of a pure Fe island and Fig. 6.13(b-f) are maps of the differential conductance of the same island taken at different magnetic field values. A spectra of the differential conductance taken at zero field at the center of the island is shown in Fig. 6.11. At 0 T the differential conductance signal does not show any pronounced spatial modulation within the Fe island (Fig. 6.13(d)). Surprisingly, as soon as the magnetic field is applied, a stripe-like modulation of the dI/dV signal, which is not visible at 0 T, appears in the maps of the differential conductance of Fig. 6.13(b,c,e,f). Figure 6.13(g) shows differential conductance dI/dV line profiles along the white line in Fig. 6.13(b-f). Important insights can be extracted from this graph. First of all, the differential conductance signal for measurements taken in-field oscillates around the green line profile measured at 0 T. Secondly, the amplitude of the oscillations of the differential conductance signal increases with increasing magnetic field and saturates at ± 1.5 T. It is important to mention at this point that the measurements in Fig. 6.13 were performed with the same tip apex used to obtain the hysteresis loop of the differential conductance of Fig. 6.9(b). Also there, the

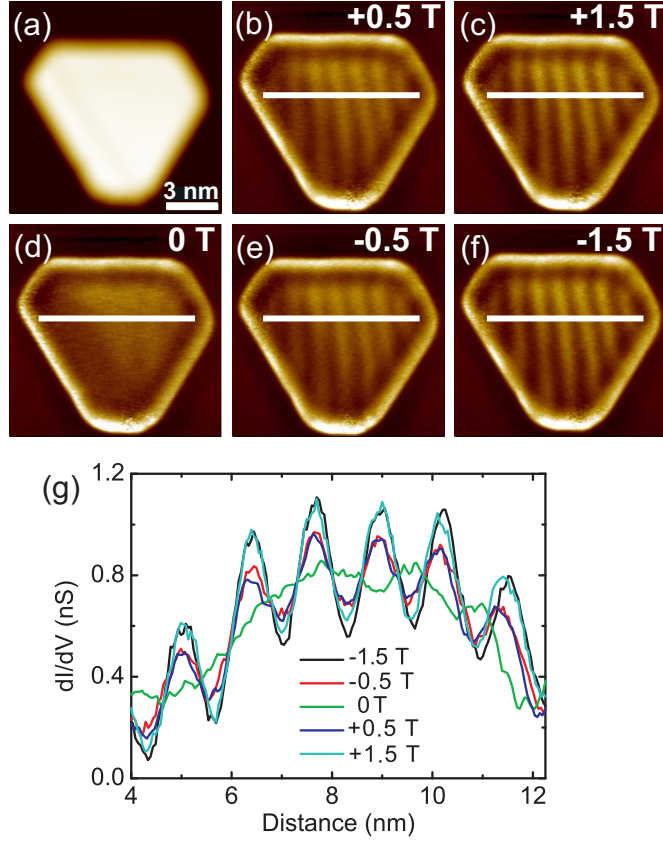


Figure 6.13: (a) Constant current STM image of a pure Fe-b island. Imaging parameters: $V_{gap} = +0.1$ V, $I_t = 1$ nA. (b-f) dI/dV maps of (a) at different magnetic field values. The white line indicates the line along which the dI/dV lines profiles in (g) were taken. Measurement parameters: $V_{gap} = -0.5$ V, $V_{stab} = +0.5$ V, $I_{stab} = 1$ nA, $T = 10$ K, W tip covered with 40 atomic layers of Fe. (g) dI/dV line profiles measured along the white line in (b-f).

saturation of the differential conductance signal is achieved at ± 1.5 T. We ascribe this saturation to the tip apex, where the z-component of the tip magnetic moment reaches its magnetic saturation at the field value of ± 1.5 T. Finally, the oscillations are always in phase and no shift or inversion of the differential conductance dI/dV contrast can be observed upon changing the polarity of the applied magnetic field. As can be seen in Fig. 6.13(g), the line profiles measured at -1.5 T and $+1.5$ T overlap as well as those measured at -0.5 T and $+0.5$ T do. Many pure Fe islands with different size were investigated, and a periodicity of 1.28 ± 0.06 nm of the stripe pattern was always observed, irrespective of the size of the island.

Next, we investigated whether the stripe-like pattern observed on the Fe phase-b in pure Fe islands is influenced by the Co core when the Fe phase-b decorates a Co island. Figure 6.14 shows maps of the differential conductance of the Fe-decorated Co island of Fig. 6.11(b) at different magnetic field values.

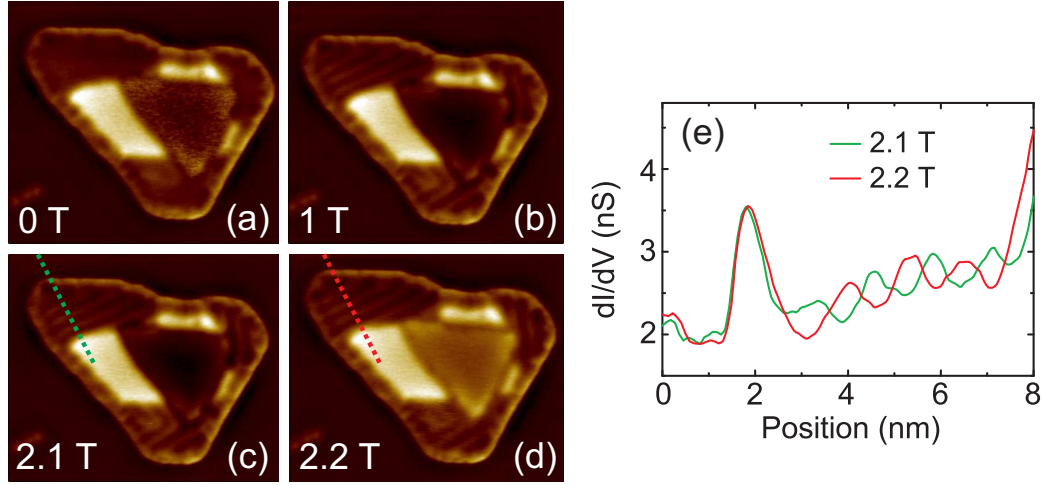


Figure 6.14: (a-d) Maps of the differential conductance dI/dV of the Fe-decorated Co island of fig. 6.11 at different magnetic field values. (e) Differential conductance dI/dV line profiles along the green and red dashed lines in (c) and (d), before and after the switching of the Co core magnetization direction respectively. It is clear that the differential conductance signal, measured on the stripe pattern located on the Fe-b region, inverts its contrast after the switching of the magnetization of the Co core. Measurement parameters: $V_{gap} = -0.5$ V, $I_t = 1$ nA, $V_{stab} = +0.5$ V, $I_{stab} = 1$ nA, $T = 10$ K, W tip covered with 40 atomic layers of Fe.

Fe phase-b regions are found at the corners of the island, and Fe phase-a are observed along the side of the Fe decoration, as identified by the dI/dV spectra in Fig. 6.11(b). A large region of Fe phase-b can be seen at the upper-left corner of the island. No stripe-like modulation of the differential conductance signal on the Fe phase-b is observed in the maps of the differential conductance at 0 T (Fig. 6.14(a)). Upon application of the magnetic field, a clear stripe-like pattern appears on the Fe phase-b located at the corner of the island (Fig. 6.14(b,c)), as observed for pure Fe islands. A further increase of the magnetic field induces the magnetization reversal of the Co core, as indicated by the change in the brightness of the Co core from Fig. 6.14(c) to Fig. 6.14(d). Figure 6.14(e) shows the differential conductance dI/dV line profiles along the green and red lines drawn in Fig. 6.14(c) and (d). The direction of the line profiles are perpendicular to the stripe pattern on Fe phase-b. It is oriented from the edge of the island, across the Fe phase-b region, towards the Fe phase-a region. The change of the modulation shows that the dI/dV signal on the Fe phase-b inverts its contrast after the switching of the Co island magnetization. This indicates a strong coupling between the two regions, as discussed in Section 7.8.1.

Figure 6.15(c,d) shows maps of the differential conductance dI/dV of two Fe-decorated Co islands and one pure Fe island for a magnetic field of +1 T. The corresponding constant-current STM images are shown in Fig. 6.15(a,b). As already discussed, spatial periodic modulations of the dI/dV signal can be observed both on Fe phase-b at the decoration of the Co islands and on Fe

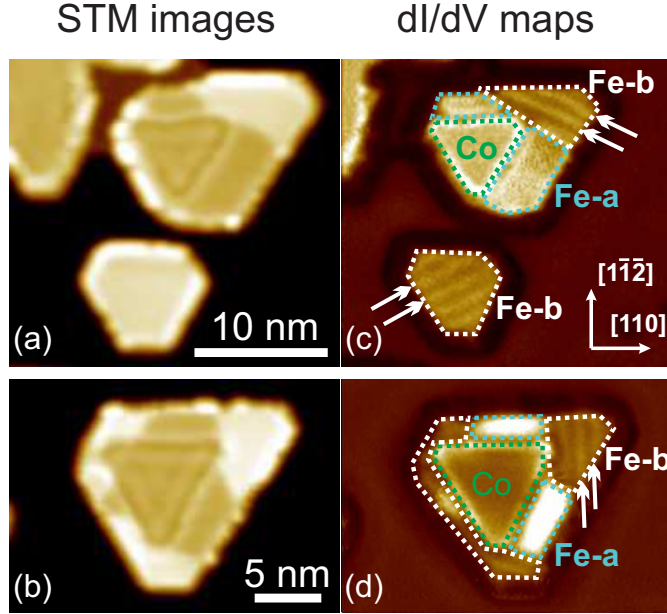


Figure 6.15: (a), (b) Constant current STM images of pure Fe and Fe-decorated Co islands. Imaging parameters: $V_{gap} = +0.2$ V, $I_t = 1$ nA. (c) and (d) Maps of the differential conductance dI/dV of the same islands in (a) and (b). The white arrows indicate the directions of the stripes in the Fe-b regions. The different areas are evidenced, i.e. the dashed white, light blue and green lines surround the Fe-b, Fe-a and the Co regions, respectively. Measurement parameters: $V_{gap} = -0.4$ V, $I_t = 1$ nA, $V_{stab} = +0.5$ V, $I_{stab} = 1$ nA, $B = 1$ T, $T = 10$ K, W tip covered with 40 atomic layers of Fe.

phase-b which forms the pure Fe islands. Figure 6.15(c,d) show that three directions of the stripe-like pattern are observed, as indicated by the white arrows. The stripes run along the $[1\bar{1}\bar{2}]$, $[21\bar{1}]$ and $[121]$ crystallographic directions of the Cu(111) surface, as established from atomic resolution STM images of the Cu(111) substrate. Also, they are perpendicular to the edges of the islands, which are orientated along the $[10\bar{1}]$, $[110]$ and $[011]$ crystallographic directions of the Cu(111).

Up to this point, the dependence of the differential conductance dI/dV signal on the the magnetic field has been discussed only for the Fe phase-b. As it was already shown above, the Fe decoration presents regions of the so-called Fe phase-a, located along the side of the islands. In-field measurements of the differential conductance were performed also on Fe phase-a regions, but no field-dependent feature of the dI/dV signal was found. Figure 6.16(a) shows a constant current STM image of a Fe-decorated Co island. A spatial modulation in the inner part of the island marks off the Co core. Fe phase-a areas are located at the side of the the Fe decoration as identified by STS. Figure 6.16(b) shows two dI/dV spectra taken at the positions marked in red and blue in Fig. 6.16(a). The signatures of the Fe phase-a at -0.4 V and of the Co at -0.3 V are clearly visible. Several dI/dV spectra were measured at the position marked in blue

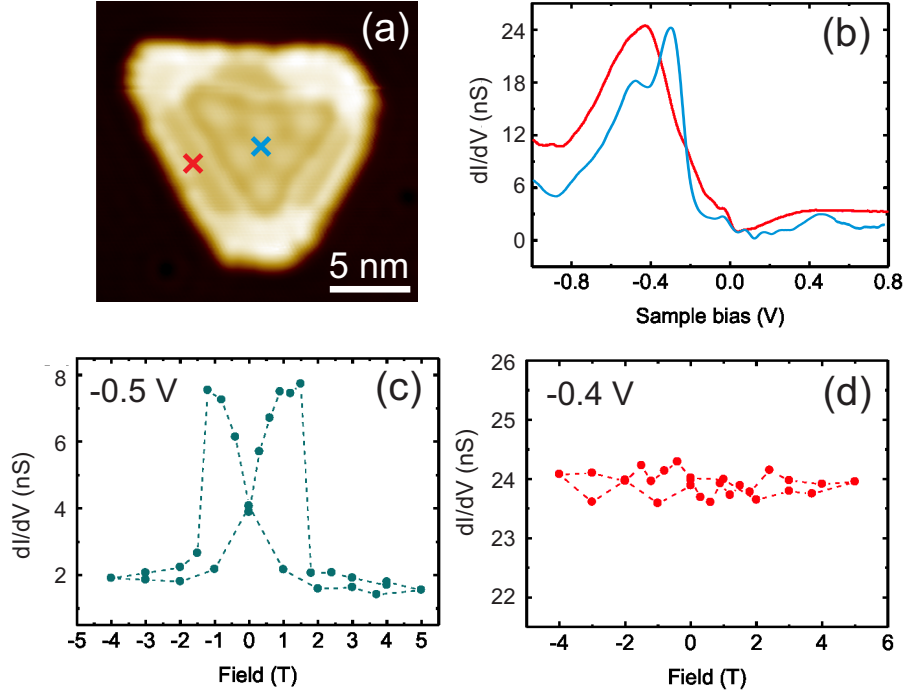


Figure 6.16: (a) Constant current STM image of a Fe-decorated Co island. The red and blue marks indicate the points where the dI/dV spectra in (b) and the hysteresis loops of the differential conductance in (c) and (d) were measured. (b) Spectra of the differential conductance dI/dV measured at zero field at the marked red position in (a). The characteristic peak of the Fe phase-a at -0.4 V is clearly visible. (c), (d) Hysteresis loops of the differential conductance measured on the Co core (c) and on Fe phase-a region (d). A drop in the dI/dV signal, due to the switching of the Co core magnetization, can be clearly observed in the measurement performed on the Co core. On the other hand, no clear dependence of the differential conductance dI/dV on the magnetic field can be observed in the hysteresis loop of the differential conductance measured on the Fe phase-a region. Measurement parameters: $V_{gap} = -0.1$ V, $I_t = 1$ nA, $V_{stab} = +0.5$ V, $I_{stab} = 1$ nA, $T = 10$ K, W tip covered with 40 atomic layers of Fe.

(Co) and red (Fe) in Fig. 6.16(a) and the field dependence of the dI/dV signal at -0.5 V (for Co) and -0.4 V (for Fe) is shown in Fig. 6.16(c,d). A clear drop in the differential conductance signal due to the switching of the Co core magnetization can be observed in Fig. 6.16(c), whereas no clear dependence of the dI/dV signal on the magnetic field is evident for Fe phase-a in Fig. 6.16(d). No dependence of the dI/dV signal on the magnetic field was found for any sample bias between ± 1 V. This result reveals that the relative magnetization orientation between tip and Fe-a remains constant through a field cycle, and its implication for the magnetic order of Fe-a is discussed in Section 7.8.2.

In conclusion, both pure Fe islands and Fe-decorated Co islands on Cu(111) show striking and unexpected characteristics. The Fe phase-b presents a stripe-

like pattern in the maps of the differential conductance measured in-field and Fe phase-a does not show any dependence of the differential conductance dI/dV signal on the magnetic field. The surprising results presented in this section are discussed in Section 7.8. In the same Section, also asymmetry maps of the differential conductance for Fe-decorated Co islands are presented and compared to previous measurements on pure Co islands.

Chapter 7

Discussion

A detailed discussion and analysis of all experimental data presented above is given in this chapter. The different topics are ordered according to their sequence in the Chapters 4, 5 and 6.

Firstly, the electron confinement within graphene nano islands is discussed. Our results are the first demonstration that the wave vector quantization in graphene nano islands follows the very simple 1D "particle-in-a-box" model. Interestingly, electron properties of graphene nano islands show remarkable differences in comparison with those of an extended graphene layer on Ir(111). Section 7.2 discusses and compares the results of electron confinement within Co islands and Fe-decorated Co islands. The characteristic confinement length in Co islands is found to be between 2.5 and 3 nm shorter than the geometrical height of the island. On the other hand, the confinement length corresponds exactly to the geometrical height of the Co core in Fe-decorated Co islands. This new result is ascribed to the disappearance of the rim state at the edge of the Co core in Fe-decorated Co islands. Sections 7.3 and 7.4 discuss the spin polarization of Cr bulk tips and the temperature dependence of the magnetic response of Fe-coated W tips. The spin polarization of bulk Cr tips is extracted and a superparamagnetic response to the applied magnetic field is established for the Fe-coated W tips used in this thesis. *Ab-initio* calculations are discussed in Sections 7.5 and 7.6 to estimate the spin polarization of Cu surface states near a Co island and to discuss the spin-dependent Smulochowski effect. Section 7.7 discusses the results on the magnetic switching field of individual Co islands and Fe-decorated Co islands on Cu(111). A crossover of the magnetization reversal from an exchange-spring behavior to domain wall formation with increasing size is found for pure Co islands. A model treating the Co islands formed by a magnetically soft Co rim coupled via exchange interaction to a magnetically hard Co core explains the results. Surprisingly, the Fe decoration removes the magnetically soft Co rim and contributes in a non-trivial way to the switching fields of the nano islands. Finally, Section 7.8 discusses the results obtained for Fe on Cu(111). A novel and unexpected magnetic structure is found both on pure Fe islands and on the Fe rim of Fe-decorated Co islands.

7.1 Electron confinement in graphene nano islands

Figure 4.3 shows a series of maps of the differential conductance dI/dV taken on graphene nano islands on Ir(111) which exhibit pronounced modulation patterns that change with energy. This observation is ascribed to the formation of standing waves in the local density of states (LDOS) due to electron confinement [54]. This phenomenon arises from the scattering of electrons at potential barriers, such as the edges of the graphene nano islands. The interference of incoming and outgoing waves leads to the formation of standing wave patterns. To compare the observed dI/dV maps to the LDOS of confined electrons, the multiple-scattering method [50, 160–162] was used to simulate the formation of standing waves in the same confinement geometries as that of the islands shown in fig 7.1(f-j,p-t). In the multiple-scattering method, the electron probability density at a position is determined as the interference between incoming wave and scattered wave from point scatterers. The confinement areas were set by arranging the atomic-size point scatterers at the same boundaries as the geometrical ones in the STM images (Fig. 4.1(B,C)). The resultant probability density at a position within the boundary is given by the superposition of the

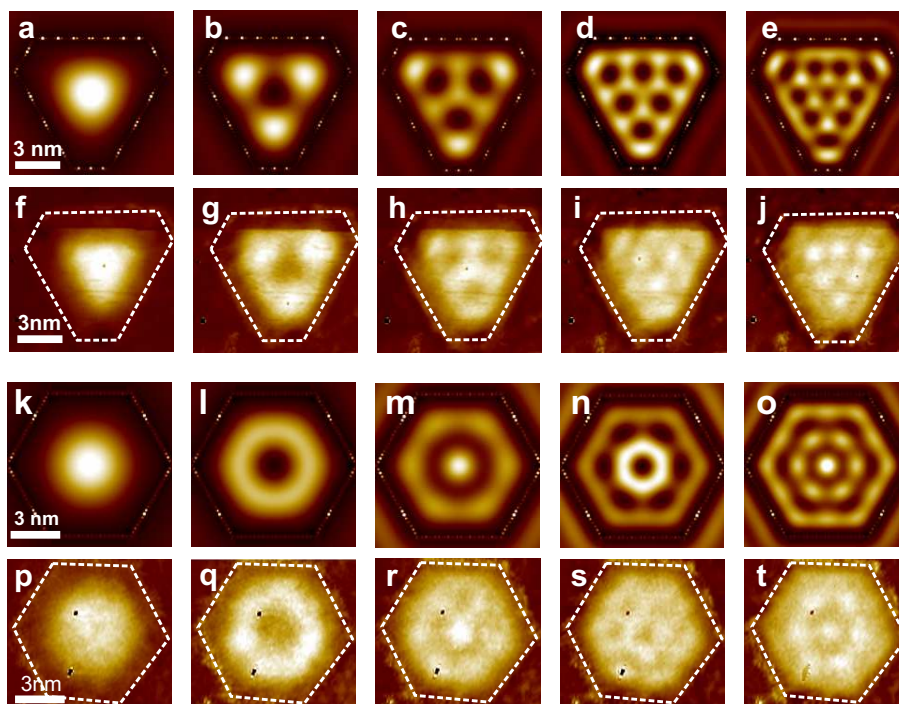


Figure 7.1: (a-j) Calculated spatial modulation of the electron density (a-e) for the island boundary in Fig. 4.1(B) and maps of the differential conductance dI/dV obtained for the same island (f-j). (k-t) Calculated spatial modulation of the electron density (k-o) for the island boundary in Fig. 4.1(C) and maps of the differential conductance dI/dV obtained for the same island [54].

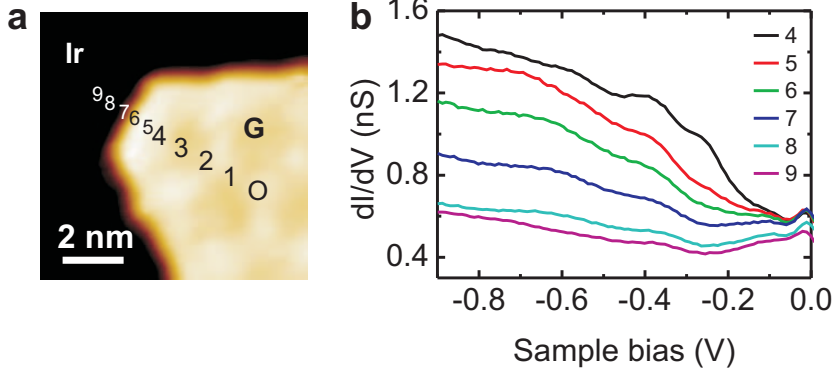


Figure 7.2: (a) The upper-left region of the island in Fig. 4.1(B). (b) Spectra of the differential conductance dI/dV at the positions denoted by 4 – 9 in (a). The positions for the spectra in fig. 4.2(B) are denoted by O-4. Measurement parameters: $V_{stab} = +0.5$ V, $I_{stab} = 1$ nA, $V_{mod} = 20$ mV. Adopted from ref. [54]

original wave with the scattered waves from all the point scatterers. The input parameter for the calculation is the wave number k of the original wave. The calculation gives spatially resolved LDOS patterns. Figure 7.1(a-e,k-o) presents the LDOS patterns of the five lowest confinement modes for the structures corresponding to Fig. 4.1(B,C). The calculation reproduces very similar patterns as compared to the dI/dV modulation patterns in Fig. 7.1(f-j,p-t).

In the results Section 4.1 the energy dependence of the wave-vector within the graphene nano islands is extracted from the maps of the differential conductance by a FT analysis. The resulting dispersion relation is presented in Fig. 4.4. The data points follow a linear shape, although they exhibits a distinct quantization in k . The linear dispersion relation $E = E_D - \hbar v_F k$ is expected from the electronic dispersion relation predicted by the tight binding model of graphene [109, 110]. Therefore, a linear fit with the mentioned linear equation is performed. The fit leads to $E_D = -0.088 \pm 0.022$ eV (-0.086 ± 0.021 eV) and $v_F = (6.3 \pm 0.40) \times 10^5$ m/s ($(6.0 \pm 0.38) \times 10^5$ m/s) for the island in Fig. 4.1(B) (Fig. 4.1(C)).

The offset E_D of -0.1 eV with respect to the Fermi energy (E_F) is similar to the results obtained on infinitely large graphene/Ir(111) systems [163–165]. However, it is surprising that v_F values extracted from the plots in Fig. 4.4 are smaller by 30 – 40% than the Fermi velocity calculated for free-standing graphene (v_{F0}) [109, 110]. The graphene-substrate interaction is known to affect the graphene band structure. Angle-resolved photoemission spectroscopy (ARPES) was employed to measure the band structure of graphene/Ir(111). Those experiments reveal the creations of mini gaps in the graphene π -band due to the moiré interaction and the hybridization of Ir surface states [166] with the graphene π -band at E_F . Nevertheless, the measured band structures showed the

preservation of a linear dispersion relation with the deviation of v_F from v_{F0} by only a few percent. Therefore, the graphene-substrate interaction itself appears not to be the only origin to explain the large reduction of v_F in this experiment. Another mechanism for the reduction of v_F could stem from the nanometer-size of the graphene islands in this study. In a tight binding model, v_F is described by $\hbar v_F = 3ta/2$ [109,110], where a is the nearest carbon-carbon atomic distance and t is the nearest-neighbor hopping amplitude through the π orbitals of carbon atoms. This expression with v_F extracted from this study gives a hopping amplitude $t \simeq 1.7$ eV $\simeq 0.6t_0$, where $t_0 = 2.8$ eV is the carbon-carbon hopping amplitude of free-standing graphene. It was predicted that the modification in the hopping amplitude between carbon and impurity sites can locally reduce v_F due to the π orbital suppression at the defect sites [167]. Recent STM and STS measurements near the defects in graphene corroborated this view and reported a considerable reduction of v_F down to $\simeq 0.3v_{F0}$ [168,169]. Furthermore, these studies showed that the reduction of v_F extends over several nanometers around the defect sites. The edge atoms of graphene grown on Ir(111) are known to have a much stronger interaction with the substrate than those in the central region of the island [170–172]. The sharp decrease of the differential conductance signal near the island edge supports this view. Figure 7.2 shows the dI/dV spectra measured on different positions along the transition from graphene towards Ir across the upper-left edge of the graphene island shown in Fig. 4.1(B). As the measurement position moves from graphene to Ir, the dI/dV signal decreases in magnitude and approaches the values measured on Ir. A monotonic variation of the dI/dV signal was observed within the distance of $\simeq 1$ nm from the edges, where peculiar edge-related states, which were discussed for other systems [173], or described in theory [55], were not observed here. This strongly suggests the suppression of the π -band in the near-edge regions. The edges of the islands, therefore, could be viewed as extended lattice defects. Since the islands in this study have radii of 4 – 5 nm, one could expect a reduction of v_F over the whole area of the islands. The noticeable difference between our work and the previous ARPES studies is the size of graphene. Thus, besides the graphene-substrate interaction, the small island sizes with the suppressed π -band near the edges provides one plausible scenario as a mechanism to induce the considerably small v_F in the nanometer-size graphene islands.

An additional explanation of the observed electron confinement comes from very recent works of Subramaniam et al. [174] and Altenburg et al. [175]. They claim that the modulation pattern observed in maps of the differential conductance on graphene nano islands on Ir(111) comes from the intrusion of the Ir surface resonance located at the Γ point into the graphene layer. Altenburg et al. propose that nanometer-seized graphene islands act as local gates, which shift and confine the Ir surface resonance. Their analysis of the electron confinement indicates the presence of a two-dimensional electron gas described by a parabolic equation with a binding energy of -160 meV and an effective electron mass of $0.18 m_e$ underneath single-layer graphene on the Ir(111) surface. So far, electron confinement in graphene nano islands has been observed only on the Ir(111) substrate and this might be a convincing explanation for the lack of experimental observations on other substrates. Although the data presented in fig. 4.4 are described better by a linear fit, parabolic fits of our data with the two-dimensional-electron-gas equation $E = E_0 + \hbar^2 k^2 / 2m^*$ were performed following the suggestion of Altenburg et al. [175]. The quality of the fit is quite

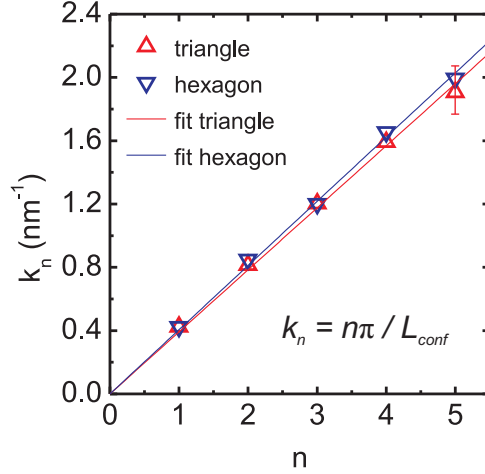


Figure 7.3: $k_n(n)$ plots extracted by applying 1D particle-in-a-box model to the wave vectors obtained from the FT maps in Fig. 4.3. The slope of the fit gives the effective confinement length L_{conf} . The effective confinement length is 8.4 nm (8.0 nm) for the island in Fig. 4.1(B) (Fig. 4.1(C)). Adopted from ref. [54].

poor and yields $E_0 = -0.29 \pm 0.04$ ($E_0 = -0.30 \pm 0.04$) and $m^* = 0.22 \pm 0.02 m_e$ ($m^* = 0.25 \pm 0.02 m_e$) for the island in Fig. 4.1(B) (Fig. 4.1(C)). These values do not agree with the values measured in ref. [175]. Therefore, electron confinement in our system does not appear to arise from electron confinement of Ir surface state electrons, described by a two-dimensional electron gas. However, the observation of an Ir-related electron confinement cannot be excluded. Recent studies show that even the dispersion relation of the well known Shockley surface states of Cu(111) deviates significantly from the paradigmatic parabolic behavior of quasi-free electrons [176]. This is due to the hybridization between Cu surface states and bulk states. Similarly, the hybridization between Ir and graphene may lead to a specific dispersion relation and electron confinement which reflect properties of this specific interface.

The determination of the effective size of the confinement L_{conf} is an interesting aspect of the confinement phenomena in graphene nano islands, as it is in the surface state confinement of metallic system [41, 43–46]. An effective way to obtain the confinement size along the symmetry axis of a threefold symmetric 2D structure by using a one-dimensional (1D) particle-in-a-box model was introduced by Rodary et al. [46]. The same analogy was applied to the graphene islands in Fig. 4.3. The magnitude of the wave vector k_n was taken along one of the symmetric direction, where n is the integer index determined from the sequence of dI/dV patterns shown in Fig. 4.3(A-E) (Fig. 4.3(K-O)). Figure 7.3 shows the plots of k_n as a function of n . Each data set is fitted well by a linear function $k_n = n\pi/L_{conf}$ intersecting the origin. The slope of the $k_n(n)$ relation gives $L_{conf} = 8.4$ nm (8.0 nm) for the island in Fig. 4.1(B) (Fig. 4.1(C)), which is approximately 0.5 (0.7) nm smaller than the geometric size as indicated in Fig. 4.1(B) (Fig. 4.1(C)). The above-mentioned strong interaction of the edge carbon atom is expected to deplete the electronic DOS near the island edge. It

is plausible that such an effect extends to 2 – 3 unit cells (0.5 – 0.7 nm) from the island edge (see also the dI/dV spectra in Fig. 7.2). This may indicate that the sharp transition of the electronic properties near the island edge serves as the potential barrier for confinement, leading to a smaller L_{conf} as compared to the geometric size.

In conclusion, a pronounced spatial modulation of the differential conductance dI/dV in nano sized monolayer graphene island on Ir(111) was observed. These findings are ascribed to spatial modulations of the LDOS which is induced by electron confinement. The origin of the confined electrons is currently still under debate.

7.2 Electron confinement in Co nano islands and Fe-decorated Co nano islands

The results presented in Section 4.2 revealed, similar to the observations made for graphene nano islands, pronounced modulation patterns of the differential conductance within the Co islands. The energy dependence of these patterns is investigated, and the wave-vector is extracted from the spatial modulation of the differential conductance by a FT analysis. The confinement analysis is extended to smaller wave vectors ($k \leq 1 \text{ nm}^{-1}$) as compared to previous work [75], and the discrete wave vectors follow a parabolic dispersion relation (see Fig. 4.6). The parabolic fit with the equation $E = E_0 + \hbar^2 k^2 / 2m^*$ yields $E_0 = -0.17 \pm 0.02$ and $m^* = 0.35 \pm 0.02 m_e$. Previous studies reported values of $E_0 = -0.22$ [106], -0.16 [111] and -0.11 eV [75] for the onset of the Co surface states on Cu and an effective mass of $m^* = -0.38 m_e$ [111] and $m^* = -0.39 m_e$ [75]. The onset

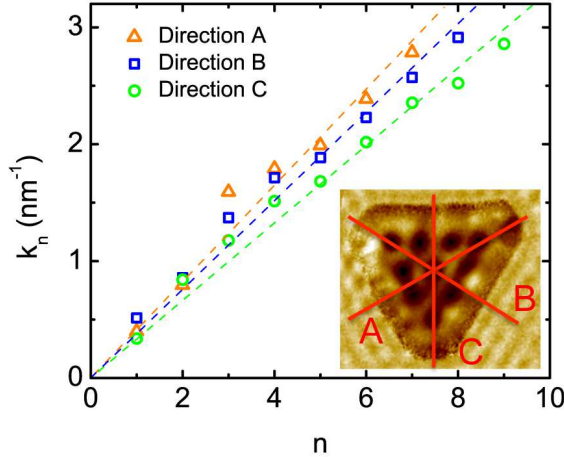


Figure 7.4: Plot of the wave vector as a function of an integer index extracted by applying 1D particle-in-a-box model to the wave vectors obtained from Fig. 4.6. The three data sets correspond to three directions of the triangle. The slope of the fit gives the effective size of the confinement length d_{eff} . We obtain $d_{eff} = 7.6 \pm 0.3, 8.3 \pm 0.4, 9.5 \pm 0.5$ nm for the directions A, B, C, respectively. These are indicated in Fig. 7.5.

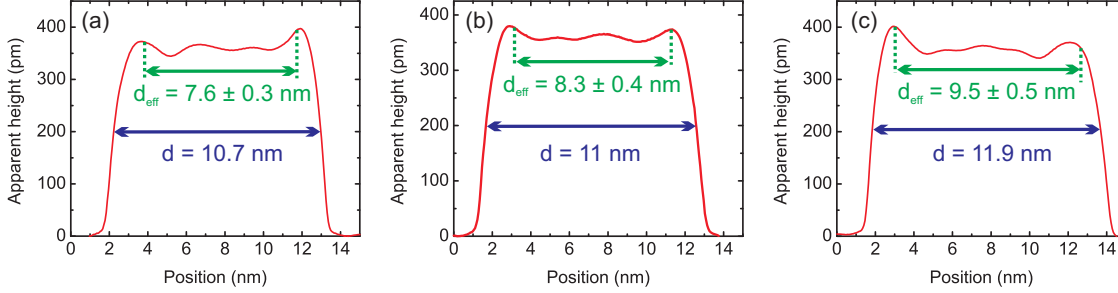


Figure 7.5: Comparison of the characteristic lengths extracted from the quantization rule of Fig. 7.4 with constant current STM data along the three different directions A, B and C of the Co island.

$E_0 = -0.17 \pm 0.02$ measured here is in line with the previous reports, but the effective mass $m^* = 0.35 \pm 0.02 m_e$ is slightly smaller. Considering the relative large variations of E_0 between the different reports, it is possible that the values E_0 and m^* may be island size dependent.

The one-dimensional particle-in-a-box model [46, 75] was used also here to analyze the confinement in the Co island. Figure 7.4 shows the plots of the wave vector k_n as a function of n for the three symmetry axes shown in the inset. Each data set is fitted by a linear function $k_n = n\pi/d_{eff}$ enforced through the origin, where the slope of the curves gives the effective confinement length d_{eff} for the three symmetric directions of the island in Fig. 4.5. A comparison of the three d_{eff} extracted for the different directions in Fig. 7.4 with STM topography data is shown in Fig. 7.5. Note, this island is not equilateral and the three heights differ from each other. Fig. 7.5 reveals a systematic deviation of the extracted characteristic lengths d_{eff} from the different geometric lengths d . The extracted d_{eff} are between 2.4 and 3.1 nm smaller than the topographical values from constant-current STM images. A possible explanation is that the electronic structure of the island is changed close to the rim [106]. Such a change alters the position of the potential barrier responsible for the scattering towards the island center and leads to a reduced characteristic length. It was shown in ref. [75, 115] that the electronic structure is indeed changing significantly as a function of position on the island towards the rim. This phenomenon can be explained by structural relaxation of the atoms at the rim of the island [115]. Furthermore an electronic state is observed at the rim of the islands near the Fermi energy [106, 115]. This also alters the electronic structure, and we speculate that this also affects the scattering potential barrier at the rim of the islands. Since the spatial distribution of that rim-state has a width of about 1.2 – 1.5 nm [75], it seems likely that the differences between geometric lengths and confinement lengths are mainly caused by the rim-state in combination with structural relaxation effects.

In order to check the validity of these assumptions, the borders of the Co islands were decorated with Fe. The confinement within the Co core of the Fe-decorated Co island of Fig. 4.7 was investigated performing the same FT analysis of the spatial modulation of the differential conductance of the Co core as presented before. A parabolic dispersion relation gives a valid description

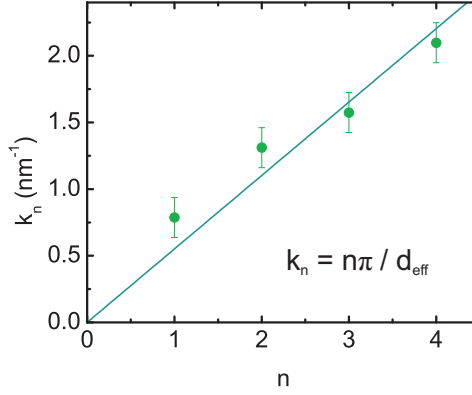


Figure 7.6: Plot of the wave vector as a function of an integer index extracted by applying the 1D "particle-in-a-box" model to the wave vectors obtained from Fig. 4.8. The slope gives the size of the effective confinement length $d_{\text{eff}} = 5.7 \pm 0.4$ nm.

| Direction | Confinement length d_{eff} (nm) | Geometrical height (nm) |
|-----------|--|-------------------------|
| A | 5.5 ± 0.4 | 5.5 ± 0.2 |
| B | 5.6 ± 0.4 | 5.7 ± 0.2 |
| C | 5.7 ± 0.4 | 5.8 ± 0.2 |

Table 7.1: Comparison between confinement lengths d_{eff} and geometrical heights for the Co core in Fig. 7.7

of the experimental data (see Fig. 4.8). The parabolic fit with the equation $E = E_0 + \hbar^2 k^2 / 2m^*$ yields $E_0 = -0.11 \pm 0.03$ and $m^* = 0.34 \pm 0.03 m_e$. The extracted values E_0 and m^* are in line with the discussion presented above for pure Co islands.

The one-dimensional particle-in-a-box model was used also here and Fig. 7.6 shows the plot of the wave vector k_n as a function of n for the symmetry axis C of the Co core of Fig. 4.7. Here, only the relation $k_n(n)$ for the direction C is plotted since the Co core is very regular and all the three different directions give very similar curves. From the slope of the linear fit in Fig. 7.6, the effective confinement length d_{eff} can be extracted. The effective confinement lengths for the three symmetric directions are listed in Table 7.1 and Fig. 7.7 shows a comparison between the extracted d_{eff} and the size of the Co core. The confinement lengths d_{eff} corresponds to the geometrical heights of the Co core, in contrast to pure Co islands, where d_{eff} is 2.4 – 3.1 nm smaller than the geometrical height of the island. Thus, we can conclude that the effect of the Fe decoration is to move the scattering potential barrier right at the border between Fe and Co. What is the origin of this difference?

As discussed above for pure Co islands, the electronic properties at the border of the nano structure, where the electron scattering takes place, are the prime suspects. In order to understand why the position of the potential barrier, which is responsible for the scattering, moves from 1.2 – 1.5 nm away from the island border, in pure the Co island, to right at the Fe-Co border, in

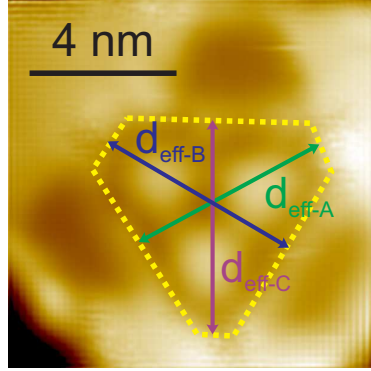


Figure 7.7: Constant current STM image of the Fe-decorated island in on which the measurement were performed. The yellow dashed line indicates the Co core of the Fe-decorated Co island. The arrows indicate the effective confinement lengths extracted from the quantization rule. It is clear that the effective lengths d_{eff} correspond to the geometrical heights of the triangular Co core. Imaging parameters: $V_{gap} = +0.1$ V, $I_t = 1$ nA.

the Fe-decorated Co island, position dependent STS was performed.

Figure 7.8 shows several dI/dV spectra as a function of position across the border between Co and Fe phase-a (a-c) or Co and Fe phase-b (d-f)¹. The black dI/dV spectrum at the bottom of Fig. 7.8(b) (Fig. 7.8(e)) shows clearly the Co 3- d peak at -0.3 V. Moving towards the Co-Fe phase-a (Co-Fe phase-b) border, the Co 3- d peak decreases in intensity and the typical peaks of the Fe phase-a (Fe phase-b) at -0.4 V (-0.2 V) gradually appears. On the basis of the changes of the dI/dV spectra, the transition region between Co and Fe phase-a (Fe phase-b) occurs over a distance of 0.7 nm for both Fe phases. This corresponds to about 3 nearest-neighbor atomic distances of the Cu(111) substrate.

But the most striking observation is that no Co rim state can be observed at the Fermi energy in the dI/dV spectra taken at the Co border. No peak at 0 V can be observed in the dI/dV spectra measured either at the Co-Fe phase-a border or at the Co-Fe phase-b border. Thus, the Fe decoration removes the peculiar Co rim state, which is observed at the edge of the pure Co islands. We propose that without rim state, the scattering potential barrier moves all the way towards the Co-Fe border and therefore, the extracted confinement length d_{eff} correspond to the geometrical height of the Co core. It was shown by Rastei et al. [115] that surface-state electrons on nano islands are significantly affected by the local atomic structure and relaxation. Therefore, we speculate that the Co rim state is closely related to the structural relaxation of the atoms at edge of the Co islands. The structural relaxation of the atoms at the Co island edges alters the local electronic structure and this might be responsible of the formation of the so-called rim state in pure Co islands. In a Fe-decorated Co island, the Co atoms at the edge of the Co core do not undergo the same structural relaxation as in pure Co islands due to the Fe decoration, and consequently, no rim state forms. Note that the absence of the Co rim state, and the almost

¹The two different Fe phases which can be found in our sample were defined in Section 6.3

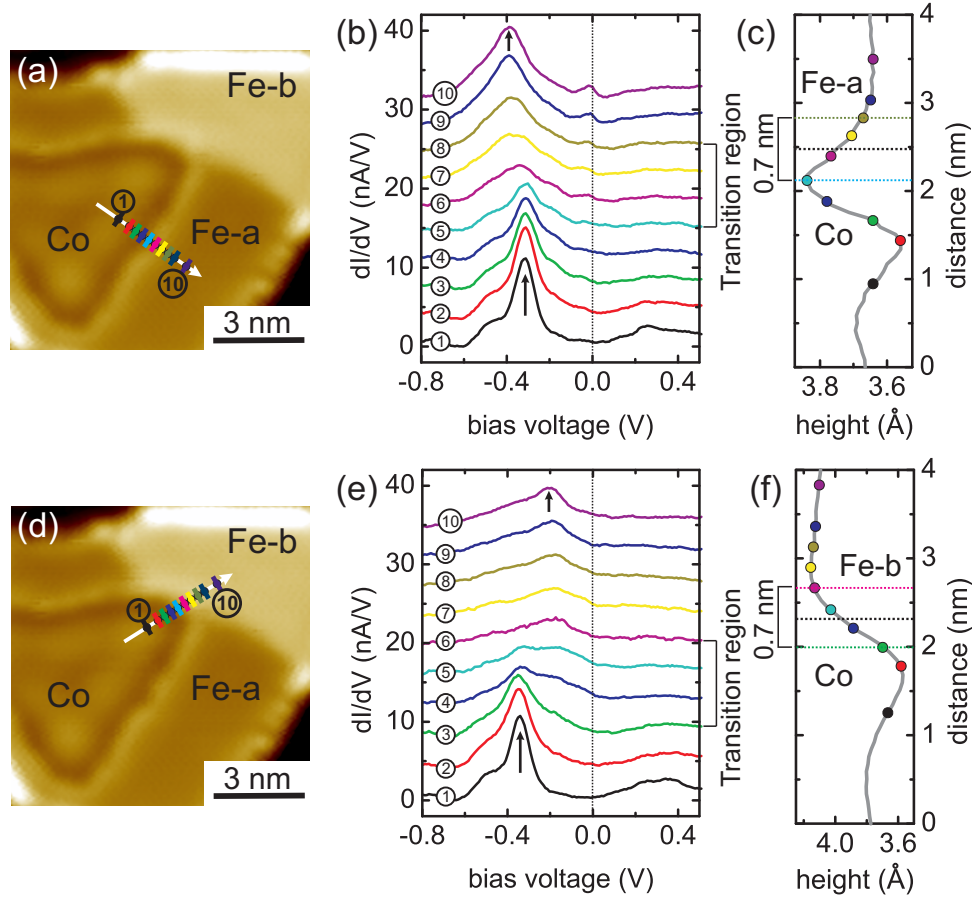


Figure 7.8: (a,d) Constant current STM image of a Fe-decorated island on which the position dependent STS measurements were performed. The white line in (a) and (d) indicate the positions and directions along which the dI/dV spectra in (b) and (e) and the line profiles in (c) and (f) were taken. The line profile in (a) runs from the Co core towards the Fe phase-a. The line profile in (d) runs from the Co core towards the Fe phase-b. (b,e) Spectra of the differential conductance dI/dV measured on the points evidenced in (a) and (d). (c,f) Constant current line profiles along the white arrows in (a) and (d). Measurement parameters: $I_t = 1$ nA, $V_{gap} = +0.1$ V, $I_{stab} = 1$ nA, $V_{stab} = +0.5$ V.

constant energy position of the Co related peak at -0.3 eV, is a first indication of rather constant electronic properties and strain state within the Co core. This assessment is further corroborated by the following discussion of the energy position of the Co 3- d peak.

Another indication of a rather constant strain state of the Co core, which does not vary sensibly at the edge region, comes from the observation of the constant energy position of the 3- d Co peak at -0.3 V in Fig. 7.8(b). It was shown that the energy position of the 3- d Co peak is closely related to the Co-Co interatomic distance [115], and therefore to the local structural relaxations.

Position dependent dI/dV spectra on pure Co islands performed by Rastei et al. [115] and Wedekind [75] show that the 3- d Co peak shifts of about 0.06–0.1 V when moving from the center of the islands towards the Co island edges. This finding was ascribed to the variation of the Co interatomic distance within the island. Figure 7.8(b) does not show a pronounced energy shift of the 3- d Co peak and its energy position stays constant at -0.3 V from spectra 1 to spectra 5. Thus, the hypothesis of a fairly constant Co interatomic distance, and therefore a rather constant strain state, in the Co core can be advanced. This observation is important in view of the discussion on the island size dependence of the magnetic switching of Fe-decorated Co islands discussed in Section 7.7.2.

In conclusion, electron confinement both in pure Co and Fe-decorated Co islands was investigated. In Co islands, the potential barrier responsible of the electron scattering was found to be located around 1.2 – 1.5 nm away from the edge of the islands, towards the inner part of the island. This differs for the Fe-decorated Co islands, where the scattering of the electrons takes place right at the Co-Fe border. This difference is ascribed to the disappearance of the Co rim state at the border of the Co core in Fe-decorated Co islands. We speculate that the rim state is a electronic characteristic raising from the structural relaxations of the atoms at the edges of Co islands. The Co atoms at the edge of Co cores of Fe-decorated Co islands cannot undergo the same structural relaxations as in pure Co islands due to the Fe decoration and the characteristic Co rim state does not appear. The absence of the Co rim state at the Co core borders of Fe-decorated Co islands does not affect electron confinement only, but also magnetism and electron spin dependent properties of the Co cores are influenced. Section 7.7.2 and 7.8.3 will give further insights into these topics.

7.3 Magnetic response and spin polarization of bulk Cr tips

The measurements presented in Section 5.1 demonstrate that bulk Cr tips can be successfully used for in-field sp-STM measurements and no tip-related specific features in the differential conductance dI/dV spectra are observed.

The hysteresis loop of the differential conductance in Fig. 5.3(b) suggests a continuous increase of the z -component of the local magnetic moment of the tip apex towards the field direction with increasing z -field. At first sight the reorientation of the spin moment of a bulk antiferromagnetic material in a modest field of 2 T might come as a surprise. However, Rodary et al. [81] showed by high resolution transmission electron microscopy measurements that clusters at the end of the tip need to be considered in the tunneling process. Thus, the presence of uncompensated spin moments at the tip apex is a reasonable assumption since uncompensated magnetic moments in Cr clusters were already observed experimentally by Payne et al. [177] and treated theoretically by Czerner et al. [178].

An important figure of merit in sp-STs is the spin polarization of the tip as it determines, together with the sample spin polarization, the measured magnetic contrast. Furthermore, knowledge about the tip spin polarization enables to disentangle the contribution from tip and sample in the dI/dV signal and gain detailed information about sample properties. To determine the spin po-

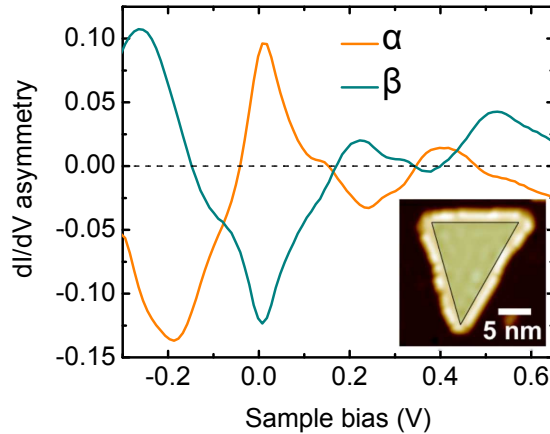


Figure 7.9: Energy dependence of the asymmetry of the differential conductance dI/dV averaged over the highlighted inner part of the Co island shown in the inset (the Co island marked in Fig. 5.2). The two curves refer to two different measurements performed by the same macroscopic bulk Cr tip but with different tip apexes. The tip apex changed between α and β during a spectroscopy scan.

larization of the tip (P_t), asymmetry maps of the differential conductance were measured on the Co island shown in the inset of Fig. 7.9 as described in Section 3.4. Then, the energy dependence of the asymmetry of the differential conductance was extracted averaging each asymmetry map of the differential conductance over the inner part of the Co island, in order to avoid the contribution of the rim state and to average out the modulation of the Co spin polarization (see also supporting material of ref. [95]). The result is shown in Fig. 7.9 (curve α). The asymmetry varies in sign and magnitude with the applied voltage and reaches a maximum value of -0.123 at the Fermi energy. The pronounced voltage dependence of the asymmetry of the differential conductance reflects the energy dependence of the spin polarization of a 2-ML-high Co film [95]. In order to quantitatively extract the spin polarization of the tip, the effect of the tip-sample distance on the extraction of the spin polarization must be taken in account [129, 179]. The energy dependence of the spin polarization of a 2-ML-high Co film (P_s) at 4 \AA away from the surface was calculated by *ab-initio* calculation in ref. [95]. Here, the calculated sample spin polarization P_s was used to extract the tip spin polarization P_t . Using the relation $A = -P_t P_s$ (see Chapter 2), from curve α in Fig. 7.9 we obtain a tip spin polarization $P_t = 0.45$ at the Fermi energy. The calculated spin polarization at the Fermi energy for this tip has the opposite sign and is significantly larger than the spin polarization of the Cr(001) surface ($P = -0.18$) [180]. This value is comparable to the spin polarization obtained for Fe-coated W tips ($P = 0.42$) [34, 181] and it is much larger in comparison with Cr/Co/W tips ($P = -0.1$) [95].

The characterization of the tip spin polarization is important to obtain a correct interpretation of the experimental data since it can change from tip

apex to tip apex, as we discuss in the following. Curve β in Fig. 7.9 shows the measured dI/dV asymmetry averaged over the island after the tip apex changed its configuration unintentionally during an STS measurement. We observed that the overall shape and amplitude of the two curves are very similar, but the sign of the asymmetry of the differential conductance is different. The change in the tip apex could only be noticed from the slightly different shape of the dI/dV spectra, whereas the constant-current image did not show any noteworthy difference after the tip had changed. Moreover, the response of the spin moment of the tip apex to the applied magnetic field did not change. The change in the tip apex can be ascribed to structural modification of the cluster at its apex, which is responsible for the tunneling process. This measurement clearly shows that even a small change in the tip apex can modify the value of the tip spin polarization as well as reverse its sign. This is in line with recent theoretical calculations by Ferriani et al. [182], which reveal that the spin polarization of a Cr ad-atom can strongly change depending on the orientation of the surface on which it is bonded.

In conclusion, a magnetic characterization of bulk Cr tips was performed. The significant spin polarization and the easy fabrication as compared to film covered W tips make bulk Cr tips excellent candidates for antiferromagnetic sp-STM/STS probes.

7.4 Temperature dependent measurements with Fe-coated W tips

Figure 5.4 shows the dependence of the differential conductance dI/dV on the magnetic field measured on the Co cores of single Fe-decorated Co islands. The measurements show clear changes in the slope of the differential conductance signal between -1 T and $+1$ T with temperature. This observation is already a strong hint of a superparamagnetic response of the magnetization of the tip apex.

The abrupt change of the differential conductance in the measurements of Fig. 5.4 is ascribed to the reversal of the Co core magnetization direction. Thus, the dependence of the differential conductance on the magnetic field due to the response of the tip magnetization can be obtained by subtracting the ferromagnetic contribution of the Co island from the measurements of Section 5.2. The results are shown in Fig. 7.10. The labels Co1 and Co2 refer to the two different Co cores of Fig. 5.4 on which the magnetic field dependence of the differential conductance was measured.

The measurements in Fig. 7.10 show remarkable changes of the slope around 0 T with temperature. These curves were calculated from the magnetic field dependence of the differential conductance of Fig. 5.4(b,c) by subtracting the signal change due to the magnetization reversal of the sample. If the increase of the z -component of the magnetic moment of the tip apex was due to the rotation of the tip magnetization direction from the in-plane to out-of-plane direction, these pronounced changes come as a surprise as the magnetic anisotropy constants of Fe can be considered constant in this rather small temperature interval [123, 125, 183]. A possible temperature dependence of the anisotropy of the tip apex does not seem to be responsible for the observed temperature

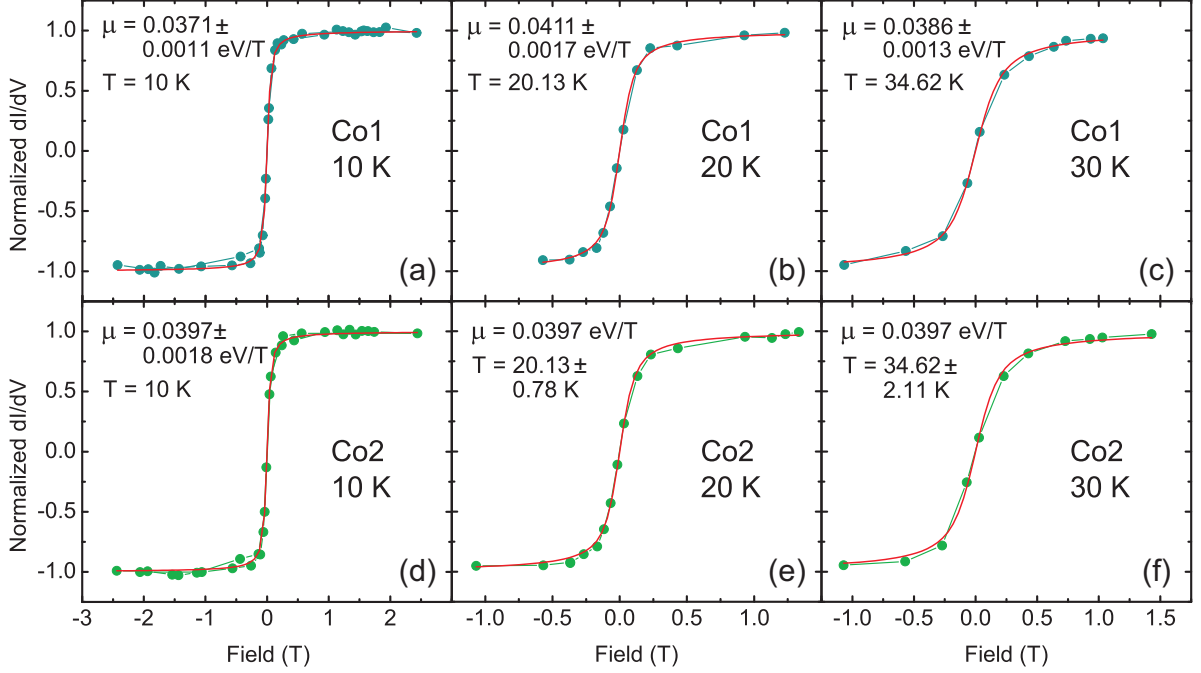


Figure 7.10: Calculated differential conductance dI/dV loops, measured with a 40 ML Fe/W tip, extracted by subtracting the ferromagnetic contribution of the Co magnetization from the magnetic field dependence of the differential conductance of Fig. 5.4(b,c). These calculated curves from the experimental data represent the magnetic response of the 40 ML Fe/W tip measured over the two Co cores Co1 and Co2 in Fig. 5.4(a). The red curves are Langevin fits to the experimental data.

dependence. The temperature induced changes rather point at superparamagnetic response of the magnetization of the tip apex. As a first analysis, the case of isotropic superparamagnetism is considered. Under the assumption of $(KV/k_B T) \ll 1$ (K : anisotropy per unit volume, V : volume of the magnetic cluster at the tip apex, k_B : Boltzmann constant, T : temperature), the thermal agitation energy is so high in respect to the anisotropy energy of the magnetic cluster at the tip apex, that all macrospin directions of the magnetic cluster are equally probable, and the magnetic anisotropy K can be neglected. Therefore, the data can be fitted with the Langevin function $L(x) = \coth(x) - 1/x$, where $x = \mu H/k_B T$ (μ : magnetic moment of the cluster at the tip apex, H : applied field) [124]. The red curves in Fig. 7.10 represent the Langevin fits though the data points. The Langevin function reproduces well the experimental data at each temperature explored here.

The data were analyzed as follows. Firstly, the data at 10 K were fitted with the measuring temperature of 10 K in order to obtain the magnetic moment μ of the magnetic cluster at the apex of the tip. Once checked that the magnetic moments obtained from the fits of the data in Fig. 7.10(a,b) were the same in view of the experimental error, the magnetic moment $\mu = 0.0397$ eV/T was used

to fit the data measured on the so-called Co2 island in order to cross check the temperature reading. The temperatures extracted from the fits in Fig. 7.10(e,f) were then used as fixed parameters in the fits of the the data in Fig. 7.10(b,c) to extract the tip magnetic moment μ .

The temperatures extracted from these fits reproduce well the temperatures imposed by the resistive heater at the STM head. At 30 K a deviation of around 4 K is observed. The origin of this error might come from different factors. At this temperature, the duration of the measurement for each single point in Fig. 7.10(c,f) is longer in respect to the other two temperatures because of the larger noise introduced in the differential conductance signal with increasing temperature. Another factor is the spatial separation between the heater, the Cernox temperature sensor and the sample. With increasing heating power it appears plausible that the thermal equilibrium of the setup is disturbed and larger temperature gradients appear. In any case, the overall agreement looks satisfactory. Also, the magnetic moments extracted from the fits are rather constant in the experimental error bar. Considering an atomic magnetic moment of $3\mu_B$ per Fe atom [184], the magnetic cluster at the tip apex can be estimated to contain some 210–250 Fe atoms, which is a reasonable result in view of previous high resolution transmission electron microscopy (HRTEM) studies [81].

Also the case of anisotropic superparamagnetism was considered to fit the data. In this case, the assumption $(KV/k_B T) \simeq 1$ is made, and the macrospin of the magnetic cluster at the tip apex fluctuates along the easy axis of the cluster only. The difference in respect to the previous case is that the magnetic anisotropy K is explicitly considered in this model. The experimental data in Fig. 7.10(a) were fitted with the function [185]

$$F(H) = -h/2d + (2/\sqrt{\pi d}) \times \frac{\exp(d + h^2/4d) \sinh(h)}{\operatorname{Erfi}(\sqrt{d} + h/2\sqrt{d}) + \operatorname{Erfi}(\sqrt{d} - h/2\sqrt{d})} \quad (7.1)$$

where $d = \beta KN$, $h = \beta\mu_0\mu H$, $\beta = 1/k_B T$ and $\operatorname{Erfi}(x) = (2/\sqrt{\pi}) \int_0^x e^{t^2} dt$ is the imaginary error function (K : anisotropy per atom, N : number of atoms in the magnetic cluster at the tip apex, μ : magnetic moment of the cluster at the tip apex, H : applied field, T : temperature). Considering an atomic magnetic moment of $3\mu_B$ per Fe atom as above, the fit gives $K = 24 \pm 9 \mu\text{eV}/\text{atom}$ and $N = 108 \pm 14$ atoms. From these values we calculate $(KN/k_B T) = 3, 2, 1$ for $T = 10, 20, 30$ K, which validates the previous assumption. Also, a blocking temperature [124] $T_B = KN/25k_B = 1.2$ K results for the cluster at the tip apex. The extracted magnetic anisotropy K is surprisingly large compared to the bulk anisotropy of Fe ($3.9 \mu\text{eV}/\text{atom}$ at 4.2 K) [183] and Fe films on W(110) ($9.4 \mu\text{eV}/\text{atom}$) [186], but it is reasonable in view of the large values reported for nanoscopic systems [23, 77, 187]. Therefore, also an anisotropic superparamagnetic response of the tip apex magnetization can describe the experimental data well. However, a clear cut distinction between isotropic and anisotropic superparamagnetism is difficult for the presented data. Indeed, numerical evaluation shows that the Langevin function $L(\mu H/k_B T)$ and Eq. 7.1 are very similar within this temperature range, i.e. $T \simeq 10-30 T_B$, and both the curves describe the presented data well.

In conclusion, the measurements and the discussion presented above indicate a superparamagnetic response of the tip apex magnetization of Fe-coated W

tips. At this point, we can state that the magnetic sensitivity of the Fe-coated W tips used for the measurements presented in this thesis was always along the direction of the external magnetic field. This implies that only the out-of-plane component of the sample magnetization was detected and no in-plane component was ever probed. At zero field, no spatial orientation of the tip apex magnetic moment is preferred, and no magnetic sensitivity was ever achieved. Thus, for this tips we conclude that at 0 T we cannot detect in-plane sample magnetization. These findings are important for the interpretation of the results presented in Section 6.3 and discussed in Section 7.8.

7.5 Estimation of the induced spin polarization in Cu in proximity of a Co island

The measurements in Section 6.1.1 aim at measuring the spin polarization induced in the Cu surface between two Co islands. The line profiles of the differential conductance dI/dV asymmetry shown in Fig. 6.2 do not reveal any clear modulation of the signal in the Cu channel, but only at the Co edges. This suggests that the induced spin polarization of the Cu surface states is too small to be detected. The estimation of the statistical error presented in Fig. 6.3 indicates that the minimum detectable differential conductance dI/dV asymmetry signal is around 0.02 – 0.03 under these measurement conditions. By similar analysis to that presented in Section 7.3, the spin polarization P_T of the specific bulk Cr tip tip used to perform this experiment was estimated to be 0.35 at the Fermi energy. Therefore, an upper limit of $|P_S| = A/P_T = 0.05 - 0.08$ can be estimated for the Co-induced spin polarization of the Cu surface at the Fermi energy. Note that a tip with larger spin polarization would give a better sensitivity for the detection of minute spin polarization of the sample.

In order to have a theoretical estimation of the induced spin polarization in the Cu surface in proximity of a Co island, *ab-initio* calculations were per-

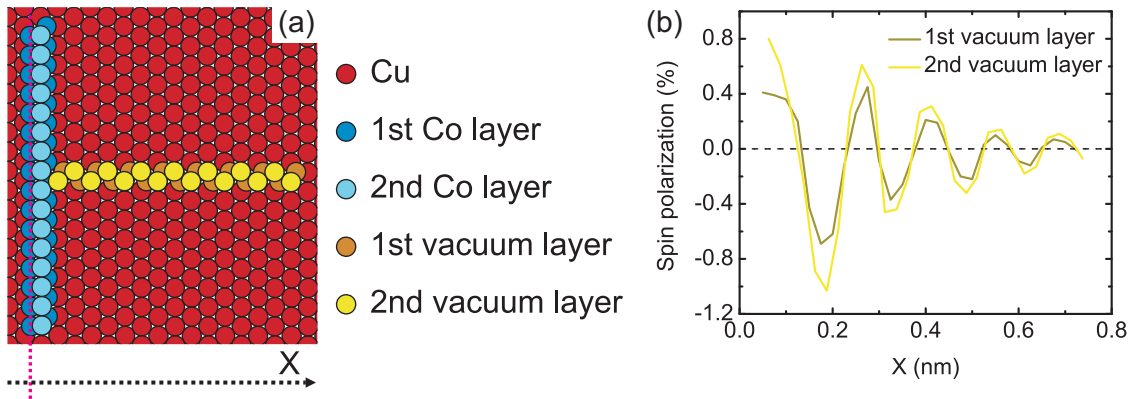


Figure 7.11: (a) Hardsphere model of the system used in the calculations. The magenta dashed line indicate the origin of the X axis. (b) Calculation of the spin polarization at the vacuum spheres for the geometry sketched in (a).

formed². The induced spin polarization in the Cu surface was calculated in the geometry sketched in Fig. 7.11. A two-atomic-layer-high Co stripe runs along the $[1\bar{1}0]$ direction of the Cu(111) and the sample spin polarization is calculated in the first and second vacuum layer above the Cu surface, along the $[11\bar{2}]$ direction. This geometry reflects the orientation of the Co island edges shown in Fig. 6.1. The results of the calculations performed at the Fermi energy are shown in Fig. 7.11. A maximum spin polarization of 1% ($P_S = 0.01$) is calculated in the second vacuum sphere around 0.2 nm away from the Co stripe, and it vanishes around 0.8 nm. These calculations corroborate the estimate done before for the upper limit of the induced spin polarization in the Cu surface states. The calculated minute magnitude of the spin polarization suggests that its value is too small to be reliably detected already at a distance of about one atomic diameter away from Co. Nevertheless, novel insights into spin-dependent electron spill-out near a Co island are accessible, and they are discussed in Section 7.6.

In conclusion, improving the lower limit for the smallest detectable spin polarization remains a challenge for future investigations. Magnetic tips with a bigger spin polarization in bulk materials may be used. However, as it was shown and discussed in previous sections, this tip characteristic is not easy to control and tip spin polarizations larger than 0.4 – 0.5 are rarely achieved. Working at lower temperature also helps to reduce the thermal induced noise and to increase to signal to noise ratio. In any case, this experiment gives an estimate of the smallest spin polarization value detectable with the Omicron cryo-STM used in this thesis, and it is of the order of 5%.

7.6 Spin-dependent Smoluchowski effect

The data presented in Section 6.1.2 provide clear evidence of strong spatial modulations of the spin-dependent electronic properties and transport properties along the edge of a Co island on Cu(111). In order to link these observations to an electron spin dependent charge flow at the Co island edge and to understand how majority and minority states contribute to this effect, first principles calculations were performed³.

In the calculations, the edge of a bilayer high Co island on Cu(111) was mimicked by an infinite stripe of Co atoms, which is four atomic rows wide in the topmost layer and five for the lower layer. The Cu substrate is described by a slab of five layers, with 12 atomic rows in each layer. This structure is sketched in Fig. 7.12(A). The electronic structure at the edge of Co islands was calculated performing simulations for different numbers of atomic rows in the stripe, and it was found that the chosen model describes the main aspects reliably.

Energy and site resolved plots of the calculated total local density of states and for the minority and majority electrons in the vacuum space above the edge of the Co stripe are presented in Fig. 7.12(B). The total density of states reveals a non-trivial spatial and energy dependence of the density of states.

²Calculations are kindly provided by L. Niebergall and V. S. Stepanyuk from the theory department at the Max-Planck-Institute of Halle.

³Calculations are kindly provided by O. P. Polyakov, O. V. Stepanyuk, A. M. Saletsky and V. S. Stepanyuk from the Faculty of Physics of Moscow State University and the theory department at the Max-Planck-Institute of Halle. A correspondingly publication has been submitted [61].

The total density of states is strongly reduced above the step edge (position 3). Qualitatively we find that the total electron density of states at any given energy is reduced above the Co stripe (position 1) and increased above the Cu surface (position 6). Thus, a positive surface dipole is expected near the step edge, in accordance with the Smoluchowski's model. However, the plot also indicates that states of different energy show a different spatial variation. Thus, electron charge spill out and smoothing is an energy dependent phenomenon.

The plots of the minority and majority states in Fig. 7.12(B) reveal that the local density of states (LDOS) for minority electrons is significantly larger than for majority electrons. The minority LDOS exhibits strong spatial variations across the step, which vary drastically with energy. In both spin channels a deep minimum of the LDOS near the top of the step, which corresponds to the vacuum sphere 3, is revealed. This reflects the spill out of electronic charge near the top of the step, in accordance with Smoluchowski's description. Our treatment advances the Smoluchowski description by identifying that charge redistribution at step edges affects minority and majority electrons differently, as outlined next.

There is a strong local increase in the electron density of the majority electrons at the bottom of the step. This contrasts with the LDOS of the minority electrons, where the LDOS at the bottom is close to that on the top of the step. The behavior of the minority *sp* electrons is strongly affected by the localized minority *d*-rim states observed at the edge of Co islands on Cu(111) in spin-polarized STS experiments [95, 106]. The rim states have been clearly identified as spin-polarized states having an electronic structure strongly different from that of the islands interior.

The above results give clear evidence of the spin-dependent charge redistribution across a step of a magnetic nanostructure. In other words, one can speak of a spin-dependent Smoluchowski effect at the edges of magnetic nanostructures.

One very interesting and important issue predicted by these results is the possible strong impact of the spin-dependent charge redistribution on the spin-polarization of electrons above step edges. In particular, one might expect significant spatial variations of the spin-polarization near step edges. The spin-polarization P is defined as

$$P(E) = \frac{n_{\uparrow}(E) - n_{\downarrow}(E)}{n_{\uparrow}(E) + n_{\downarrow}(E)} \quad (7.2)$$

where $n_{\uparrow}(E)$ and $n_{\downarrow}(E)$ are the LDOS for the majority and minority electrons, respectively. The calculated spin-polarization near the edge of the Co island is presented in Fig. 7.13⁴.

In order to determine the spin-polarization above the step edge of the Co island shown in Fig. 6.4, the asymmetry of the differential conductance was extracted across the same step edge. This asymmetry is proportional to the spin polarization of the sample P_S . Three line profiles of the asymmetry of the differential conductance are shown in Fig. 6.5 for different bias voltages. The comparison between the experimental data of Fig. 6.5 and the theoretical data

⁴The position of occupied minority Co *d*-states calculated by VASP or by the Korringa-Kohn-Rostoker method is about 0.1 eV higher than the experimental results [97, 115]. Therefore, the Fermi level on the map of the spin-polarization was shifted to the higher energy by 0.1 eV.

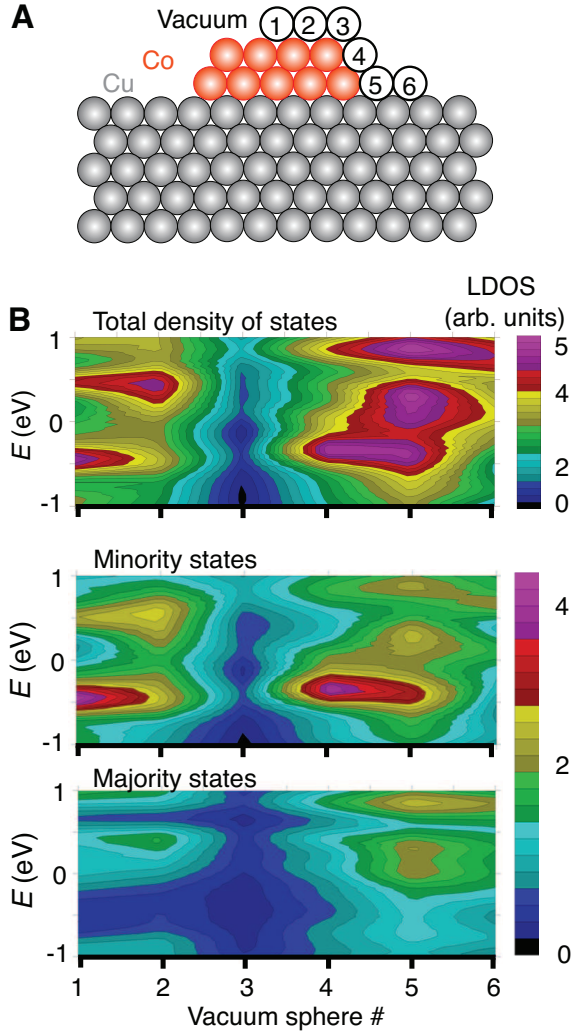


Figure 7.12: (a) Hardsphere model of the system used in the calculations. Note that all atomic positions were allowed to relax. (b) Plots of the energy dependence of the total density of states (top) and of the spin-resolved density of states of minority (center) and majority (bottom) electrons as calculated at the position of the vacuum spheres identified in (a). Adopted from ref. [61].

of Fig. 7.13 requires an alignment of the horizontal spatial axis. The position of half step height was chosen as the common point, i.e. the position 4 nm of the experimental line scans corresponds to the lateral position of vacuum sphere 4. Our data reveal that both experiment and theory observe the same location of the strongest changes of the asymmetry and spin polarization signal, which is located near the upper section of the step edge, i.e. at position 3 – 3.5 nm in Fig. 6.5 and at position 3 in Fig. 7.13.

The experimental data obtained at a gap voltage of -0.5 V (Fig. 6.5(A)) show a negative value near the top of the Co island step, and it turns slightly

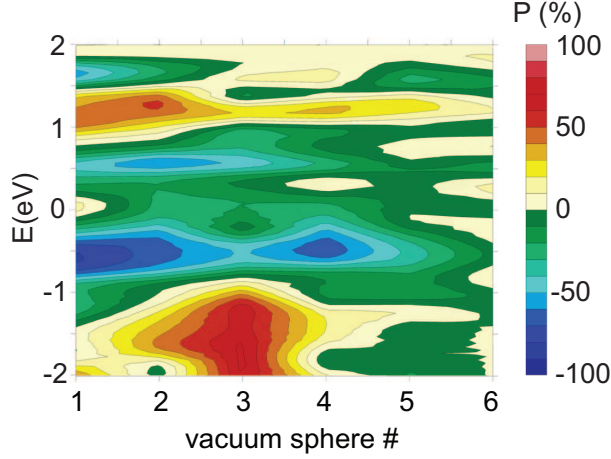


Figure 7.13: Calculation of the energy dependence of the spin-polarization P at the vacuum spheres across the step edge, as defined in Fig. 7.12(a). Adopted from ref. [61].

positive before going to zero at the bottom of the step. This resembles favorably the behavior of the spin polarization along the step edge as indicated for a horizontal section through Fig. 7.13 at -0.5 eV. For -0.05 V (Fig. 6.5B), the asymmetry of the differential conductance shows small positive values near the upper step edge, and negative values at half height of the step edge (4 nm), changing to zero above the Cu surface. This behavior agrees favorably with the calculation presented in Fig. 7.13. Also at $+0.5$ V (Fig. 6.5(C)) the agreement with theory is comforting as we measure a negative asymmetry of the differential conductance, indicative of a negative spin polarization over the complete step edge, in agreement with theory.

This spatial modulation of the spin-polarization at the edge of the Co island impacts also the TMR ratio, as it is evident from Fig. 6.6. The TMR ratio is related to the spin polarization of tip P_T and sample P_S by [96]

$$TMR = \frac{I_P - I_{AP}}{I_{AP}} = \frac{2P_T(E)P_S(E)}{1 - P_T(E)P_S(E)} \quad (7.3)$$

as outlined in Chapter 2. For small spin polarizations of the tip and the sample, the TMR ratio is proportional to the spin polarization above the sample [96]. Thus, our combined calculations and experiments indicate a pronounced spatial variation of the TMR ratio near steps which is ascribed to the spin-dependent Smoluchowski effect.

In conclusion, this combined theoretical and experimental study establishes the spin-dependence of the Smoluchowski effect at the edge of a Co nanostructure for the first time. The implications of the spin-dependent Smoluchowski effect are manifold for spin dependent transport, where tunnel current, differential conductance and spin polarization are effected. The exploitation of the spin-dependent Smoluchowski effect opens a new way to tune the TMR of nano structured magnetic tunnel junctions on a scale of a few Angstroms [61].

7.7 Magnetization reversal of individual Co and Fe-decorated Co islands

7.7.1 Co nano islands

The results presented in Section 6.2.1 showed a pronounced size dependence of the switching field H_{sw} of single Co islands on Cu(111) (see Fig. 6.8). This observation is discussed in this section in view of a possible thermally assisted magnetization reversal process [77].

The dependence of the switching field on island size shows two regimes. The switching field increases up to an island size of 7500 atoms, and it decreases for islands larger than 7500 atoms. The overall dependence of the switching field on islands size is *qualitatively* easily understood. Small islands with less than a few hundred atoms are superparamagnetic at 8 K, and their switching field is zero. With increasing island size the magnetization is blocked on the time scale of our experiment (100 s), and a switching field is observed. Thermal assisted magnetization reversal is the switching mechanism for island sizes up to 7500 atoms [74,188]. The larger the island, the less important is the thermal agitation for the reversal, and the switching field increases sharply towards a value which is given by the Stoner-Wohlfarth model $H_{max} = 2K/M$ [189], where K is the effective anisotropy, and M the magnetization. With increasing islands size, domain nucleation and growth becomes feasible as reversal mechanism and the switching field decreases for larger islands. This mechanism characterizes the reversal process for islands bigger than 7500 atoms.

One might be tempted to assume that islands smaller than 7500 atoms are characterized by magnetization reversal by coherent rotation of a macrospin, which changes to reversal by domain nucleation and growth for islands with more than 7500 atoms. The transition from thermally assisted magnetization reversal of a macrospin to reversal by domain formation has already been described some 50 years ago in a study of the magnetization reversal of ensembles of FeCo alloy nano particles [74], and it appears tempting to apply it also here. However, our analysis reveals that this approach fails to describe the data *quantitatively* [77, 78].

To unravel the physics of the reversal mechanism we extract the energy barrier ΔE of magnetization reversal from the switching field H_{sw} as [62,188]

$$H_{sw} = \frac{2\Delta E}{N\mu} \left[1 - \left(\frac{k_B T}{\Delta E} \ln \frac{t_{meas}}{\tau_0} \right)^{1/2} \right] \quad (7.4)$$

where $\mu = 1.8 \mu_B$ is the magnetic moment per atom, $\tau_0 = 10^{-10}$ [65] and $t_{meas} = 100$ s, which reflects the time scale of our experiment [77].

Figure 7.14(a) shows the resulting compilation of the data on the energy barrier as a function of island size, where all switching fields plotted in Fig. 6.8 have been evaluated using Eq. 7.4. Figure 7.14(b) shows a zoom-in for smaller N . The data points are described by a linear dependence of ΔE on N up to $N \simeq 7500$ atoms. Data points for $N > 7500$ deviate clearly from this linear dependence. The data points for $N < 7500$ were fitted with the relation $\Delta E_{lin}(N) = K(N - N_0)$. The slope gives $K = 0.15$ meV/atom, and we observe an offset of $N_0 = 870 \pm 93$ atoms. The offset N_0 comes as a surprise and it

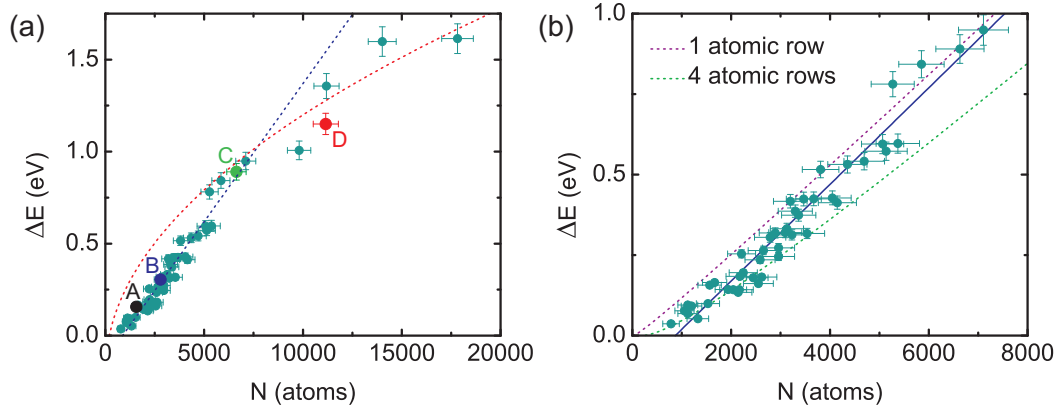


Figure 7.14: (a) Island size dependence of the energy barrier ΔE . The blue curve is a linear fit $\Delta E_{lin}(N) = K(N - N_0)$. The red curve shows the calculated energy barrier for domain wall formation $\Delta E_{dw}(N) = 4\sigma\sqrt{AK}$. The labels identify the data for the islands of fig. 6.7. (b) The solid blue line is the same as in (a). The function $K(N - N_{rim})$ is plotted for different rim widths of 1 and 4 atomic rows, respectively, with purple and green dashed lines [77].

suggests that only a reduced number of atoms ($N - N_0$) contributes to the magnetic anisotropy K . Therefore, the offset N_0 can be interpreted as the number of atoms with vanishing anisotropy. This is in contrast to the expectation of a simple macrospin model discussed above, where all atoms contribute equally.

We propose that the islands are magnetically inhomogeneous, where the rim atoms are magnetically soft and do not contribute to the magnetic anisotropy K . To elucidate this point, Figure 7.14(b) plots the energy barrier $\Delta E_{lin}(N)$ for two different rim widths of one and four atomic rows. The plot indicates that the experimental data fall in between these limiting cases. Therefore, we conclude that Co islands show a 1 – 4 atomic wide region of vanishing magnetic anisotropy located at their outer rims. Moreover, position resolved measurements of the differential conductance by STM have revealed inhomogeneous electronic structure for Co islands. Almost spatially-independent spectroscopy is observed in the center region of large island, whereas specific edge-related features appear near the edge region [95, 106, 115]. We speculate that these spatial variations of the electronic structures may also influence the magnetic anisotropy of the islands. On the basis of this observations, Co islands may be considered as a one-element exchange-spring system [190]. The rim contributes to the magnetization, but not to the magnetic anisotropy. We may consider the Co atoms near the rim magnetically soft, i.e. they show a negligible magnetic anisotropy as compared to the inner part of the Co island.

Figure 7.14(a) shows that the energy barrier ΔE deviates from the linear fit for $N \geq 7500$ atoms. Here, the data points are fitted with the energy cost for domain wall formation $\Delta E_{dw}(N) = 4\sigma\sqrt{AK}$ [62]. Where σ is the area of the domain wall, and it is given by the vertical cross-section $\sigma = d \times l$ with $d = 2$ atoms and l the geometric height of the inner part (without considering the magnetically soft rim), given by the STM measurements for each island. $A = 27.1$ meV/atom is the exchange constant and $K = 0.15 \pm 0.005$ meV/atom

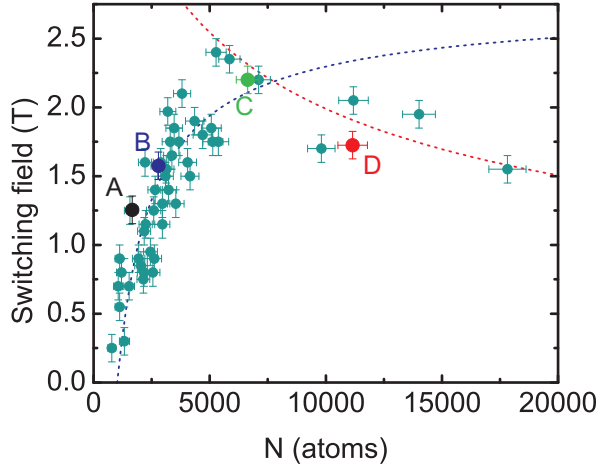


Figure 7.15: Switching fields of 54 individual Co islands of different size. Data points of islands A to D from Fig. 6.7 are indicated. The blue and red lines are calculated from two different reversal mechanism, i.e. coherent rotation and domain wall formation respectively [77].

is the anisotropy energy density. The red dotted line in Fig. 7.14(a) shows the curve $\Delta E_{dw}(N)$. Note that the calculated energy barrier agrees optimally with the measured data points.

The calculated curves for the switching fields corresponding to ΔE_{lin} and ΔE_{dw} are shown as blue and red curves, respectively, in Fig. 7.15. The experimental data are described very well by the calculated curves, which gives further evidence of the reversal mechanism discussed here.

In conclusion, two regimes for the size dependence of the switching fields H_{sw} of Co nano islands, which are ascribed to two magnetization reversal mechanisms, are identified. The switching field of islands smaller than 7500 atoms increases with island size, and the magnetization reversal shows the characteristics of an exchange-spring magnet. We propose that the island rim is magnetically soft, i.e. with negligible magnetic anisotropy as compared to the inner part of the Co island. The switching field decreases for larger islands and this is ascribed to a crossover from a magnetization reversal characteristic of a exchange-spring magnet to a magnetization reversal via domain wall formation. These measurements have been recently published in ref. [77], and are reported here with the purpose to be the basis of the discussion on the size dependence of the switching fields of Fe-decorated Co islands presented in the next section.

7.7.2 Fe-decorated Co nano islands

The measurements presented in Section 6.2.2 show that the Co core of Fe-decorated Co islands remains ferromagnetic with out-of-plane easy axis upon Fe decoration. Inspecting Fig. 6.10(b) it is clear that the Fe decoration affects the Co core switching field H_{sw} , inducing larger H_{sw} up to about 2000 atoms. However, from a first inspection, it is not evident how an increase of the island size influences the switching field.

To analyze the data quantitatively, the energy barrier ΔE is derived from H_{sw} in Fig. 6.10(b) using Eq. 7.4. Figure 7.16 shows the compilation of the obtained energy barriers as a function of the size of the Co cores. A linear fit of the data points with the relation $\Delta E_{lin}(N) = K(N - N_0)$ gives $K = 0.105 \pm 0.005$ meV/atom and an offset $N_0 = -55 \pm 76$ atoms. Two remarkably different results are obtained in comparison with the analysis of pure Co islands. Firstly, the magnetic anisotropy constant K is reduced as compared to the value extracted for pure Co islands ($K = 0.15$ meV/atom) and secondly, the offset N_0 is zero within the error margin, in contrast to the offset discussed for pure Co islands.

A clue to understand the disappearance of the offset N_0 can be drawn linking the discussion on electron confinement within Co and Fe-decorated Co islands in Section 7.2 with that on magnetization reversal of Co islands in Section 7.7.1. In the previous section, the offset N_0 was correlated to the number of atoms at the rim N_{rim} , and these rim atoms were considered magnetically soft. It was proposed that Co atoms near the rim show a negligible magnetic anisotropy as compared to the inner part of the Co island [77]. The width of the magnetically soft area corresponds roughly to the extension of the so-called electronic rim state. In Section 7.2, position dependent dI/dV spectra show clearly the disappearance of the characteristic Co rim state at the Co-Fe border in Fe-decorated Co islands. Thus, it is tempting to correlate the vanishing N_0 with the absence of the electronic rim state. The borders of the Co cores in Fe-decorated Co islands do not show the electronic rim state. Therefore, we may speculate that all atoms of the Co cores contribute to the magnetic anisotropy equally.

The second remarkable result of the fit is a 30% reduction of the magnetic

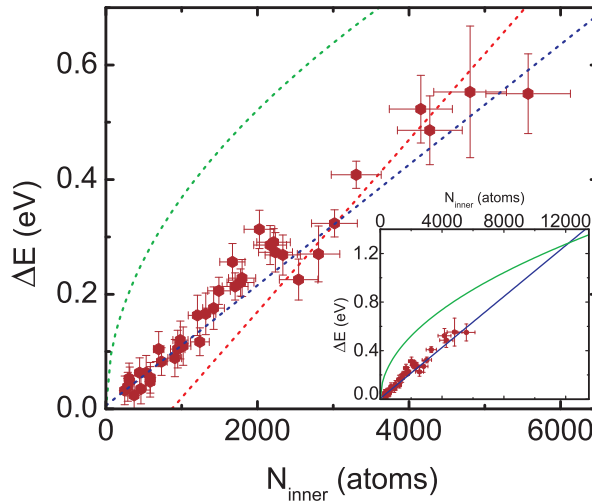


Figure 7.16: Dependence of the energy barrier ΔE from the size of the inner Co core. The blue dashed curve is a linear fit $\Delta E(N) = K(N - N_0)$. The red dashed curve is the linear fit ΔE_{lin} obtained in Fig. 7.14 for pure Co islands. The green curve shows the calculated energy barrier for domain wall formation $\Delta E(N) = 4\sigma\sqrt{AK}$. The inset shows that the crossing point between the two curves occurs around $N_{inner} = 12000$.

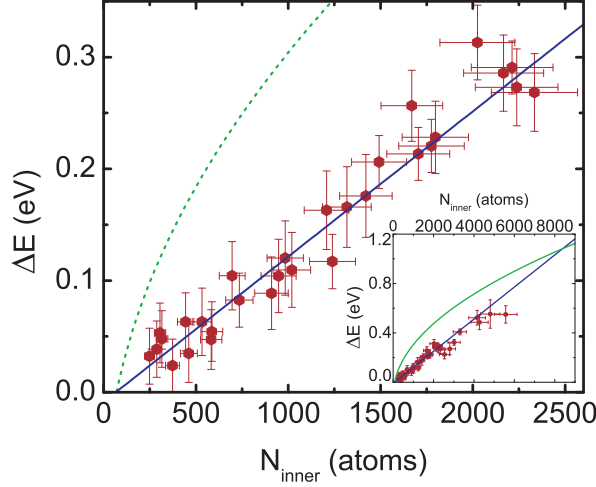


Figure 7.17: Dependence of the energy barrier ΔE on the size of the inner Co core for $N_{inner} < 2500$. The blue line is a linear fit $\Delta E(N) = K(N - N_0)$. The green curve shows the calculated energy barrier for domain wall formation $\Delta E(N) = 4\sigma\sqrt{AK}$. The inset shows that the crossing point between the two curves occurs around $N_{inner} = 8300$.

anisotropy K . At a first sight, this is a surprising result in view of Fig. 6.10(b), which shows larger switching fields H_{sw} for Fe-decorated Co islands as compared to pure Co islands up to about 2000–2500 atoms of the Co core. This apparent discrepancy is readily understood considering that a number of atoms N_{rim} do not contribute to the magnetic anisotropy K in pure Co islands, as discussed in the previous section. The Co atoms of pure Co islands have a larger magnetic anisotropy but only $(N - N_{rim})$ of them contribute to the energy barrier ΔE , which determines the switching field H_{sw} (see also Eq. 7.4). On the other hand, the Co atoms in the Co core of Fe-decorated Co islands have a smaller magnetic anisotropy but all of them contribute to the energy barrier ΔE of the magnetization reversal. Therefore, the energy barrier ΔE for the Co cores of Fe-decorated Co islands results larger than the energy barrier of pure Co islands up to a value of almost 3000 atoms, and the switching fields H_{sw} of Fig. 6.10(b) follow the same trend. This can be seen clearly in Fig. 7.16, where the two linear fits corresponding to the energy barriers of the magnetization reversal of pure Co islands (red curve) and Fe-decorated Co islands (blue curve) intercept at around $N = 3000$.

Two basically different mechanisms may be the keys to understand the reduction of the magnetic anisotropy in the Co cores of Fe-decorated Co islands. The first explanation may come by describing the Fe-decorated Co islands with an exchange spring model, as discussed for pure Co islands in the previous section. The difference between the random scatter of H_{sw} as a function of N_{tot} (total number of atoms in the Fe-decorated Co island) in Fig. 6.10(a) and the clear increase of H_{sw} with N_{inner} (atoms in Co core) in Fig. 6.10(b) suggests that the Fe decoration does not contribute to the magnetic anisotropy of the system. However, it is likely that the Fe decoration introduces an additional magnetic

moment which increases the overall magnetization of the single island and favors an early switch of the magnetization direction as compared to a pure Co island with the size of the Co core only. As a result, the magnetic anisotropy of the atoms in the Co core is apparently reduced. Although this may be a reasonable assumption, the measurements presented in Section 6.3 show that the spin dependent properties of the Fe which decorates the Co islands are far from trivial and this explanation sounds too simplistic.

Another mechanism which may be responsible of the reduction of K is atomic relaxation. Changes of magnetic anisotropy up to $\pm 30\%$ were reported by Nahas et al. [191] and Campiglio et al. [192] for Au and Pt-decorated (and capped) Co islands on Au(111). Molecular dynamics simulations show that Co islands undergoes a substantial in-plane deformation due to atomic relaxations upon Au and Pt decoration and these relaxations have strong impact on the magnetic anisotropy of the system. Position dependent measurements of the differential conductance dI/dV discussed in Section 7.2 indicate a variation of the strain state of the Co cores of Fe-decorated Co islands in respect to pure Co islands. Therefore, structural relaxations may play an important role in modifying the magnetic anisotropy also in this system. The Fe decoration may change the overall strain state of the Co core with a consequent modification of the magnetic anisotropy. This leads to a smaller magnetic anisotropy per Co atom as compared to pure Co islands. Then, we speculate that the variation of the lattice strain within the Co islands leads to an enhanced magnetic anisotropy.

In order to understand whether domain wall formation plays a role as reversal mechanism of the largest Fe-decorated Co islands studied here, the energy cost for domain wall formation $\Delta E_{dw}(N) = 4\sigma\sqrt{AK}$ is calculated [62]. Where σ is the area of the domain wall and is calculated from the vertical cross-section $\sigma = d \times l$ with $d = 2$ atoms and l the geometric height of the inner Co core, given by the STM measurements for each island. $A = 27.1$ meV/atom is the exchange constant and $K = 0.105$ meV/atom is the anisotropy energy density. The green dotted curve in Fig. 7.16 shows the curve $\Delta E_{dw}(N)$. The curve $\Delta E_{dw}(N)$ is far above the data points and it crosses $\Delta E_{lin}(N)$ for $N = 12000$. Therefore, domain wall formation is not the reversal mechanism for any islands investigated here.

A closer inspection of Fig. 7.16 reveals that the data points for $N < 2500$ atoms seem to follow a steeper slope in respect to those for $N > 2500$ atoms. For this reason, the data points for $N < 2500$ atoms were fitted with the function $\Delta E_{lin}(N)$ which gives $K = 0.130 \pm 0.006$ meV/atom and $N_0 = 56 \pm 66$ atoms (Fig. 7.17). The numbers extracted from the fit are different but the discussion is qualitatively the same done for the previous case, i.e. the offset N_0 due to the magnetically soft atoms at the rim is removed, and we ascribe it to the disappearance of the rim state at the Co core borders. Also the magnetic anisotropy K is reduced, although the difference in respect to pure Co islands is not as remarkable as before. The energy cost for domain wall formation $\Delta E_{dw}(N)$ was also calculated and the curve runs above all the data points (green dotted line in Fig. 7.17). The crossing with the function $\Delta E_{lin}(N)$ occurs at 8300 atoms and also in this case no data point can be described by a reversal caused by domain wall formation.

The switching fields corresponding to $K = 0.105$ meV/atom and $K = 0.13$ meV/atom are shown as dotted blue and green curves, respectively, in Fig. 7.18. Most of the data points are located between these two curves but the

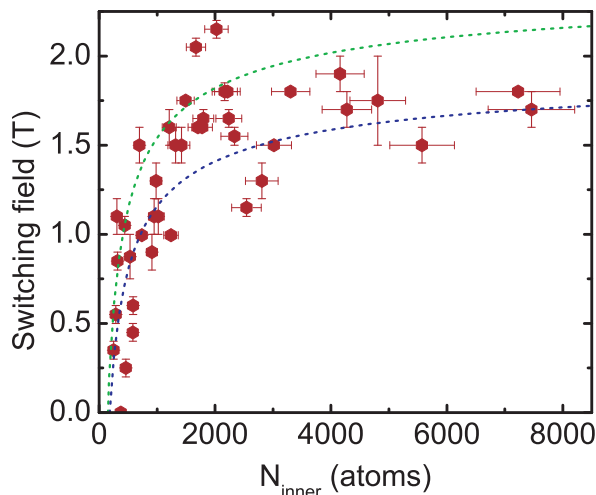


Figure 7.18: Switching fields of 41 individual Fe-decorated Co islands of different size. The blue and green curves are calculated from the coherent rotation reversal mechanism using two different anisotropy constants K obtained from the fits in Fig. 7.16 and Fig. 7.17.

scatter is substantial. This scatter might arise from the different ratio between Fe phase-a and phase-b present in the Fe decoration. As it was shown in Section 6.3 and discussed in the next section, the Fe decoration shows two different phases and these phases present distinct different magnetic properties. Therefore, it is reasonable to assume that the two Fe phases have different interaction with the Co core and influence the switching field of the Co core differently.

Another indication that the thermally assisted coherent rotation model does not describe fully the experimental data, and more complex scenarios must be considered also in this case, comes from the analysis of the temperature dependence of the switching fields of the so-called Co1 and Co2 cores of Fig. 5.4. Figure 7.19 shows the temperature dependence of the switching fields extracted from the field dependence of the differential conductance of Fig. 5.4. The red and black solid lines represent the fits with the Eq. 7.4 through the data points. The fits give $K = 0.125 \pm 0.01$ meV for the Co core Co1 and $K = 0.103 \pm 0.02$ meV for the Co core Co2. The two values for the magnetic anisotropy K are in agreement with the values extracted from the fits in Fig. 7.16 and Fig. 7.17. However, whereas the Néel-Brown model for thermal assisted coherent rotation reversal describes the temperature dependence of the switching field of the Co core Co2 reasonably, it fails to describe the data for the Co core Co1.

In conclusion, the first investigation of the size dependence of the switching field for individual core-shell Co/Fe structures is presented. In contrast to the case of pure Co islands on Cu(111), no indication for reversal by domain nucleation and growth is observed. The Fe decoration removes the magnetically soft rim of Co islands and decreases the magnetic anisotropy of the system. Further insights into the understanding of how the different Fe phases influence the Co core switching fields, and its temperature dependence, will be the topic of future studies.

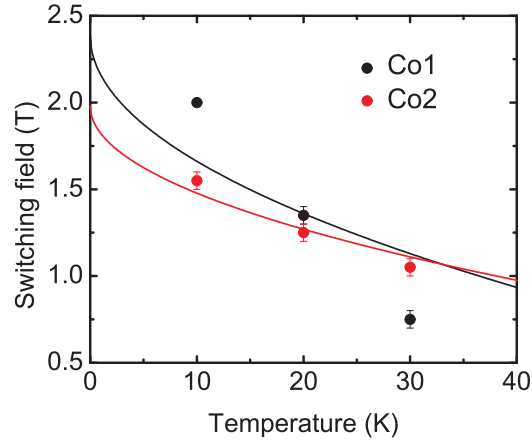


Figure 7.19: Temperature dependence of the switching field for the the two Co cores Co1 and Co2 of Fig. 5.4.

A word of caution appears appropriate. We cannot measure the anisotropy directly, but we rely on quantitative analysis of the switching fields. Thus, we consider fairly simple reversal models, whereas more complicated reversal scenarios cannot be excluded a priori. Further theoretical work on this direction might elucidate this aspect further.

7.8 Novel magnetic structure of nano structured Fe on Cu(111)

7.8.1 The stripe pattern of Fe phase-b

The measurements presented in Section 6.3 indicate spatial variation of the spin dependent electronic properties of Fe phase-b, both for pure Fe phase-b islands and for Fe phase-b regions at the decoration of Co cores. An unexpected stripe-like modulation of the differential conductance dI/dV appears in maps of the differential conductance measured in-field with magnetic tips (Fe-coated W tips) on Fe phase-b regions. Figure 6.13 and Fig. 6.14 show that this characteristic modulation of the differential conductance is only visible when the magnetic field is applied. Two scenarios are possible to explain the absence of magnetic contrast at 0 T. The first scenario assumes that our tips have an in-plane magnetization direction at 0 T and no in-plane component of the magnetization of the stripe-pattern in the Fe phase-b occurs. The second scenario which would explain the absence of magnetic contrast at 0 T is a superparamagnetic response of the magnetization of the tip apex to the magnetic field. At this point, thanks to the temperature dependent measurements performed with Fe-covered W tips in Section 5.2 and discussed in Section 7.4, we can state that the Fe-coated W tips used in this thesis always showed a superparamagnetic response of the local magnetic moment of the tip apex. Therefore, no magnetic signal is detectable at 0 T, and in-plane magnetic sensitivity is never achieved at any magnetic field. All the measurements shown in Section 6.3 and discussed here are sensitive to

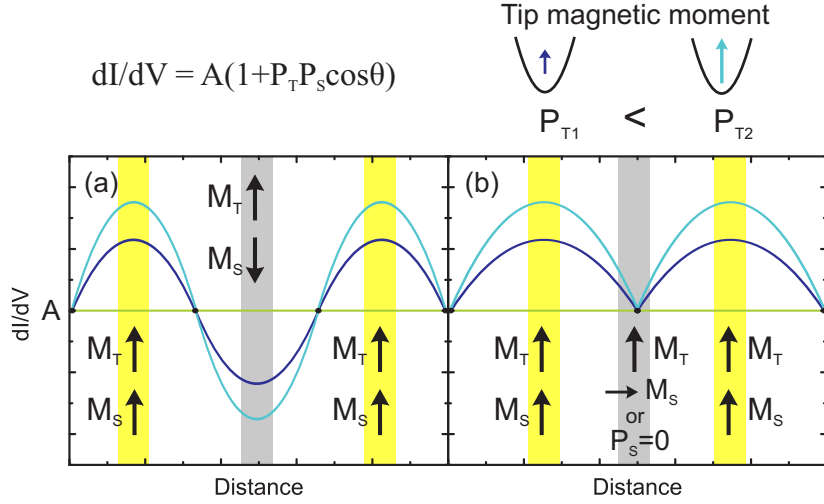


Figure 7.20: Two configurations of the sample local magnetic moments which can produce the stripe-like modulation of the differential conductance dI/dV observed in Fe phase-b areas. The black arrows represent the out-of-plane component of the sample magnetization. The horizontal green line represents the differential conductance in absence of magnetic signal. The violet and cyan curve sketch two modulations of the differential conductance signal obtained with two different magnitudes of the tip spin polarization. The cyan curve is obtained with a larger tip spin polarization P_T as compared to the violet curve, i.e. $P_{T1} < P_{T2}$.

out-of-plane local magnetization of the sample only.

Let us focus on pure Fe phase-b islands now. Figure 6.13(g) reveals that the differential conductance dI/dV oscillates around the line measured at 0 T. This observation indicates that bright and dark stripes in Fig. 6.13 correspond to regions with opposite magnetization direction. Figure 7.20 explains the concept, and the formula $dI/dV = A(1 + P_T P_S \cos \theta)$ cites the relation between the differential conductance dI/dV , the spin polarization of tip P_T and sample P_S and the angle θ between tip and sample magnetization (see Chapter 2). A is a proportional constant, which corresponds to the differential conductance dI/dV in absence of magnetic contrast, i.e. $P_T = 0$ or $P_S = 0$ or $\theta = 90^\circ$. Figure 7.20(a,b) represent two different scenarios, which produce the same stripe-like modulation of the differential conductance qualitatively. For both cases maxima and minima in the dI/dV signal are obtained, which correspond to bright and dark lines in the maps of the differential conductance. Black arrows indicate the out-of-plane component of the local sample magnetization. Minima in the differential conductance (dark lines) can be due to the opposite direction of the sample magnetization in respect to that of bright lines (Fig. 7.20(a)) or can be due to the absence of magnetic signal (Fig. 7.20(b)). Vanishing magnetic signal can result either from an in-plane orientation of the sample local magnetic moment or from a null sample spin polarization. However, the modulations of the differential conductance induced by the configurations of the local magnetic moments in the two figures are different as referred to the green line indicating

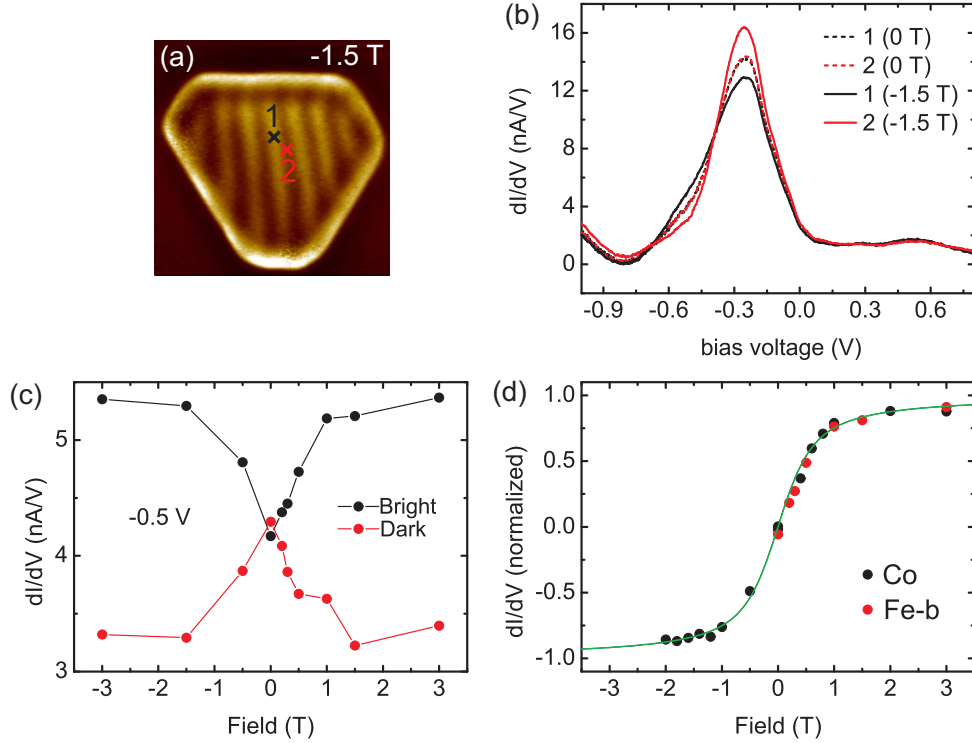


Figure 7.21: (a) Map of the differential conductance dI/dV of the Fe phase-b island of Fig. 6.13(a) measured at -1.5 T. The black and red marks indicate the points where the dI/dV spectra shown in (b) were measured. (b) Spectra of the differential conductance dI/dV measured at different magnetic field values at the positions marked in (a). (c) Dependence of the dI/dV signal at -0.5 V on the magnetic field for the two positions marked in (a), corresponding to bright and dark stripes. (d) Dependence of the dI/dV signal on the magnetic field measured on the Co core of a Fe-decorated Co island and on the position 1 (bright stripe) in (a). The green line represents the Langevin fit of the black data points corresponding to the measurements on Co. Measurement parameters: $I_t = 1$ nA, $V_{gap} = -0.5$ V, $I_{stab} = 1$ nA, $V_{stab} = +0.5$ V.

the absence of magnetic signal (0 T). The arrangement of the sample magnetization in Fig. 7.20(a) produces modulations in the dI/dV signal, which oscillate around the green line. Whereas the magnetic configuration of Fig 7.20(b) produces modulations in the dI/dV signal, which are always above the differential conductance signal measured at 0 T in absence of magnetic signal. Therefore, the model of Fig. 7.20(b) can be discarded as it does not produce modulations of the differential conductance in agreement with the experimental observations of Fig. 6.13(g). On the other hand, the model of Fig. 7.20(a) does not only produces modulations of the differential conductance around the green line, in agreement with the experimental observations, but also the increase of the amplitude of the oscillations in the differential conductance induced by a larger z -component of the tip magnetic moment is produced correctly.

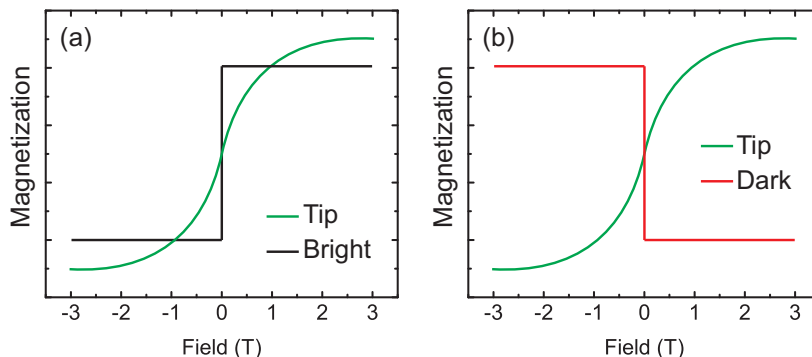


Figure 7.22: Sketches showing the tip and sample local magnetization loops which would provide the magnetic field dependence of the differential conductance dI/dV of Fig. 7.21(c) for bright and dark stripes.

Another important question arises from the observations of the measurements presented in Fig. 6.13. The amplitude of the oscillations in the differential conductance dI/dV increases with increasing magnetic field. Is this due to an increase of the z -component of the tip magnetization only, or does also the z -component of the sample magnetization increase with increasing magnetic field?

In order to clarify this point, dI/dV spectra were taken on bright and dark stripes of the Fe phase-b island of Fig. 7.21(a) at different magnetic field values. The dI/dV spectra taken at the points marked in Fig. 7.21(a) are shown in Fig. 7.21(b), and the magnetic field dependence of the dI/dV signal at -0.5 V is presented in Fig. 7.21(c). Figure 7.21(d) shows the dependence of the normalized differential conductance on the magnetic field measured on the Co core of a Fe-decorated Co island and on a bright stripe of the Fe phase-b island of Fig. 7.21(a). For the Co core, only the magnetic field values smaller than its switching field are plotted. For this range of field values, the change of the differential conductance is due to the increase of the z -component of the tip magnetic moment only, due to its superparamagnetic response to the applied magnetic field (see Section 7.4). The Co core magnetization is fixed in direction and magnitude. The green line in Fig. 7.21(d) is the Langevin fit of the data points measured on the Co core. It is clear that also the dependence of the differential conductance on the magnetic field measured on the bright stripe of Fig. 7.21(a) follows the same Langevin fit. It indicates that the local magnetic moment of the Fe phase-b stays fixed in magnitude with increasing magnetic field and the increase of the differential conductance dI/dV is only due to the increase of the z -component of the tip magnetic moment. Therefore, the magnetic field dependence of the differential conductance presented in Fig. 7.21(c) can be understood as combination of tip and sample local magnetization loops sketched in Fig. 7.22. It must be mentioned that, because of the superparamagnetic response of the tip, null or very small magnetic contrast is achieved between ± 0.1 T, and the assumed switching of the magnetic nanostructure could not be revealed experimentally. However, an upper limit of ± 0.1 T can be estimated from our measurements.

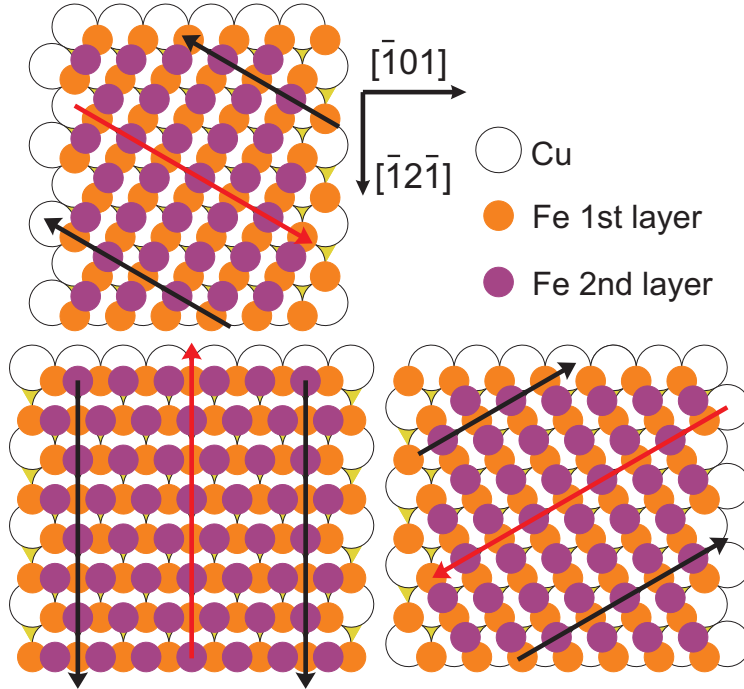


Figure 7.23: Hardsphere model representing the three symmetric stacking configurations of Fe phase-b on Cu(111), assuming the so-called bcc structure of Fe on Cu(111) proposed in ref. [159]. The black and red arrows represent the dark and bright stripes, respectively, observed in the dI/dV images taken in-field on the Fe phase-b.

In Section 6.3, a stripe periodicity of 1.28 ± 0.06 nm was extracted from measurements on both pure Fe phase-b islands and Fe phase-b regions at the decorations of Co islands. This stripe periodicity corresponds to 5 nearest neighbor distances of the Cu(111) substrate within the experimental error ($d_{NN:Cu(111)} = 0.255$ nm [193], $5 \times d_{NN:Cu(111)} = 1.275$ nm). Figure 7.23 shows a hardsphere model of the system assuming the atomic arrangement proposed in ref. [159] for the Fe phase-b, i.e. the so-called bbc stacking of Fe on Cu(111). All the three symmetric stacking configurations of Fe phase-b on Cu are sketched. The periodicity observed in the experiments suggests that if a dark stripe (black arrow) is centered on a Fe atom of the second Fe layer, the bright stripe (red arrow) is centered on a Fe atom of the first layer of the same atomic row (and vice versa for the two adjacent rows).

The discussion carried out up to this point aimed to characterize the Fe phase-b and to identify tip and sample contribution to the magnetic part of the dI/dV signal. But what is the physical origin of this stripe-like modulation of the differential conductance observed on Fe phase-b? The observed modulation may be explained by two fundamentally different spin structures: a spin-density wave or a spin spiral. A spin density wave is an antiferromagnetic ground state characterized by a spatial periodic modulation of the conduction electron spin density, and therefore of the spin polarization. Spin density waves

are observed in metals and alloys, most prominent is Cr and its alloys [194]. Recently, spin density waves were observed on the Cr(110) surface [195]. On the surface, a spin-density wave is characterized by a sinusoidal modulation of the size of the magnetic moments and the absence of spin rotation. On the other hand, spin spirals at the surface manifest themselves as magnetic moments of constant magnitude, the directions of which rotate continuously [196–198]. Spin spirals are chiral magnetic structures arising from the broken symmetry of the system. They represent a delicate energy balance between Heisenberg exchange interaction, magnetic anisotropy and Dzyaloshinskii-Moriya interaction [199,200]. The first evidence of the existence of a spin spiral at the surface was provided by Bode et al. [196] for a single atomic layer of Mn on W(110) and more recently, spin spiral states were found in bi-atomic Fe chains on the (5×1) -Ir(001) surface [197] and double-layer Mn on a W(110) surface [198]. In ref. [197], the authors show that bi-atomic Fe chains present no magnetic signal at 0 T because of thermal fluctuations which destabilize the magnetic order, only upon application of magnetic field the magnetic order is stabilized, and a net magnetization is detectable above the bi-atomic Fe chains. Moreover, the local magnetic moment of Fe chains follows the same local magnetization loops shown in Fig. 7.22. These observations may suggest that the magnetic field response of bi-atomic Fe chains on Ir(001) and Fe phase-b islands on Cu(111) may be the same. However, a clear cut evidence would require to obtain spin resolved measurements at 0 T on Fe phase-b islands to check the magnetic state of the system in absence of magnetic field. Unfortunately, these kind of measurements are not feasible with the superparamagnetic response of the tips used here, and further measurements are currently performed in our laboratory to bridge this gap.

On the contrary, Fig 6.14 shows that the local magnetic moment of Fe phase-b at the decoration of Co cores inverts its direction together with the Co core magnetization. These observations suggests a strong direct exchange interaction of the Fe spins with the Co spins at the Fe-Co boundary, which fixes the direction of the Fe spins in space. With the Fe spins fixed at the Fe-Co boundary, the coupling between Fe atoms leads to a stabilization of the whole Fe phase-b region. Switching the magnetization of the Co core, also the Fe spins at the Fe-Co boundary flip, and the perturbation propagates all the way towards the edge of the island. This observation implicates the transmission of the information about the Co magnetic state without flow of charge. By measuring the spin direction at a defined position of the Fe phase-b decoration, even nanometers away, the magnetic state of the Co core can be read out and its changes can be monitored. This novel mechanism of information transmission has been pointed out by Menzel et al. [197] recently. In that work, the authors show that by measuring the spin direction of a Fe atom at the end of a bi-atomic Fe chain they are able to read out the magnetic state of a Co particle with a fixed magnetization direction. Here, we show that a similar mechanism transfers the reversal of the Co core magnetization direction nm away through the Fe phase-b.

In conclusion, a novel and unexpected magnetic order is found for Fe phase-b on Cu(111). When the Fe phase-b is located in direct contact to Co cores, the Fe spins at the Co-Fe border are exchange coupled with the Co spins and the stripe-like magnetic structure of the Fe phase-b switches along with the Co core magnetization. Both spin density wave and spin spiral can explain the measurements obtained on Fe phase-b. Further measurements and on-going *ab-*

initio calculations will shed light on the origin of the observed stripe-like pattern soon.

7.8.2 Fe phase-a

A consideration concerning the measurement presented in Fig. 6.16 is necessary in view of the magnetic state of Fe phase-a. Figure 6.16(d) shows a hysteresis loop of the differential conductance dI/dV measured on the Fe phase-a region of the Fe-decorated Co island of Fig. 6.16(a). No clear dependence of the differential conductance on the magnetic field is evident for Fe phase-a, whereas a clear drop in the dI/dV signal due to the switching of the Co core magnetization can be observed in Fig. 6.16(c). Gerhard et al. [159] performed *ab-initio* calculations which predicted a layer-wise antiferromagnetic order with out-of-plane orientation of the spins for Fe phase-a (I remind the reader that they call it Fe fcc). Although the absence of magnetic signal for an antiferromagnetic structure is a reasonable assumption at a first sight, a deeper thought reveals that the proposed magnetic structure does not agree with the magnetic field dependence of the differential conductance measured in Fig. 6.16(d). Indeed, it was shown that sp-STM is sensitive to the spin orientations of the last atomic layer only [129, 130, 201]. Thus, supposing an arbitrary out-of-plane orientation of the spins of the last Fe layer, the magnetic field dependence of the differential conductance measured on Fe phase-a would show the superparamagnetic response of the tip and it would look like Fig. 7.24. Thus, the proposed layer-wise antiferromagnetic structure does not agree with our observation. However, a layer-wise antiferromagnetic structure with in-plane orientation of the spins can not be excluded, since in-plane magnetic sensitivity is never achieved with the tips used in this work. Also more complex magnetic structure, such as non-collinear magnetic structure without a net local out-of-plane magnetization, would lead to the same result and further measurements are presently performed in our laboratory to shed light on it.

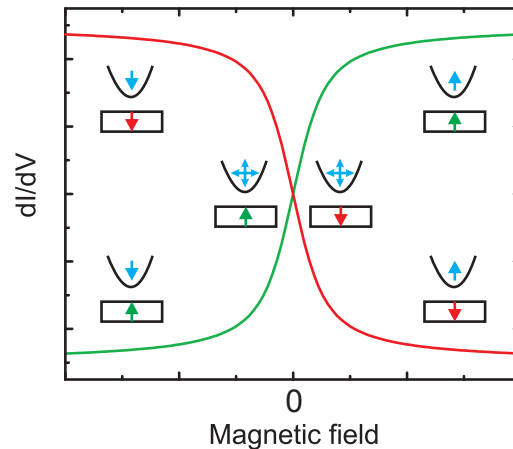


Figure 7.24: Magnetic field dependence of the differential conductance dI/dV signal resulting from a fixed out-of-plane spin direction of the last atomic layer of the sample and a superparamagnetic response of the tip apex magnetic moment.

7.8.3 Spin polarization of Fe-decorated Co islands

A powerful way to extract information concerning spatial and energy variations of the spin polarization of the sample consists in measuring asymmetry maps of the differential conductance dI/dV , as explained in section 3.4. Figure 7.25(f,g) shows two dI/dV asymmetry images measured above a pure Co island [95]. The images show spatial modulation of the spin polarization inside the Co island and the inversion of the sign of the spin polarization at the edges of the island. The modulation of the spin polarization inside the island is due to spin dependent quantum confinement, whereas the inversion of the spin polarization at the rim reflects the opposite spin character of the Co rim state in respect to the electron states in the inner part of the island, as thoroughly discussed in ref. [95]. For most of the measurements presented in Section 6.3 and discussed here, an opposite sign of the dI/dV signal is observed between parallel and antiparallel states over a wide energy range, both on the Co core and transition regions between Co and Fe. This is visible for the Co core in Fig. 6.9(a), where the spectra of the differential conductance for anti-parallel (2.1 T) and parallel (2.2 T) states have similar amplitude but opposite sign for a voltage interval between -0.8 V and -0.5 V. This is a peculiar tip induced effect which brings the sum $dI/dV_{AP} + dI/dV_P$ at the dominator in Eq. 3.1 close to zero. As a consequence, the asymmetry of the differential conductance diverges. For this reason, only maps of the numerator of Eq. 3.1 were extracted on the Fe decorated Co island of Fig. 7.25(a), and they are presented in Fig. 7.25(b-d). The cyan line indicates the edges of the island, the purple line the Co-Fe border and the green line marks off the Fe phase-a region. Using Eq. 2.5, the quantity shown in Fig. 7.25(b-d) is given by $dI/dV_{AP} - dI/dV_P \propto -\rho_T \rho_S P_T P_S$. At a fixed voltage, ρ_T and P_T are constant and the images show the spatial variation of the quantity $\rho_S P_S$. Since ρ_S is positive for definition, the sign of the quantity $dI/dV_{AP} - dI/dV_P$ comes from the sample spin polarization P_S . Thus, a qualitative comparison between the images (c)-(f) and (d)-(g) is meaningful and qualitative information about the spatial variation of the sample spin polarization can be extracted.

The most pronounced difference between the pure Co island and the Co core of the Fe-decorated Co island is the absence of the inversion of the sign of the spin polarization at the rim of the Co core in Fe-decorated Co islands. In Fig. 7.25(c,d) the Co spin polarization maintains the same sign all over the Co core and no inversion of the sign of the spin polarization due to the Co rim state is observed. This is a further consequence of the absence of the Co rim state at the Co core edges, as already shown by spatial dependent dI/dV measurements in Section 7.2. Also, the Co core of the Fe-decorated Co island shows spatial modulations of the spin polarization due to spin dependent electron confinement, as identified for pure Co islands, which extends up to Co-Fe border. We can conclude that the disappearance of the Co rim state due to the Fe decoration has many implications, from electron confinement (Section 7.2) to magnetism (Section 7.7.2) and electron spin dependent properties. Whereas Co islands show spatial dependent electronic and magnetic properties, within the Co region, Co cores of Fe-decorated Co islands are characterized by uniform properties which do not change up to the Co-Fe border, except for electron confinement induced modulations.

A second important observation is the strong energy dependence of the spin polarization on Fe and Co-Fe borders. Whereas the Co core spin polarization

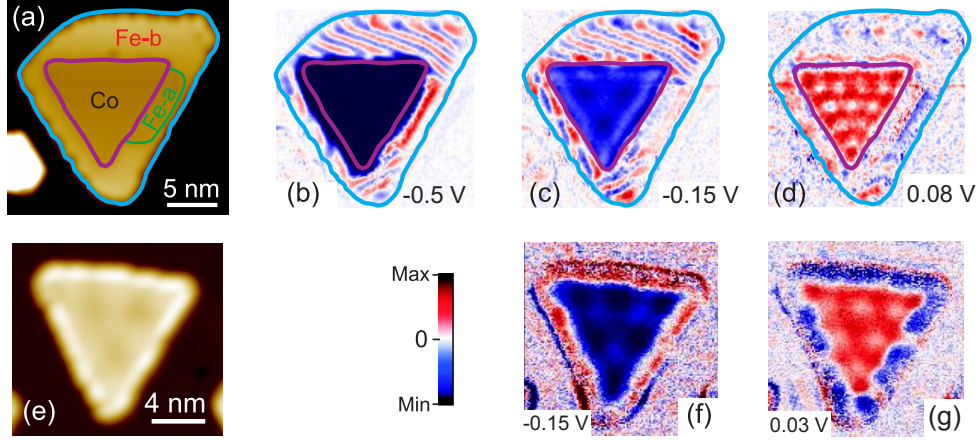


Figure 7.25: (a) Constant current image of the Fe-decorated Co island on which the measurements presented in (b-d) were taken. The purple line indicates the Co-Fe border, the green line marks off the Fe phase-a area and the cyan line shows the Fe edges of the island. (b-d) Maps of the quantity $dI/dV_{AP} - dI/dV_P = -\rho_T \rho_S P_T P_S$ measured on the Fe-decorated Co island in (a) at different energy. (e) Constant current image of the Co island on which the measurements presented in (f,g) were taken [95]. (f,g) Asymmetry maps of the differential conductance dI/dV extracted for a pure Co island showing spin dependent quantum confinement [95]. Measurement parameters: $I_t = 1$ nA, $V_{gap} = +0.1$ V, $I_{stab} = 1$ nA, $V_{stab} = +0.5$ V.

changes abruptly at the Co-Fe border in Fig. 7.25(c,d), the Co spin polarization extends across the Co-Fe border into the Fe decoration in Fig. 7.25(b). Interestingly, it can be noticed that the Fe phase-a area does not show any clear asymmetry signal in Fig. 7.25(c,d), whereas a clear induced asymmetry signal is detected in the Fe phase-a region in Fig. 7.25(b). This is probably due to the Co induced spin polarization of the Fe in proximity of the Co core.

Also, an inversion of the color of the stripes can be observed in the stripe pattern of Fe phase-b between Fig. 7.25(b) and Fig. 7.25(c). Inspecting the right-upper corner of the Co core of Fig. 7.25(b), the color of the first stripe close to the Co core is red, as well as the color of the last stripe at the right-upper Fe edge of the island. On the other hand, the color of the same two stripes turn into blue in Fig. 7.25(c). No stripes can be observed at energies bigger than the Fermi energy. This change of contrast of the stripe pattern is observed around -0.4 V and it may be due to an inversion of tip or sample spin polarization. Since this change is observed with all the magnetic tips which were used here, it can be safely concluded that the inversion of sign of the stripe pattern is due to an inversion of the spin polarization of the Fe phase-b around -0.4 V.

In conclusion, a further indication for the absence of the Co rim state in Fe-decorated Co islands as compared to pure Co islands is presented in the images of Fig. 7.25. Moreover, spin dependent electronic properties become constant all over the Co core upon Fe decoration.

Chapter 8

Conclusions and outlook

Spin-polarized scanning tunneling microscopy has been used in this thesis to study spin-dependent electronic and magnetic properties of Co and Fe nano structures on Cu(111). This technique has been used also to investigate electron confinement in Co nano islands and Fe-decorated Co nano islands on Cu(111) and graphene nano islands on Ir(111).

This thesis shows the first evidence of electron confinement within graphene nano islands grown on Ir(111) [54]. Graphene offers exciting visions for applications in future nano electronics. However, a prominent question for its application is how electronic properties depend on the size at the nanoscale. Here, we advance the understanding of the physics relevant for graphene-based electronics by scanning tunneling spectroscopy, which we used to elucidate electron quantum confinement effects in graphene nano islands on Ir(111).

Observation of electron confinement in nano structures also delivers information about the scattering potential and its spatial dependence. In this thesis, we introduce a new approach to alter the scattering potential of a nano structure by modifying the electronic properties at the edges. To achieve this goal, Co islands were decorated with Fe and electron confinement within both pure Co islands and Co cores of Fe-decorated Co islands on Cu(111) was instigated. A quantitative analysis identifies the characteristic confinement length in the two systems. The comparison shows that the relevant boundary for electron confinement is strongly influenced by the local electronic properties induced by structural relaxations at the edge of Co islands. This study provides novel insights in the correlations between electron confinement, structural relaxations and local electronic properties at the edges of nanostructures.

Structural relaxations and local electronic properties at the edge of nanostructures do not only play a fundamental role in the electron confinement of the Co surface states. Our study indicates that also the magnetism of Co islands and Fe-decorated Co islands is strongly influenced. We apply spin-polarized scanning tunneling microscopy in magnetic fields to analyze the magnetization reversal of individual Fe-decorated Co islands on Cu(111) quantitatively, and we compare the results to our previous study on Co islands on Cu(111) [77, 78]. For Co islands, we can describe our data within the Néel-Brown model of thermally assisted reversal. The analysis indicates that the rim atoms are magnetically soft, i.e. they show a negligible magnetic anisotropy, whereas the inner part of the islands is characterized by a considerable effective magnetic anisotropy of

0.150 ± 0.005 meV/atom. The width of the magnetically soft rim is deduced to be around 1 – 4 atoms wide, which is roughly the extension of the electronic Co rim state. For Fe-decorated Co islands on Cu(111), the Fe decoration decreases the magnetic anisotropy of the system up to 30%. At the same time, both the electronic Co rim state and the magnetically soft rim of Co islands are removed upon Fe-decoration. What can we learn from this?

Previous studies carried out at the MPI Halle indicate that the magnetic properties such as spin-polarization and tunnel magneto resistance vary sharply at the rim of Co islands on Cu(111) [95, 97]. Here, we deduce from a quantitative analysis of the magnetization reversal that also the magnetic anisotropy changes at the rim. Also, a previous combined experimental and theoretical study [115] has demonstrated that structural relaxations in Co islands modify their electronic structure at their edges. A clear understanding of the impact of electronic and structural relaxation on magnetic anisotropy has not been established yet. We suspect that the pronounced spatial variation of the electronic structure at the edge of a single Co island is the key to understand the resulting magnetic anisotropy. A support to this idea comes from the results obtained on Fe-decorated Co islands, where the disappearance of the electronic Co rim state at the edges of Co cores comes along with the disappearance of the magnetically soft rim. Future combined efforts in theory and experiment are called for to establish whether the similarity between the width of the rim region, as observed in tunneling spectroscopy, as compared to the width of the region with vanishing anisotropy, from the analysis of the magnetic switching fields, is of a related electronic origin.

This thesis offers many new insights into nanomagnetism but I feel that the most unexpected and striking result is the novel magnetic order found for nano structured bilayer Fe on Cu(111). Two different physical mechanisms can explain the origin of the stripe-like pattern observed in maps of the differential conductance: spin density wave and spin spiral. When Fe is located at the decoration of Co cores of Fe-decorated Co islands, the Fe spins at the Co-Fe border are exchange coupled with the Co spins and the Fe spins switch along with the Co core magnetization. The most interesting outlook is the clarification of the spin order in nano structured Fe on Cu(111). Spin-polarized scanning tunneling microscopy measurements and *ab-initio* calculations are currently performed to clarify this open aspect.

Ab-initio calculations have been of fundamental importance in this thesis also to understand the origin of the spatial dependence of the spin-polarized electronic properties near the edges of Co nano structures. The spin-dependence of the Smoluchowski effect at the edge of a Co nano structure has been established for the first time by our combined theoretical and experimental study. On the basis of the spin-dependent Smoluchowski effect, a new way to tune the tunneling magneto resistance on a scale of a few Ångströms is introduced.

Finally, many specific experimental aspects of sp-STM have been addressed. Thanks to the sp-STM measurements in the Cu channel between two Co islands, an upper limit of 0.05 for the smallest spin polarization detectable with the Omicron cryo-STM used in this thesis was derived. Moreover, this thesis delivers physical insights into magnetic probes for in-field sp-STM by characterizing bulk Cr tips and Fe-coated W tips. The easy fabrication process and a spin polarization as large as 45% make bulk Cr tips excellent candidates for sp-STM probes [80]. Temperature dependent measurements performed with the

Fe-coated W tips used to study Fe on Cu(111) indicate a superparamagnetic response of their tip-apex magnetic moment. A visionary goal in sp-STM is the exact characterization of the electronic and magnetic properties of the tip apex, in order to reliably disentangle tip and sample contributions from the differential conductance spectroscopy measurements. The precise characterization of the tip apex atomic structure may make this goal more accessible. This aspect is currently tackled in our laboratory by a close cooperation with Dr. Shigekazu Nagai [202, 203] who is setting up a field ion microscopy [204–206] experiment for the characterization of tips used in sp-STM.

Bibliography

- [1] A. K. Santra and D. W. Goodman, “Oxide-supported metal clusters: models for heterogeneous catalysts,” *J. Phys.: Condens. Matter*, vol. 15, p. R31, 2003.
- [2] H.-J. Freund, M. Bäumer, J. Libuda, T. Risse, G. Rupprechter, and S. Shaikhutdinov, “Preparation and characterization of model catalysts: from ultrahigh vacuum to in situ conditions at the atomic dimension,” *J. Catal.*, vol. 216, pp. 223 – 235, 2003.
- [3] A. T. Bell, “The Impact of Nanoscience on Heterogeneous Catalysis,” *Science*, vol. 299, pp. 1688–1691, 2003.
- [4] F. Besenbacher, J. V. Lauritsen, and S. Wendt, “STM studies of model catalysts,” *Nano Today*, vol. 2, pp. 30 – 39, 2007.
- [5] E. Serrano, G. Rus, and J. García-Martínez, “Nanotechnology for sustainable energy,” *Renew. Sust. Energ. Rev.*, vol. 13, pp. 2373 – 2384, 2009.
- [6] R. Singh, V. Rangari, S. Sanagapalli, V. Jayaraman, S. Mahendra, and V. Singh, “Nano-structured CdTe, CdS and TiO₂ for thin film solar cell applications,” *Sol. Energ. Mat. Sol. Cells*, vol. 82, pp. 315 – 330, 2004.
- [7] R. Katoh, A. Furube, M. Kasuya, N. Fuke, N. Koide, and L. Han, “Photoinduced electron injection in black dye sensitized nanocrystalline TiO₂ films,” *J. Mater. Chem.*, vol. 17, pp. 3190–3196, 2007.
- [8] A. Züttel, P. Sudan, P. Mauron, T. Kiyobayashi, C. Emmenegger, and L. Schlapbach, “Hydrogen storage in carbon nanostructures,” *Int. J. Hydrogen Energy*, vol. 27, pp. 203 – 212, 2002.
- [9] J.-G. Zhu, Y. Zheng, and G. A. Prinz, “Ultrahigh density vertical magnetoresistive random access memory (invited),” *J. Appl. Phys.*, vol. 87, pp. 6668–6673, 2000.
- [10] C. Stamm, F. Marty, A. Vaterlaus, V. Weich, S. Egger, U. Maier, U. Ramsperger, H. Fuhrmann, and D. Pescia, “Two-Dimensional Magnetic Particles,” *Science*, vol. 282, pp. 449–451, 1998.
- [11] K. J. Kirk, J. N. Chapman, and C. D. W. Wilkinson, “Switching fields and magnetostatic interactions of thin film magnetic nanoelements,” *Appl. Phys. Lett.*, vol. 71, pp. 539–541, 1997.

- [12] D. Weller and T. McDaniel, *Advanced Magnetic Nanostructures*. Springer, 2006.
- [13] D. McGrouther and J. N. Chapman, “Nanopatterning of a thin ferromagnetic CoFe film by focused-ion-beam irradiation,” *Appl. Phys. Lett.*, vol. 87, p. 022507, 2005.
- [14] M. Albrecht, C. T. Rettner, M. E. Best, and B. D. Terris, “Magnetic coercivity patterns for magnetic recording on patterned media,” *Appl. Phys. Lett.*, vol. 83, pp. 4363–4365, 2003.
- [15] J. Shen and J. Kirschner, “Tailoring magnetism in artificially structured materials: the new frontier,” *Surf. Sci.*, vol. 500, pp. 300 – 322, 2002.
- [16] E. Menéndez, M. O. Liedke, J. Fassbender, T. Gemming, A. Weber, L. J. Heyderman, K. V. Rao, S. C. Deevi, S. Suriach, M. D. Baró, J. Sort, and J. Nogués, “Direct Magnetic Patterning due to the Generation of Ferromagnetism by Selective Ion Irradiation of Paramagnetic FeAl Alloys,” *Small*, vol. 5, pp. 229–234, 2009.
- [17] K. Bussmann, G. A. Prinz, S.-F. Cheng, and D. Wang, “Switching of vertical giant magnetoresistance devices by current through the device,” *Appl. Phys. Lett.*, vol. 75, pp. 2476–2478, 1999.
- [18] S. S. P. Parkin, M. Hayashi, and L. Thomas, “Magnetic Domain-Wall Racetrack Memory,” *Science*, vol. 320, pp. 190–194, 2008.
- [19] J. Åkerman, “Toward a Universal Memory,” *Science*, vol. 308, pp. 508–510, 2005.
- [20] R. Sbiaa, H. Meng, and S. N. Piramanayagam, “Materials with perpendicular magnetic anisotropy for magnetic random access memory,” *Phys. Status Solidi*, vol. 5, pp. 413–419, 2011.
- [21] R. L. Comstock, *Introduction to Magnetism and Magnetic Recording*. Wiley, 1999.
- [22] P. Gambardella, S. Rusponi, M. Veronese, S. S. Dhesi, C. Grazioli, A. Dallmeyer, I. Cabria, R. Zeller, P. H. Dederichs, K. Kern, C. Carbone, and H. Brune, “Giant Magnetic Anisotropy of Single Cobalt Atoms and Nanoparticles,” *Science*, vol. 300, pp. 1130–1133, 2003.
- [23] S. Rusponi, T. Cren, N. Weiss, M. Epple, P. Bulushek, L. Claude, and H. Brune, “The remarkable difference between surface and step atoms in the magnetic anisotropy of two-dimensional nanostructures,” *Nature Mater.*, vol. 2, pp. 546 – 551, 2003.
- [24] W. Kuch, L. I. Chelaru, F. Offi, J. Wang, M. Kotsugi, and J. Kirschner, “Tuning the magnetic coupling across ultrathin antiferromagnetic films by controlling atomic-scale roughness,” *Nature Mater.*, vol. 5, p. 128, 2006.
- [25] A. Kubetzka, P. Ferriani, M. Bode, S. Heinze, G. Bihlmayer, K. von Bergmann, O. Pietzsch, S. Blügel, and R. Wiesendanger, “Revealing Antiferromagnetic Order of the Fe Monolayer on W(001): Spin-Polarized Scanning Tunneling Microscopy and First-Principles Calculations,” *Phys. Rev. Lett.*, vol. 94, p. 087204, 2005.

- [26] G. Binnig, H. Rohrer, C. Gerber, and E. Weibel, "Surface Studies by Scanning Tunneling Microscopy," *Phys. Rev. Lett.*, vol. 49, pp. 57–61, 1982.
- [27] G. Binnig, H. Rohrer, C. Gerber, and E. Weibel, " 7×7 Reconstruction on Si(111) Resolved in Real Space," *Phys. Rev. Lett.*, vol. 50, pp. 120–123, 1983.
- [28] G. Binnig and H. Rohrer, "Scanning tunneling microscopy - from birth to adolescence," *Rev. Mod. Phys.*, vol. 59, pp. 615–625, 1987.
- [29] C. J. Chen, *Introduction to scanning tunneling microscopy*. Oxford University Press, 2nd ed., 2008.
- [30] D. A. Bonnell, *Scanning probe microscopy and spectroscopy. Theory, techniques, and applications*. Wiley-VCH, 2. edition ed., 2001.
- [31] C. Bai, *Scanning tunneling microscopy and its applications*. Springer series in surface sciences, 2000.
- [32] R. Wiesendanger, *Theory of STM and Related Scanning Probe Methods*. Springer Series in Surface Sciences, 2. edition ed., 1996.
- [33] R. Wiesendanger, H.-J. Güntherodt, G. Güntherodt, R. J. Gambino, and R. Ruf, "Observation of vacuum tunneling of spin-polarized electrons with the scanning tunneling microscope," *Phys. Rev. Lett.*, vol. 65, pp. 247–250, 1990.
- [34] M. Bode, "Spin-polarized scanning tunnelling microscopy," *Rep. Prog. Phys.*, vol. 66, p. 523, 2003.
- [35] W. Wulfhekel and J. Kirschner, "Spin-Polarized Scanning Tunneling Microscopy of Magnetic Structures and Antiferromagnetic Thin Films," *Annu. Rev. Mater. Res.*, vol. 37, pp. 69–91, 2007.
- [36] R. Wiesendanger, "Spin mapping at the nanoscale and atomic scale," *Rev. Mod. Phys.*, vol. 81, pp. 1495–1550, 2009.
- [37] K. von Bergmann, S. Heinze, M. Bode, G. Bihlmayer, S. Blügel, and R. Wiesendanger, "Complex magnetism of the Fe monolayer on Ir(111)," *New J. Phys.*, vol. 9, p. 396, 2007.
- [38] S. Heinze, K. von Bergmann, M. Menzel, J. Brede, A. Kubetzka, R. Wiesendanger, G. Bihlmayer, and S. Blügel, "Spontaneous atomic-scale magnetic skyrmion lattice in two dimensions," *Nature Phys.*, vol. 7, pp. 713–718, 2011.
- [39] M. F. Crommie, C. P. Lutz, and D. M. Eigler, "Imaging standing waves in a two-dimensional electron gas," *Nature*, vol. 363, pp. 524–527, 1993.
- [40] Y. Hasegawa and P. Avouris, "Direct observation of standing wave formation at surface steps using scanning tunneling spectroscopy," *Phys. Rev. Lett.*, vol. 71, pp. 1071–1074, 1993.

- [41] J. Li, W.-D. Schneider, R. Berndt, and S. Crampin, “Electron Confinement to Nanoscale Ag Islands on Ag(111): A Quantitative Study,” *Phys. Rev. Lett.*, vol. 80, pp. 3332–3335, 1998.
- [42] M. F. Crommie, C. P. Lutz, and D. M. Eigler, “Confinement of Electrons to Quantum Corrals on a Metal Surface,” *Science*, vol. 262, pp. 218–220, 1993.
- [43] K. Schouteden and C. Van Haesendonck, “Lateral Quantization of Two-Dimensional Electron States by Embedded Ag Nanocrystals,” *Phys. Rev. Lett.*, vol. 108, p. 076806, 2012.
- [44] J. Kliewer, R. Berndt, and S. Crampin, “Scanning tunnelling spectroscopy of electron resonators,” *New J. Phys.*, vol. 3, p. 22, 2001.
- [45] L. Bürgi, O. Jeandupeux, A. Hirstein, H. Brune, and K. Kern, “Confinement of Surface State Electrons in Fabry-Pérot Resonators,” *Phys. Rev. Lett.*, vol. 81, pp. 5370–5373, 1998.
- [46] G. Rodary, D. Sander, H. Liu, H. Zhao, L. Niebergall, V. S. Stepanyuk, P. Bruno, and J. Kirschner, “Quantization of the electron wave vector in nanostructures: Counting k -states,” *Phys. Rev. B*, vol. 75, p. 233412, 2007.
- [47] H. Jensen, J. Kröger, R. Berndt, and S. Crampin, “Electron dynamics in vacancy islands: Scanning tunneling spectroscopy on Ag(111),” *Phys. Rev. B*, vol. 71, p. 155417, 2005.
- [48] S. Pons, P. Mallet, and J.-Y. Veullen, “Electron confinement in nickel and copper nanostructures on Cu(111),” *Phys. Rev. B*, vol. 64, p. 193408, 2001.
- [49] S. Pons, P. Mallet, L. Magaud, and J. Y. Veullen, “Investigation of the Ni(111) Shockley-like surface state using confinement to artificial nanostructures,” *Europhys. Lett.*, vol. 61, p. 375, 2003.
- [50] M. Crommie, C. Lutz, D. Eigler, and E. Heller, “Quantum interference in 2D atomic-scale structures,” *Surf. Sci.*, vol. 361 - 362, pp. 864 – 869, 1996.
- [51] J. Li, W.-D. Schneider, S. Crampin, and R. Berndt, “Tunnelling spectroscopy of surface state scattering and confinement,” *Surf. Sci.*, vol. 422, pp. 95 – 106, 1999.
- [52] I. Barke and H. Hövel, “Confined Shockley Surface States on the (111) Facets of Gold Clusters,” *Phys. Rev. Lett.*, vol. 90, p. 166801, 2003.
- [53] H. C. Manoharan, C. P. Lutz, and D. M. Eigler, “Quantum mirages formed by coherent projection of electronic structure,” *Nature*, vol. 403, pp. 512 – 515, 2000.
- [54] S.-h. Phark, J. Borme, A. L. Vanegas, M. Corbetta, D. Sander, and J. Kirschner, “Direct Observation of Electron Confinement in Epitaxial Graphene Nanoislands,” *ACS Nano*, vol. 5, pp. 8162–8166, 2011.

- [55] A. K. Geim and K. S. Novoselov, “The rise of graphene,” *Nature Mater.*, vol. 6, pp. 183 – 191, 2007.
- [56] A. K. Geim, “Graphene: Status and Prospects,” *Science*, vol. 324, pp. 1530–1534, 2009.
- [57] F. Schwierz, “Graphene transistors,” *Nature Nanotechnol.*, vol. 5, pp. 487 – 496, 2010.
- [58] S. Das Sarma, S. Adam, E. H. Hwang, and E. Rossi, “Electronic transport in two-dimensional graphene,” *Rev. Mod. Phys.*, vol. 83, pp. 407–470, 2011.
- [59] F. Bonaccorso, Z. Sun, T. Hasan, and A. C. Ferrari, “Graphene photonics and optoelectronics,” *Nature Photon.*, vol. 4, pp. 611 – 622, 2010.
- [60] R. Smoluchowski, “Anisotropy of the Electronic Work Function of Metals,” *Phys. Rev.*, vol. 60, pp. 661–674, 1941.
- [61] O. P. Polyakov, M. Corbetta, O. V. Stepanyuk, H. Oka, A. M. Saletsky, D. Sander, V. Stepanyuk, and J. Kirschner, “Spin-dependent Smoluchowski effect,” *Phys. Rev. B*, vol. 86, p. 235409, 2012.
- [62] R. O’Handley, *Modern Magnetic Materials: Principles and Applications*. Wiley, 2000.
- [63] D. Weller and A. Moser, “Thermal effect limits in ultrahigh-density magnetic recording,” *IEEE Trans. Magn.*, vol. 35, p. 4423, 1999.
- [64] E. Y. Vedmedenko, H. P. Oepen, and J. Kirschner, “Size-dependent spin reorientation transition in nanoplatelets,” *Phys. Rev. B*, vol. 67, p. 012409, 2003.
- [65] W. Wernsdorfer, *Classical and Quantum Magnetization Reversal Studied in Nanometer-Sized Particles and Clusters*, pp. 99–190. John Wiley & Sons, Inc., 2007.
- [66] R. Skomski, “Nanomagnetics,” *J. Phys.: Condens. Matter*, vol. 15, p. R841, 2003.
- [67] U. Nowak, O. N. Mryasov, R. Wieser, K. Guslienko, and R. W. Chantrell, “Spin dynamics of magnetic nanoparticles: Beyond Brown’s theory,” *Phys. Rev. B*, vol. 72, p. 172410, 2005.
- [68] D. A. Garanin and H. Kachkachi, “Magnetization reversal via internal spin waves in magnetic nanoparticles,” *Phys. Rev. B*, vol. 80, p. 014420, 2009.
- [69] S. Rohart, P. Campiglio, V. Repain, Y. Nahas, C. Chacon, Y. Girard, J. Lagoute, A. Thiaville, and S. Rousset, “Spin-Wave-Assisted Thermal Reversal of Epitaxial Perpendicular Magnetic Nanodots,” *Phys. Rev. Lett.*, vol. 104, p. 137202, 2010.
- [70] H.-B. Braun, “Topological effects in nanomagnetism: from superparamagnetism to chiral quantum solitons,” *Adv. Phys.*, vol. 61, pp. 1–116, 2012.

- [71] A. Berger, N. Supper, Y. Ikeda, B. Lengsfeld, A. Moser, and E. E. Fullerton, “Improved media performance in optimally coupled exchange spring layer media,” *Appl. Phys. Lett.*, vol. 93, p. 122502, 2008.
- [72] W. Wernsdorfer, E. B. Orozco, K. Hasselbach, A. Benoit, B. Barbara, N. Demoncy, A. Loiseau, H. Pascard, and D. Maily, “Experimental Evidence of the Néel-Brown Model of Magnetization Reversal,” *Phys. Rev. Lett.*, vol. 78, pp. 1791–1794, 1997.
- [73] W. Wernsdorfer, E. Bonet Orozco, K. Hasselbach, A. Benoit, D. Maily, O. Kubo, H. Nakano, and B. Barbara, “Macroscopic Quantum Tunneling of Magnetization of Single Ferrimagnetic Nanoparticles of Barium Ferrite,” *Phys. Rev. Lett.*, vol. 79, pp. 4014–4017, 1997.
- [74] E. F. Kneller and F. E. Luborsky, “Particle Size Dependence of Coercivity and Remanence of Single-Domain Particles,” *J. Appl. Phys.*, vol. 34, pp. 656–658, 1963.
- [75] S. Wedekind, *A spin-polarized scanning tunneling microscopy and spectroscopy study of individual nanoscale particles grown on copper surfaces*. PhD thesis, Martin-Luther-Universität at Halle-Wittenberg, 2009.
- [76] S. Wedekind, G. Rodary, J. Borme, S. Ouazi, Y. Nahas, M. Corbetta, H. Oka, D. Sander, and J. Kirschner, “Switching Fields of Individual Co Nanoislands,” *IEEE Trans. Magn.*, vol. 47, pp. 3351–3354, 2011.
- [77] S. Ouazi, S. Wedekind, G. Rodary, H. Oka, D. Sander, and J. Kirschner, “Magnetization Reversal of Individual Co Nanoislands,” *Phys. Rev. Lett.*, vol. 108, p. 107206, 2012.
- [78] D. Sander, H. Oka, M. Corbetta, V. Stepanyuk, and J. Kirschner, “New insights into nano-magnetism by spin-polarized scanning tunneling microscopy,” *J. Electron Spectrosc. Relat. Phenom.*, vol. -, pp. – In Press, 2012.
- [79] G. Rodary, S. Wedekind, H. Oka, D. Sander, and J. Kirschner, “Characterization of tips for spin-polarized scanning tunneling microscopy,” *Appl. Phys. Lett.*, vol. 95, p. 152513, 2009.
- [80] M. Corbetta, S. Ouazi, J. Borme, Y. Nahas, F. Donati, H. Oka, S. Wedekind, D. Sander, and J. Kirschner, “Magnetic Response and Spin Polarization of Bulk Cr Tips for In-Field Spin-Polarized Scanning Tunneling Microscopy,” *Jpn. J. Appl. Phys.*, vol. 51, p. 030208, 2012.
- [81] G. Rodary, J.-C. Girard, L. Largeau, C. David, O. Mauguin, and Z.-Z. Wang, “Atomic structure of tip apex for spin-polarized scanning tunneling microscopy,” *Appl. Phys. Lett.*, vol. 98, p. 082505, 2011.
- [82] J. Prokop, A. Kukunin, and H. J. Elmers, “Spin-polarized scanning tunneling microscopy and spectroscopy of ultrathin Fe/Mo(110) films using W/Au/Co tips,” *Phys. Rev. B*, vol. 73, p. 014428, 2006.

- [83] A. L. Bassi, C. S. Casari, D. Cattaneo, F. Donati, S. Foglio, M. Passoni, C. E. Bottani, P. Biagioni, A. Brambilla, M. Finazzi, F. Ciccacci, and L. Duo, “Bulk Cr tips for scanning tunneling microscopy and spin-polarized scanning tunneling microscopy,” *Appl. Phys. Lett.*, vol. 91, p. 173120, 2007.
- [84] W. Wulfhekel and J. Kirschner, “Spin-polarized scanning tunneling microscopy on ferromagnets,” *Appl. Phys. Lett.*, vol. 75, pp. 1944–1946, 1999.
- [85] H. Ibach and H. Lüth, *Solid-State Physics*. Springer, 2003.
- [86] M. Julliere, “Tunneling between ferromagnetic films,” *Phys. Lett. A*, vol. 54, pp. 225 – 226, 1975.
- [87] J. Bardeen, “Tunnelling from a Many-Particle Point of View,” *Phys. Rev. Lett.*, vol. 6, pp. 57–59, 1961.
- [88] J. R. Oppenheimer, “Three Notes on the Quantum Theory of Aperiodic Effects,” *Phys. Rev.*, vol. 31, pp. 66–81, 1928.
- [89] J. C. Slonczewski, “Conductance and exchange coupling of two ferromagnets separated by a tunneling barrier,” *Phys. Rev. B*, vol. 39, pp. 6995–7002, 1989.
- [90] J. Tersoff and D. R. Hamann, “Theory and Application for the Scanning Tunneling Microscope,” *Phys. Rev. Lett.*, vol. 50, pp. 1998–2001, 1983.
- [91] J. Tersoff and D. R. Hamann, “Theory of the scanning tunneling microscope,” *Phys. Rev. B*, vol. 31, pp. 805–813, 1985.
- [92] S. Heinze, M. Bode, A. Kubetzka, O. Pietzsch, X. Nie, S. Blügel, and R. Wiesendanger, “Real-Space Imaging of Two-Dimensional Antiferromagnetism on the Atomic Scale,” *Science*, vol. 288, pp. 1805–1808, 2000.
- [93] C. L. Gao, W. Wulfhekel, and J. Kirschner, “Revealing the 120 Antiferromagnetic Néel Structure in Real Space: One Monolayer Mn on Ag(111),” *Phys. Rev. Lett.*, vol. 101, p. 267205, 2008.
- [94] D. Wortmann, S. Heinze, P. Kurz, G. Bihlmayer, and S. Blügel, “Resolving Complex Atomic-Scale Spin Structures by Spin-Polarized Scanning Tunneling Microscopy,” *Phys. Rev. Lett.*, vol. 86, pp. 4132–4135, 2001.
- [95] H. Oka, P. A. Ignatiev, S. Wedekind, G. Rodary, L. Niebergall, V. S. Stepanyuk, D. Sander, and J. Kirschner, “Spin-Dependent Quantum Interference Within a Single Magnetic Nanostructure,” *Science*, vol. 327, pp. 843–846, 2010.
- [96] P. A. Ignatiev, O. O. Brovko, and V. S. Stepanyuk, “Local tunneling magnetoresistance control with surface-state confinement and external electric field,” *Phys. Rev. B*, vol. 86, p. 045409, 2012.
- [97] H. Oka, K. Tao, S. Wedekind, G. Rodary, V. S. Stepanyuk, D. Sander, and J. Kirschner, “Spatially Modulated Tunnel Magnetoresistance on the Nanoscale,” *Phys. Rev. Lett.*, vol. 107, p. 187201, 2011.

- [98] A. Rabe, N. Memmel, A. Steltenpohl, and T. Fauster, “Room-Temperature Instability of Co/Cu(111),” *Phys. Rev. Lett.*, vol. 73, pp. 2728–2731, 1994.
- [99] J. de la Figuera, J. E. Prieto, C. Ocal, and R. Miranda, “Scanning-tunneling-microscopy study of the growth of cobalt on Cu(111),” *Phys. Rev. B*, vol. 47, pp. 13043–13046, 1993.
- [100] N. N. Negulyaev, V. S. Stepanyuk, P. Bruno, L. Diekhöner, P. Wahl, and K. Kern, “Bilayer growth of nanoscale Co islands on Cu(111),” *Phys. Rev. B*, vol. 77, p. 125437, 2008.
- [101] P. J. Bryant, H. S. Kim, Y. C. Zheng, and R. Yang, “Technique for shaping scanning tunneling microscope tips,” *Rev. Sci. Instrum.*, vol. 58, p. 1115, 1987.
- [102] J. P. Ibe, P. P. Bey, S. L. Brandow, R. A. Brizzolara, N. A. Burnham, D. P. DiLella, K. P. Lee, C. R. K. Marrian, and R. J. Colton, “On the electrochemical etching of tips for scanning tunneling microscopy,” *J. Vac. Sci. Technol. A*, vol. 8, p. 3570, 1990.
- [103] R. Kazinczi, E. Szöcs, E. Kálmán, and P. Nagy, “Novel methods for preparing EC STM tips,” *Appl. Phys. A*, vol. 66, p. S535S538, 1998.
- [104] A. I. Oliva, A. Romero G., J. L. Peña, E. Anguiano, and M. Aguilar, “Electrochemical preparation of tungsten tips for a scanning tunneling microscope,” *Rev. Sci. Instrum.*, vol. 67, p. 1917, 1996.
- [105] O. Pietzsch, A. Kubetzka, M. Bode, and R. Wiesendanger, “Spin-Polarized Scanning Tunneling Spectroscopy of Nanoscale Cobalt Islands on Cu(111),” *Phys. Rev. Lett.*, vol. 92, p. 057202, 2004.
- [106] O. Pietzsch, S. Okatov, A. Kubetzka, M. Bode, S. Heinze, A. Lichtenstein, and R. Wiesendanger, “Spin-Resolved Electronic Structure of Nanoscale Cobalt Islands on Cu(111),” *Phys. Rev. Lett.*, vol. 96, p. 237203, 2006.
- [107] S.-h. Phark, J. Borme, A. L. Vanegas, M. Corbetta, D. Sander, and J. Kirschner, “Atomic structure and spectroscopy of graphene edges on Ir(111),” *Phys. Rev. B*, vol. 86, p. 045442, 2012.
- [108] A. T. N’Diaye, J. Coraux, T. N. Plasa, C. Busse, and T. Michely, “Structure of epitaxial graphene on Ir(111),” *New J. Phys.*, vol. 10, p. 043033, 2008.
- [109] P. R. Wallace, “The Band Theory of Graphite,” *Phys. Rev.*, vol. 71, pp. 622–634, 1947.
- [110] A. H. Castro Neto, F. Guinea, N. M. R. Peres, K. S. Novoselov, and A. K. Geim, “The electronic properties of graphene,” *Rev. Mod. Phys.*, vol. 81, pp. 109–162, 2009.
- [111] L. Diekhöner, M. A. Schneider, A. N. Baranov, V. S. Stepanyuk, P. Bruno, and K. Kern, “Surface States of Cobalt Nanoislands on Cu(111),” *Phys. Rev. Lett.*, vol. 90, p. 236801, 2003.

- [112] L. Petersen, P. T. Sprunger, P. Hofmann, E. L. B. G. Briner, M. Doering, H.-P. Rust, A. M. Bradshaw, F. Besenbacher, and E. W. Plummer, “Direct imaging of the two-dimensional Fermi contour: Fourier-transform STM,” *Phys. Rev. B*, vol. 57, pp. R6858–R6861, 1998.
- [113] K. Schouteden, E. Lijnen, E. Janssens, A. Ceulemans, L. F. Chibotaru, P. Lievens, and C. V. Haesendonck, “Confinement of surface state electrons in self-organized Co islands on Au(111),” *New J. Phys.*, vol. 10, p. 043016, 2008.
- [114] H. Lüth, *Solid Surfaces, Interfaces and Thin Films*. Springer, fourth ed., 2001.
- [115] M. V. Rastei, B. Heinrich, L. Limot, P. A. Ignatiev, V. S. Stepanyuk, P. Bruno, and J. P. Bucher, “Size-Dependent Surface States of Strained Cobalt Nanoislands on Cu(111),” *Phys. Rev. Lett.*, vol. 99, p. 246102, 2007.
- [116] D. J. Griffiths, *Introduction to Quantum Mechanics*. Prentice Hall, 2004.
- [117] A. Kubetzka, M. Bode, O. Pietzsch, and R. Wiesendanger, “Spin-Polarized Scanning Tunneling Microscopy with Antiferromagnetic Probe Tips,” *Phys. Rev. Lett.*, vol. 88, p. 057201, 2002.
- [118] S. Murphy, J. Osing, and I. Shvets, “Atomically resolved p(3x1) reconstruction on the W(100) surface imaged with magnetic tips,” *J. Magn. Magn. Mater.*, vol. 198 - 199, pp. 686 – 688, 1999.
- [119] R. Wiesendanger, D. Bürgler, G. Tarrach, T. Schaub, U. Hartmann, H. J. Güntherodt, I. V. Shvets, and J. M. D. Coey, “Recent advances in scanning tunneling microscopy involving magnetic probes and samples,” *Appl. Phys. A Mater. Sci. Process.*, vol. 53, pp. 349–355, 1991.
- [120] S. Ceballos, G. Mariotto, S. Murphy, and I. Shvets, “Fabrication of magnetic STM probes and their application to studies of the Fe₃O₄(001) surface,” *Surf. Sci.*, vol. 523, pp. 131 – 140, 2003.
- [121] A. Schlenhoff, S. Krause, G. Herzog, and R. Wiesendanger, “Bulk Cr tips with full spatial magnetic sensitivity for spin-polarized scanning tunneling microscopy,” *Appl. Phys. Lett.*, vol. 97, p. 083104, 2010.
- [122] G. Rodary, S. Wedekind, D. Sander, and J. Kirschner, “Magnetic Hysteresis Loop of Single Co Nano-islands,” *Jpn. J. Appl. Phys.*, vol. 47, pp. 9013–9015, 2008.
- [123] B. Cullity and C. Graham, *Introduction to Magnetic Materials*. John Wiley, 2005.
- [124] C. P. Bean and J. D. Livingston, “Superparamagnetism,” *J. Appl. Phys.*, vol. 30, pp. S120–S129, 1959.
- [125] C. D. Graham, “Magnetocrystalline Anisotropy Constants of Iron at Room Temperature and Below,” *Phys. Rev.*, vol. 112, pp. 1117–1120, 1958.

- [126] J. A. Stroscio, D. T. Pierce, A. Davies, R. J. Celotta, and M. Weinert, “Tunneling Spectroscopy of bcc (001) Surface States,” *Phys. Rev. Lett.*, vol. 75, pp. 2960–2963, 1995.
- [127] M. Bode, M. Getzlaff, and R. Wiesendanger, “Spin-Polarized Vacuum Tunneling into the Exchange-Split Surface State of Gd(0001),” *Phys. Rev. Lett.*, vol. 81, pp. 4256–4259, 1998.
- [128] S. N. Okuno, T. Kishi, and K. Tanaka, “Spin-Polarized Tunneling Spectroscopy of Co(0001) Surface States,” *Phys. Rev. Lett.*, vol. 88, p. 066803, 2002.
- [129] T. K. Yamada, M. M. J. Bischoff, G. M. M. Heijnen, T. Mizoguchi, and H. van Kempen, “Observation of Spin-Polarized Surface States on Ultrathin bct Mn(001) Films by Spin-Polarized Scanning Tunneling Spectroscopy,” *Phys. Rev. Lett.*, vol. 90, p. 056803, 2003.
- [130] M. Kleiber, M. Bode, R. Ravlić, and R. Wiesendanger, “Topology-Induced Spin Frustrations at the Cr(001) Surface Studied by Spin-Polarized Scanning Tunneling Spectroscopy,” *Phys. Rev. Lett.*, vol. 85, pp. 4606–4609, 2000.
- [131] O. Y. Kolesnychenko, R. de Kort, M. I. Katsnelson, A. I. Lichtenstein, and H. van Kempen, “Real-space imaging of an orbital Kondo resonance on the Cr(001) surface,” *Nature*, vol. 415, pp. 507 – 509, 2002.
- [132] D. Li, J. Pearson, S. D. Bader, D. N. McIlroy, C. Waldfried, and P. A. Dowben, “Spin-polarized photoemission studies of the exchange splitting of the Gd 5*d* electrons near the Curie temperature,” *Phys. Rev. B*, vol. 51, pp. 13895–13898, 1995.
- [133] M. Donath, B. Gubanka, and F. Passek, “Temperature-Dependent Spin Polarization of Magnetic Surface State at Gd(0001),” *Phys. Rev. Lett.*, vol. 77, pp. 5138–5141, 1996.
- [134] L. Niebergall, G. Rodary, H. F. Ding, D. Sander, V. S. Stepanyuk, P. Bruno, and J. Kirschner, “Electron confinement in hexagonal vacancy islands: Theory and experiment,” *Phys. Rev. B*, vol. 74, p. 195436, 2006.
- [135] L. Niebergall, V. S. Stepanyuk, J. Berakdar, and P. Bruno, “Controlling the Spin Polarization of Nanostructures on Magnetic Substrates,” *Phys. Rev. Lett.*, vol. 96, p. 127204, 2006.
- [136] B. Lazarovits, L. Szunyogh, and P. Weinberger, “Spin-polarized surface states close to adatoms on Cu(111),” *Phys. Rev. B*, vol. 73, p. 045430, 2006.
- [137] O. O. Brovko, V. S. Stepanyuk, W. Hergert, and P. Bruno, “Probing buried magnetic nanostructures by spin-resolved local density of states at the surface: A density functional study,” *Phys. Rev. B*, vol. 79, p. 245417, 2009.

- [138] O. Šipr, S. Bornemann, J. Minár, S. Polesya, V. Popescu, A. Šimůnek, and H. Ebert, “Magnetic moments, exchange coupling, and crossover temperatures of Co clusters on Pt(111) and Au(111),” *J. Phys.: Condens. Matter*, vol. 19, p. 096203, 2007.
- [139] F. Wilhelm, M. Angelakeris, N. Jaouen, P. Pouloupoulos, E. T. Papaioannou, C. Mueller, P. Fumagalli, A. Rogalev, and N. K. Flevaris, “Magnetic moment of Au at Au/Co interfaces: A direct experimental determination,” *Phys. Rev. B*, vol. 69, p. 220404, 2004.
- [140] M. Suzuki, H. Muraoka, Y. Inaba, H. Miyagawa, N. Kawamura, T. Shimatsu, H. Maruyama, N. Ishimatsu, Y. Isohama, and Y. Sonobe, “Depth profile of spin and orbital magnetic moments in a subnanometer Pt film on Co,” *Phys. Rev. B*, vol. 72, p. 054430, 2005.
- [141] L. V. Dzemiantsova, M. Hortamani, C. Hanneken, A. Kubetzka, K. von Bergmann, and R. Wiesendanger, “Magnetic coupling of single Co adatoms to a Co underlayer through a Pd spacer of variable thickness,” *Phys. Rev. B*, vol. 86, p. 094427, 2012.
- [142] A. Al-Zubi, G. Bihlmayer, and S. Blügel, “Magnetism of 3d transition-metal monolayers on Rh(100),” *Phys. Rev. B*, vol. 83, p. 024407, 2011.
- [143] S. Pizzini, A. Fontaine, C. Giorgetti, E. Dartyge, J.-F. Bobo, M. Piecuch, and F. Baudelet, “Evidence for the Spin Polarization of Copper in Co/Cu and Fe/Cu Multilayers,” *Phys. Rev. Lett.*, vol. 74, pp. 1470–1473, 1995.
- [144] F. Meier, S. Lounis, J. Wiebe, L. Zhou, S. Heers, P. Mavropoulos, P. H. Dederichs, S. Blügel, and R. Wiesendanger, “Spin polarization of platinum (111) induced by the proximity to cobalt nanostripes,” *Phys. Rev. B*, vol. 83, p. 075407, 2011.
- [145] K. Besocke and H. Wagner, “Adsorption of W on W(110): Work-Function Reduction and Island Formation,” *Phys. Rev. B*, vol. 8, pp. 4597–4600, 1973.
- [146] H. Ishida and A. Liebsch, “Calculation of the electronic structure of stepped metal surfaces,” *Phys. Rev. B*, vol. 46, pp. 7153–7156, 1992.
- [147] K. Besocke, B. Krahl-Urban, and H. Wagner, “Dipole moments associated with edge atoms; A comparative study on stepped Pt, Au and W surfaces,” *Surf. Sci.*, vol. 68, pp. 39 – 46, 1977.
- [148] B. Krahl-Urban, E. Niekisch, and H. Wagner, “Work function of stepped tungsten single crystal surfaces,” *Surf. Sci.*, vol. 64, pp. 52 – 68, 1977.
- [149] K. Wandelt, “Properties and influence of surface defects,” *Surf. Sci.*, vol. 251 - 252, pp. 387 – 395, 1991.
- [150] I. Merrick, J. E. Inglesfield, and G. A. Attard, “Local work function and induced screening effects at stepped Pd surfaces,” *Phys. Rev. B*, vol. 71, p. 085407, 2005.

- [151] P. Bedrossian, B. Poelsema, G. Rosenfeld, L. C. Jorritsma, N. N. Lipkin, and G. Comsa, “Electron density contour smoothening for epitaxial Ag islands on Ag(100),” *Surf. Sci.*, vol. 334, pp. 1 – 9, 1995.
- [152] E. Y. Tsympal, O. N. Mryasov, and P. R. LeClair, “Spin-dependent tunnelling in magnetic tunnel junctions,” *J. Phys.: Condens. Matter*, vol. 15, p. R109, 2003.
- [153] D. Sander, A. Enders, C. Schmidhals, J. Kirschner, H. L. Johnston, C. S. Arnold, and D. Venus, “Structure and perpendicular magnetization of Fe/Ni(111) bilayers on W(110),” *J. Appl. Phys.*, vol. 81, pp. 4702–4704, 1997.
- [154] D. Sander, “The correlation between mechanical stress and magnetic anisotropy in ultrathin films,” *Rep. Prog. Phys.*, vol. 62, p. 809, 1999.
- [155] D. Sander, “The magnetic anisotropy and spin reorientation of nanostructures and nanoscale films,” *J. Phys.: Condens. Matter*, vol. 16, p. R603, 2004.
- [156] D. Sander, W. Pan, S. Ouazi, J. Kirschner, W. Meyer, M. Krause, S. Müller, L. Hammer, and K. Heinz, “Reversible H-Induced Switching of the Magnetic Easy Axis in Ni/Cu(001) Thin Films,” *Phys. Rev. Lett.*, vol. 93, p. 247203, 2004.
- [157] O. V. Lysenko, V. S. Stepanyuk, W. Hergert, and J. Kirschner, “Mesoscopic Relaxation in Homoepitaxial Metal Growth,” *Phys. Rev. Lett.*, vol. 89, p. 126102, 2002.
- [158] A. Biedermann, W. Rupp, M. Schmid, and P. Varga, “Coexistence of fcc- and bcc-like crystal structures in ultrathin Fe films grown on Cu(111),” *Phys. Rev. B*, vol. 73, p. 165418, 2006.
- [159] L. Gerhard, T. K. Yamada, T. Balashov, A. F. Takacs, R. J. H. Wesselink, M. Dane, M. Fechner, S. Ostanin, A. Ernst, I. Mertig, and W. Wulfhekel, “Magnetoelectric coupling at metal surfaces,” *Nature Nanotechnol.*, vol. 5, pp. 792 – 797, 2010.
- [160] E. J. Heller, M. F. Crommie, C. P. Lutz, and D. M. Eigler, “Scattering and absorption of surface electron waves in quantum corrals,” *Nature*, vol. 369, pp. 464 – 466, 1994.
- [161] M. F. Crommie, C. P. Lutz, D. M. Eigler, and E. J. Heller, “Quantum corrals,” *Phys. D*, vol. 83, pp. 98 – 108, 1995.
- [162] G. A. Fiete and E. J. Heller, “*Colloquium* : Theory of quantum corrals and quantum mirages,” *Rev. Mod. Phys.*, vol. 75, pp. 933–948, 2003.
- [163] I. Pletikosić, M. Kralj, P. Pervan, R. Brako, J. Coraux, A. T. N’Diaye, C. Busse, and T. Michely, “Dirac Cones and Minigaps for Graphene on Ir(111),” *Phys. Rev. Lett.*, vol. 102, p. 056808, 2009.

- [164] S. Rusponi, M. Papagno, P. Moras, S. Vlais, M. Etzkorn, P. M. Sheverdyaeva, D. Pacilé, H. Brune, and C. Carbone, “Highly Anisotropic Dirac Cones in Epitaxial Graphene Modulated by an Island Superlattice,” *Phys. Rev. Lett.*, vol. 105, p. 246803, 2010.
- [165] M. Kralj, I. Pletikosić, M. Petrović, P. Pervan, M. Milun, A. T. N’Diaye, C. Busse, T. Michely, J. Fujii, and I. Vobornik, “Graphene on Ir(111) characterized by angle-resolved photoemission,” *Phys. Rev. B*, vol. 84, p. 075427, 2011.
- [166] E. Starodub, A. Bostwick, L. Moreschini, S. Nie, F. E. Gabaly, K. F. McCarty, and E. Rotenberg, “In-plane orientation effects on the electronic structure, stability, and Raman scattering of monolayer graphene on Ir(111),” *Phys. Rev. B*, vol. 83, p. 125428, 2011.
- [167] V. M. Pereira, J. M. B. Lopes dos Santos, and A. H. Castro Neto, “Modeling disorder in graphene,” *Phys. Rev. B*, vol. 77, p. 115109, 2008.
- [168] L. Tapasztó, G. Dobrik, P. Nemes-Incze, G. Vertesy, P. Lambin, and L. P. Biró, “Tuning the electronic structure of graphene by ion irradiation,” *Phys. Rev. B*, vol. 78, p. 233407, 2008.
- [169] L. Simon, C. Bena, F. Vonau, D. Aubel, H. Nasrallah, M. Habar, and J. C. Peruchetti, “Symmetry of standing waves generated by a point defect in epitaxial graphene,” *EPJ B*, vol. 69, pp. 351–355, 2009.
- [170] P. Lacovig, M. Pozzo, D. Alfè, P. Vilmercati, A. Baraldi, and S. Lizzit, “Growth of Dome-Shaped Carbon Nanoislands on Ir(111): The Intermediate between Carbide Clusters and Quasi-Free-Standing Graphene,” *Phys. Rev. Lett.*, vol. 103, p. 166101, 2009.
- [171] H. Chen, W. Zhu, and Z. Zhang, “Contrasting Behavior of Carbon Nucleation in the Initial Stages of Graphene Epitaxial Growth on Stepped Metal Surfaces,” *Phys. Rev. Lett.*, vol. 104, p. 186101, 2010.
- [172] Y. Cui, Q. Fu, H. Zhang, and X. Bao, “Formation of identical-size graphene nanoclusters on Ru(0001),” *Chem. Commun.*, vol. 47, pp. 1470–1472, 2011.
- [173] K. A. Ritter and J. W. Lyding, “The influence of edge structure on the electronic properties of graphene quantum dots and nanoribbons,” *Nature Mater.*, vol. 8, pp. 235 – 242, 2009.
- [174] D. Subramaniam, F. Libisch, Y. Li, C. Pauly, V. Geringer, R. Reiter, T. Mashoff, M. Liebmann, J. Burgdörfer, C. Busse, T. Michely, R. Mazzarello, M. Pratzner, and M. Morgenstern, “Wave-Function Mapping of Graphene Quantum Dots with Soft Confinement,” *Phys. Rev. Lett.*, vol. 108, p. 046801, 2012.
- [175] S. J. Altenburg, J. Kröger, T. O. Wehling, B. Sachs, A. I. Lichtenstein, and R. Berndt, “Local Gating of an Ir(111) Surface Resonance by Graphene Islands,” *Phys. Rev. Lett.*, vol. 108, p. 206805, 2012.

- [176] A. A. Ünal, C. Tusche, S. Ouazi, S. Wedekind, C.-T. Chiang, A. Winkelmann, D. Sander, J. Henk, and J. Kirschner, “Hybridization between the unoccupied Shockley surface state and bulk electronic states on Cu(111),” *Phys. Rev. B*, vol. 84, p. 073107, 2011.
- [177] F. W. Payne, W. Jiang, and L. A. Bloomfield, “Magnetism and Magnetic Isomers in Free Chromium Clusters,” *Phys. Rev. Lett.*, vol. 97, p. 193401, 2006.
- [178] M. Czerner, G. Rodary, S. Wedekind, D. V. Fedorov, D. Sander, I. Mertig, and J. Kirschner, “Electronic picture of spin-polarized tunneling with a Cr tip,” *J. Magn. Magn. Mater.*, vol. 322, pp. 1416 – 1418, 2010.
- [179] T. K. Yamada, M. M. J. Bischoff, G. M. M. Heijnen, T. Mizoguchi, and H. V. Kempen, “Origin of Magnetic Contrast in Spin-Polarized Scanning Tunneling Spectroscopy: Experiments on Ultra-Thin Mn Films,” *Jpn. J. Appl. Phys.*, vol. 42, pp. 4688–4691, 2003.
- [180] C. Rau and S. Eichner, “Electron-Spin Polarization at Single-Crystalline Cr and Ni Surfaces Determined with Electron-Capture Spectroscopy,” *Phys. Rev. Lett.*, vol. 47, pp. 939–942, 1981.
- [181] T. Irisawa, T. K. Yamada, and T. Mizoguchi, “Spin polarization vectors of field emitted electrons from Fe/W tips,” *New J. Phys.*, vol. 11, p. 113031, 2009.
- [182] P. Ferriani, C. Lazo, and S. Heinze, “Origin of the spin polarization of magnetic scanning tunneling microscopy tips,” *Phys. Rev. B*, vol. 82, p. 054411, 2010.
- [183] B. Westerstrand, P. Nordblad, and L. Nordborg, “The Magnetocrystalline Anisotropy Constants of Iron and Iron-silicon Alloys,” *Phys. Scr.*, vol. 11, p. 383, 1975.
- [184] I. M. L. Billas, J. A. Becker, A. Châtelain, and W. A. de Heer, “Magnetic moments of iron clusters with 25 to 700 atoms and their dependence on temperature,” *Phys. Rev. Lett.*, vol. 71, pp. 4067–4070, 1993.
- [185] O. Fruchart, P.-O. Jubert, C. Meyer, M. Klaua, J. Barthel, and J. Kirschner, “Vertical self-organization of epitaxial magnetic nanostructures,” *J. Magn. Magn. Mater.*, vol. 239, pp. 224 – 227, 2002.
- [186] H. Elmers and U. Gradmann, “Magnetic anisotropies in Fe(110) films on W(110),” *Appl. Phys. A*, vol. 51, pp. 255–263, 1990.
- [187] S. Rohart, V. Repain, A. Tejada, P. Ohresser, F. Scheurer, P. Bencok, J. Ferré, and S. Rousset, “Distribution of the magnetic anisotropy energy of an array of self-ordered Co nanodots deposited on vicinal Au(111): X-ray magnetic circular dichroism measurements and theory,” *Phys. Rev. B*, vol. 73, p. 165412, 2006.
- [188] W. F. Brown, “Thermal Fluctuations of a Single-Domain Particle,” *Phys. Rev.*, vol. 130, pp. 1677–1686, 1963.

- [189] E. C. Stoner and E. P. Wohlfarth, “A Mechanism of Magnetic Hysteresis in Heterogeneous Alloys,” *Philosophical Transactions of the Royal Society of London. Series A, Mathematical and Physical Sciences*, vol. 240, pp. 599–642, 1948.
- [190] H. Zeng, J. Li, J. P. Liu, Z. L. Wang, and S. Sun, “Exchange-coupled nanocomposite magnets by nanoparticle self-assembly,” *Nature*, vol. 420, p. 395, 2002.
- [191] Y. Nahas, V. Repain, C. Chacon, Y. Girard, J. Lagoute, G. Rodary, J. Klein, S. Rousset, H. Bulou, and C. Goyhenex, “Dominant Role of the Epitaxial Strain in the Magnetism of Core-Shell Co/Au Self-Organized Nanodots,” *Phys. Rev. Lett.*, vol. 103, p. 067202, 2009.
- [192] P. Campiglio, N. Moreau, V. Repain, C. Chacon, Y. Girard, J. Klein, J. Lagoute, S. Rousset, H. Bulou, F. Scheurer, C. Goyhenex, P. Ohresser, E. Fonda, and H. Magnan, “Interplay between interfacial and structural properties on the magnetism of self-organized core-shell Co/Pt supported nanodots,” *Phys. Rev. B*, vol. 84, p. 235443, 2011.
- [193] J. Donohue, *Structures of the elements*. John Wiley and Sons, Inc., New York, 2011.
- [194] E. Fawcett, “Spin-density-wave antiferromagnetism in chromium,” *Rev. Mod. Phys.*, vol. 60, pp. 209–283, 1988.
- [195] B. Santos, J. M. Puerta, J. I. Cerda, R. Stumpf, K. von Bergmann, R. Wiesendanger, M. Bode, K. F. McCarty, and J. de la Figuera, “Structure and magnetism of ultra-thin chromium layers on W(110),” *New J. Phys.*, vol. 10, p. 013005, 2008.
- [196] M. Bode, M. Heide, K. von Bergmann, P. Ferriani, S. Heinze, G. Bihlmayer, A. Kubetzka, O. Pietzsch, S. Blügel, and R. Wiesendanger, “Chiral magnetic order at surfaces driven by inversion asymmetry,” *Nature*, vol. 447, p. 190, 2007.
- [197] M. Menzel, Y. Mokrousov, R. Wieser, J. E. Bickel, E. Vedmedenko, S. Blügel, S. Heinze, K. von Bergmann, A. Kubetzka, and R. Wiesendanger, “Information Transfer by Vector Spin Chirality in Finite Magnetic Chains,” *Phys. Rev. Lett.*, vol. 108, p. 197204, 2012.
- [198] Y. Yoshida, S. Schröder, P. Ferriani, D. Serrate, A. Kubetzka, K. von Bergmann, S. Heinze, and R. Wiesendanger, “Conical Spin-Spiral State in an Ultrathin Film Driven by Higher-Order Spin Interactions,” *Phys. Rev. Lett.*, vol. 108, p. 087205, 2012.
- [199] I. Dzyaloshinsky, “A thermodynamic theory of ”weak” ferromagnetism of antiferromagnetics,” *J. Phys. Chem. Solids*, vol. 4, pp. 241 – 255, 1958.
- [200] T. Moriya, “Anisotropic Superexchange Interaction and Weak Ferromagnetism,” *Phys. Rev.*, vol. 120, pp. 91–98, 1960.

- [201] U. Schlickum, C. L. Gao, W. Wulfhekel, J. Henk, P. Bruno, and J. Kirschner, “Effect of antiferromagnetic layers on the spin-dependent transport in magnetic tunnel junctions,” *Phys. Rev. B*, vol. 74, p. 054409, 2006.
- [202] Y. Sugiura, H. Liu, T. Iwata, S. Nagai, K. Kajiwara, K. Asaka, Y. Saito, and K. Hata, “Fabrication of Gas Field Ion Emitter by Field Induced Oxygen Etching Method,” *e-J. Surf. Sci. Nanotech.*, vol. 9, pp. 344–347, 2011.
- [203] R. Okawa, Y. Morikawa, S. Nagai, T. Iwata, K. Kajiwara, and K. Hata, “Stability Measurement of Ion Beam Current from Argon Field Ion Source,” *e-J. Surf. Sci. Nanotech.*, vol. 9, pp. 371–374, 2011.
- [204] E. W. Müller and K. Bahadur, “Field Ionization of Gases at a Metal Surface and the Resolution of the Field Ion Microscope,” *Phys. Rev.*, vol. 102, pp. 624–631, 1956.
- [205] T. Hagedorn, M. E. Ouali, W. Paul, D. Oliver, Y. Miyahara, and P. Grutter, “Refined tip preparation by electrochemical etching and ultrahigh vacuum treatment to obtain atomically sharp tips for scanning tunneling microscope and atomic force microscope,” *Rev. Sci. Instrum.*, vol. 82, p. 113903, 2011.
- [206] T. Sakurai, T. Hashizume, Y. Hasegawa, I. Kamiya, N. Sano, K. Yokoyama, H. Tanaka, I. Sumita, and S. Hyodo, “New versatile room-temperature field ion scanning tunneling microscopy,” *J. Vac. Sci. Technol. A*, vol. 8, p. 324, 1990.

Publications

1. S. Wedekind, G. Rodary, J. Borme, S. Ouazi, Y. Nahas, M. Corbetta, H. Oka, D. Sander, and J. Kirschner, "Switching fields of individual Co nanoislands," *IEEE Trans. Magn.*, vol. 47, p. 3351, 2011.
2. S.-h. Phark, J. Borme, A. L. Vanegas, M. Corbetta, D. Sander, and J. Kirschner, "Direct observation of electron confinement in epitaxial graphene nanoislands," *ACS Nano*, vol. 5, no. 10, p. 8162, 2011.
3. M. Corbetta, S. Ouazi, J. Borme, Y. Nahas, F. Donati, H. Oka, S. Wedekind, D. Sander, and J. Kirschner, "Magnetic response and spin polarization of bulk Cr tips for in-field spin-polarized scanning tunneling microscopy," *Jpn. J. Appl. Phys.*, vol. 51, p. 030208, 2012.
4. S.-h. Phark, J. Borme, A. L. Vanegas, M. Corbetta, D. Sander, and J. Kirschner, "Scanning tunneling spectroscopy of epitaxial graphene nanoisland on Ir(111)," *Nanoscale Res. Lett.*, vol. 7, p. 255, 2012.
5. S.-h. Phark, J. Borme, A. L. Vanegas, M. Corbetta, D. Sander, and J. Kirschner, "Atomic structure and spectroscopy of graphene edges on Ir(111)," *Phys. Rev. B*, vol. 86, p. 045442, 2012.
6. D. Sander, H. Oka, M. Corbetta, V. Stepanyuk, and J. Kirschner, "New insights into nano-magnetism by spin-polarized scanning tunneling microscopy," *J. Electron Spectrosc. Relat. Phenom.*, In Press, 2012.
7. O. P. Polyakov, M. Corbetta, O. V. Stepanyuk, H. Oka, A. M. Saletsky, D. Sander, V. Stepanyuk, and J. Kirschner, "Spin-dependent Smoluchowski effect," *Phys. Rev. B*, vol. 86, p. 235409, 2012.
8. S.-h. Phark, J. A. Fischer, M. Corbetta, D. Sander, and J. Kirschner, "Superparamagnetic response of Fe-coated W tips in spin-polarized scanning tunneling microscopy," *Appl. Phys. Lett.*, vol 103, p. 032407, 2013.

Acknowledgments

I would like to express my gratitude to my supervisor Prof. Jürgen Kirschner for giving me the opportunity to do my Ph.D. work in his department and for his continuous support and promotion of my professional career. His valuable experience, advices and intensive and stimulating discussions contributed a lot to the completion of this work.

I am indebted to Dr. Dirk Sander for his constant guidance. I am immensely thankful to him for all the fruitful discussions, encouragements and for being an excellent teacher in many aspects. His cheerful personality and his smile made working with him a great pleasure. His careful reading of this manuscript led to numerous and valuable improvements.

I profoundly appreciate the contributions to this work from our dear theory collaborators. I would like to thank Larissa Niebergall, Oleg Brovko, Nikolay Negulyaev and Valeriy Stepanyuk from the theory department at the Max-Planck-Institute of Halle and Oleg Polyakov and Oleg Stepanyuk from Faculty of Physics of Moscow State University.

I am especially grateful to my friends and colleagues of the lab, Compadre Augusto Leon, Safia Ouazi, Hirofumi Oka, Soo-Hyon Phark, Sebastian Wedekind, Jérôm Brome, Jeison Fisher, Zhen Tian, Nicole Kurowsky, Sebastian Gliga, Fabio Donati, Yasmine Nahas and Shigekazu Nagai, for their help, support and for creating a cheerful atmosphere in the lab. I thank them also for fattening me up with biscuits, sweets and candies which are a constant presence in the daily work.

I would like to thank also the staff of the mechanical, electronic workshops, administration and all colleagues of the MPI Halle for their support.

I am also grateful to Maria, Espe, Yannick, Martina, Javi, Álvaro, Floor, Valeria, Pavla, Martin, Fabio, Marco, Roberto, and all the other awesome people who I met in the last three years, for keeping me connected to the non-scientific world.

Last but not least, my thoughts are for my family. Without their love, support and encouragement I would not have been able to achieve this goal.

Curriculum vitae

Personal details

Name: Marco Corbetta
Date of birth: 6 January 1984
Sex: Male
Place of birth: Bollate (MI), Italy
Nationality: Italian
Marital status: Single
Present address: August-Bebel Str. 35, 06108, Halle (Saale), Germany
Email: corbetta@mpi-halle.de

Education

10/2009 – present Doctoral Fellow at Max Planck Institute of Microstructure Physics, Halle, Germany
09/2006 – 12/2008 Master of Science in Physics Engineering, Politecnico di Milano, Milano, Italy
09/2003 – 07/2006 Bachelor of Science in Physics Engineering, Politecnico di Milano, Milano, Italy

Erklärung an Eides statt

Hiermit erkläre ich, dass ich die vorliegende Arbeit selbstständig und ohne fremde Hilfe verfasst, andere als die von mir angegebenen Quellen und Hilfsmittel nicht benutzt und die den benutzten Werken wörtlich oder inhaltlich entnommenen Stellen als solche kenntlich gemacht habe.

Eine Anmeldung der Promotionsabsicht habe ich an keiner anderen Fakultät einer Universität oder Hochschule beantragt.

Halle (Saale), 20.11.2012

Marco Corbetta